SAPIENZA
UNIVERSITÀ DI ROMA

Stable Orbits in the Proximity of an Asteroid: Solutions for the Hayabusa 2 Mission

Dipartimento di Ingegneria Astronautica, Elettrica ed Energetica

Dottorato di Ricerca in Ingegneria Aerospaziale – XXVI Ciclo

Candidate

Marco Giancotti
ID number 1052306

Thesis Advisor

Prof. Paolo Teofilatto

A thesis submitted in partial fulfillment of the requirements
for the degree of Doctor of Philosophy in Aerospace Engineering

January 2014

Thesis defended on 25 February 2014
in front of a Board of Examiners composed by:

Prof. Alessandra Celletti

Prof. Nicola De Divitiis

Prof. Giancarmine Fasano

Stable Orbits in the Proximity of an Asteroid:Solutions for the Hayabusa 2 Mission

Ph.D. thesis. Sapienza – University of Rome

This thesis has been typeset by LaTeX and the Sapthesis class.

Author's email: ma.giancotti@gmail.com

To Pissu

Abstract

This thesis studies the dynamics that arise in the surroundings of a small asteroid with the objective of identifying feasible trajectories for use in the Japanese mission Hayabusa 2. Hayabusa 2, which is expected to be launched at the end of year 2014, will travel to near earth asteroid 1999 JU3 and rendezvous with it. The main purpose of the mission is to collect a sample of the asteroid's rock and carry it back to the earth for a detailed analysis. The spacecraft, however, will remain close to the asteroid for approximately 1.5 years, and it will perform several other types of scientific observations.

All of the operations will be carried out from a controlled hovering position, that is, a fixed point between the earth the asteroid, close to the latter. This study aims at finding orbital strategies, different from hovering, that can enhance the scientific returns of this phase. In particular, orbits passing repeatedly close to the asteroid would provide a wealth of information on the gravitational field, and thus the internal structure, that would not be available through simple hovering.

A first part of this work is focused on the circular augmented Hill's 3–body problem, a formulation similar to the restricted 3-body problem that well describes the asteroidal environment, including solar radiation pressure. In this system we perform a grid search that results in a collection of several periodic orbits. We study a group of these orbits in detail, constructing their whole families with numerical continuation and analyzing their stability properties. The orbit families are also subject to a comparison on the basis of the characteristics most appropriate to Hayabusa 2. The result of this part is the identification of a type of orbit that is most feasible for the Japanese mission.

Not treated in the above part are the two other important properties of the dynamical system, that is, the inhomogeneity of the asteroid's mass and the ellipticity of its orbit around the sun. These are considered in the second part as perturbations, and a linear quadratic regulator (LQR) is set up in order to actively eliminate them. We show that the LQR is capable of stabilizing the periodic orbits against these and other effects, using thrusts attainable, in theory, with electric propulsion.

The final part of this thesis addresses the need for trajectories that are stable in the elliptic Hill's problem without any control. Rather then looking for periodic orbits in this more complex system, we use the results from the circular case to identify non-periodic repetitive trajectories that are nonetheless stable. The result in a map of the space of initial conditions containing a wide group of trajectories that neither impact nor escape from the asteroids for long periods of time. Among these trajectories, some are especially suitable for the purposes and instrument requirements of Hayabusa 2.

Acknowledgments

I thank my mentor Prof. Paolo Teofilatto for his experienced guidance, kind support and patience, that helped me grow as a researcher and kept me from straying in front of tough challenges. I extend my gratitude to Dr. Mauro Pontani, who taught me a lot of what I know about doing research.

I would also like to thank Prof. Jun'ichiro Kawaguchi, without whom I could not have lived such a wonderful experience at JAXA, nor would I have started the research for this thesis. Thank you also to Dr. Yuichi Tsuda, fundamental provider of the driving force for this work, and Dr. Stefano Campagnola, generous advisor and strict friend (or was it the other way around?).

Besides the above mentioned names, during my three years of PhD I've become indebted to many other researchers, fellow students and friends at the School of Aerospace Engineering in Rome and at the Institute of Space and Astronautical Science in Sagamihara. Thank you, I will not forget your help and support.

Contents

List of Figures

List of Tables

Chapter 1

Introduction

The existence of asteroids in orbit around the sun was unknown until the beginning of the 19th century. While astronomers in Germany were looking for a new planet just in the region that we now know to correspond with the asteroid belt, the first asteroid was actually discovered in 1801 by Giuseppe Piazzi from the observatory of Palermo, in Sicily. He called this object *Ceres*, and started a series of discoveries that continues to this day.

The number and recognized importance of asteroids has grown in time. At first astronomers thought that only a handful of such objects existed, and even stopped looking for them for more than two decades in the first half of the 19th century. When they finally resumed, the number of yearly discoveries started growing slowly, as the number of groups searching increased and their methods improved. Hand-drawn charts were eventually replaced by photographs at the beginning of the 20th century, and the rate of new discoveries grew considerably. During the following century it became clear that asteroids formed an important group of objects in the solar system, and that their knowledge would give us hints on the formation process of the sun, the planets and our own Earth.

With the introduction of computers in the discovery and classification process, along with better telescopes on Earth and in orbit, recent years have seen an explosion in the number of recognized objects. Today, more than a million asteroids have been cataloged, although precise orbits have been determined for only a fraction of them[1]. These are distributed on the main asteroid belt, between the orbits of Mars and Jupiter, but also in other regions, even close to our planet.

Such near-earth asteroids, shortened as NEA, have become object of particular interest in the last few decades. The scientific community believes that the impact of an asteroid with the earth is the most likely cause of a mass extinction that happened in our ecosystem millions of years ago, and that other events of this kind are possible in the future. Perception of the risk of an asteroid collision has grown dramatically, and has become another important motivation for the study of these objects.

For scientific purposes, it is important that we understand how asteroids were formed, what composes and differentiates them, and why they are distributed the way they are. On the other hand, if we want to avoid a catastrophe in the not

[1] `http://www.minorplanetcenter.net/iau/lists/Desigs.html`

too distant future, we also need to learn how to deflect their paths away from the earth. Researchers have proposed a variety of methods for this task, but detailed characterization of the surface conditions of an asteroid, as well as the surrounding environment and dynamics, plays a vital role in this endeavor.

1.1 Aims and Methods of this Research

For the above reasons, space agencies around the world have started directing part of their efforts to asteroidal missions. Two asteroid-specific missions, NEAR and Hayabusa, have already been completed successfully. Another one, DAWN, is still ongoing while NASA, ESA and JAXA are currently developing three more. This dissertation is related to one of these, the future mission by JAXA to be launched in 2014: sample-return mission Hayabusa 2.

Hayabusa 2 will travel to a small NEA, called with the provisional name 1999 JU3, and remain in its vicinity for several months. During this time, it will use its scientific payload to characterize the asteroid, and it will also briefly land on its surface to collect samples of material. It will then return to the earth, where it will deliver its precious cargo to laboratories around the world.

Target 1999 JU3 is less than a kilometer in diameter and its mass, while not known precisely, is many orders of magnitude smaller than that of a planet. This allows Hayabusa 2 to hover close to the asteroid at a fixed position without incurring in unacceptable consumption of propellant. During most of its stay, Hayabusa 2 will thus perform its observations from this hovering stance, and only descend, roughly vertically, when it is needed for its other mission purposes.

Hovering is relatively easy to control and is thus a safe choice, with low risk of accidental impact or escape from the asteroid. However, it also has some downsides. First of all, it requires an almost constant thrust in the direction of the asteroid to cancel out its gravitational pull. Also, in Hayabusa 2's case, it offers only one point of view of the target body's surface, possibly hiding some of its features for long periods of times. Finally, hovering only allows for a rough estimation of the asteroid's mass, and it offers almost no sensitivity to the higher terms of the irregular gravitational field.

The aim of the research work described in this thesis is to find orbital strategies alternative to hovering that can overcome the above limitations. This is part of a study for possible additional scientific and engineering applications of the Hayabusa 2 spacecraft carried out at JAXA. Characterization of orbits in an environment strongly perturbed like that of an asteroid requires a deeper understanding of the related dynamics, and this is another, more theoretical aim of this work. While it is unlikely that the results of this study will be actually added to the mission plan, they are of interest for theoretical purposes, and for applications in future missions.

In the first phases of this research we study an approximation of the sun-asteroid-spacecraft system, called circular Hill's problem. This is a special case of the restricted 3-body problem and lends itself to detailed theoretical investigation. In this system, tuned to the parameters of Hayabusa 2, we look for periodic orbits using a grid search. Periodic orbits form the "skeleton" of the dynamics, and guide the types of motions that are possible in the region. We find many such trajectories,

and among these we select a few that are most "promising" from the point of view of the mission. These we study through numerical continuation and bifurcation theory, performing also a stability analysis.

The periodic orbits thus selected, then, are the subject of two applications. The first one is the computation of an optimal control, through the linear-quadratic regulator, to correct deviations introduced by some perturbations. We show that all the periodic orbits are stabilizable, with low-thrust, in the presence of brisk errors in orbit determination, of gravity irregularities, and of a perturbation simulating elliptic dynamics.

The second, and last, application of the periodic orbits is the search for stable trajectories in the elliptic version of Hill's problem. Since the orbit of 1999 JU3 has an eccentricity close to 0.2, the elliptic problem approximates its surrounding dynamics much better than the circular one. It is, however, harder to study because it is not a conservative system. Therefore we use the solutions found in the circular problem as starting points for the determination of types of motion that are stable in the elliptic problem for long periods of time. We identify regions in the phase space of initial conditions that are associated to this type of motion, and compare different versions of stable orbits. Some of them are found to be particularly suitable to Hayabusa 2, because they satisfy the various restrictions dictated by its design.

1.2 Outline of the Thesis

Chapter 2 of this thesis gives a brief overview of asteroid observation and exploration efforts, as well as previous results in the study of the dynamical environment around an asteroid. Special attention is given to the Hayabusa and Hayabusa 2 missions, because they are strictly related to the research that follows.

Chapters 3–9 provide all the theoretical background used in the research, ranging from the formulation of the effects of solar radiation pressure to the various dynamical models assumed for the sun-spacecraft-asteroid system. These sections also show the specific methods employed, such as numerical continuation and grid search.

Chapter 10 is the first one to display results of this work. It describes the periodic orbits found in the grid search phase for the circular Hill's problem, and the resulting orbit families. Stability and bifurcation analysis is also carried out on selected families, and an in-depth comparison of the main orbits on the basis of Hayabusa 2's requirements is used to identify the most suitable ones for the mission.

Linear quadratic control is applied to the periodic orbits in Chapter 11. We apply different perturbations, both fictitious and realistic, and show that in most cases the regulator is able to stabilize the orbits automatically and with small thrusts.

Finally, Chapter 12 describes a group of non-periodic orbits that are stable in the elliptic Hill's problem. These are found with a grid search using the periodic solutions of the circular problem as initial guesses. These trajectories are compared in order to identify those most suitable to the Hayabusa 2 mission.

Chapter 2

Background

2.1 Remote Observations of Asteroids

Since the discovery of Ceres in 1801, optical observations have been the main—and, until recently, the only—means of studying asteroids. Optical methods are necessary for the initial discovery of an astronomical body, and for the determination of its orbit. They also supply information about the asteroid's magnitude, which in turn constrains its size.

More data can be extracted when the observations continue consistently in time, rather than being isolated and far apart. By plotting the intensity of the light source as a function of time, we can determine the *light curve* of the asteroid (Figure 2.1a). The structure of this curve often contains useful hints about its physical properties, such as its shape, rotation period and spin axis. Lastly, we can study parts of the electromagnetic spectrum to learn more about the asteroid's composition. This method allows for the classification of the asteroids into spectral types and further constrains its physical properties.

Unfortunately, the data that can be obtained with optical methods is limited and, in some cases, it is not enough to constrain the parameters of the target body in a satisfactory way. This is particularly true regarding the shape model and rotational state, which therefore remain unknown to this day for most of the asteroids. With the construction of large radio telescopes capable of radar observations, it has become possible to partly solve these limitations. Radar imaging can reach high resolutions of the asteroidal surface (Figure 2.1b), and often allows for the detailed determination of shape and rotational parameters.

There are two downsides to radar observations that prevent them from being more widely used. The first one is that they require the target body to be sufficiently close, because the strength of the echoes decreases quickly with distance. The second limitation is the very low number of telescopes capable of performing such measurements as of today.

2.2 Past Exploration Missions to Asteroids

That which cannot be achieved with remote observations must be sought through more direct approaches. At the moment, the only known way to have precise models

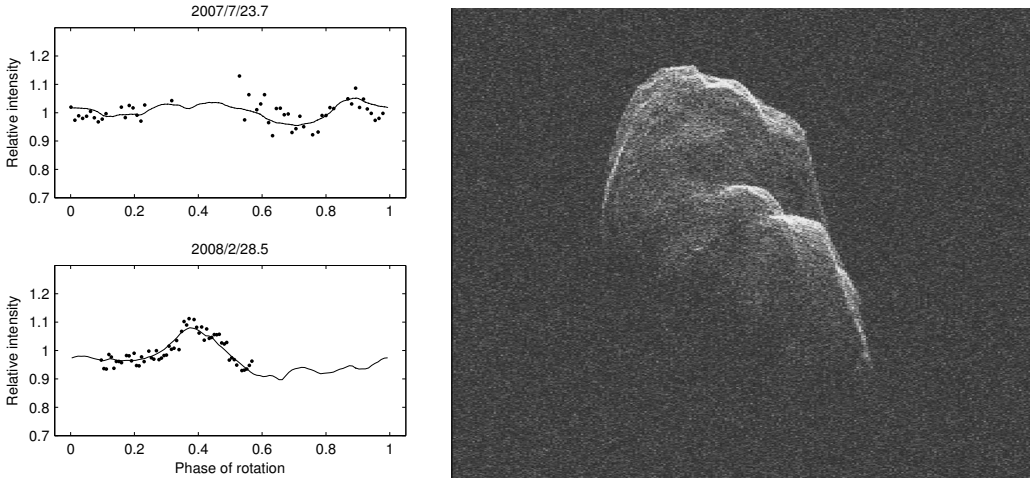

Figure 2.1. (a) Light curve of asteroid 1999 JU3 during two different observations, from Müller et al. [43]. (b) Radar image of asteroid Toutatis taken by NASA's Goldstone Solar System Radar. Credit: NASA/JPL-Caltech.

of an asteroid's mass, shape, surface appearance and related properties is to inspect it from a close distance using deep space probes.

The first few occasions for close-range asteroid observations were incidental flybys by spacecraft headed to other destinations. In 1991 the NASA Galileo mission to Jupiter approached the main belt object Gaspra to a minimum distance of approximately 1600 km, producing the first detailed images of an asteroid. The same probe then performed a flyby with another main belt asteroid two years later, when it flew past Ida and discovered, besides several of its physical properties, that it has a small moon orbiting around it.

So far, three more missions have accomplished asteroid flybys. The most recent one is the ESA Rosetta mission, still on its way to comet 67P/Churyumov-Gerasimenko, which it will reach and rendezvous with in May 2014. In 2008, Rosetta had a flyby of Šteins, passing at just 800 km from it and collecting useful information. Then Rosetta flew by Lutetia and was able to estimate its mass, as well as its size and mean density (Figure 2.2).

The new frontier of asteroid exploration is pushed by rendezvous missions, in which the spacecraft remains in close proximity of the target for long periods of time. This approach can bring a much more complete and deeper knowledge of the asteroid's parameters compared to remote observations and even flybys. The first such mission was accomplished by the NASA spacecraft NEAR Shoemaker which, after flying by main belt asteroid Mathilde, reached and was gravitationally captured by near-earth object Eros.

After reaching Eros in February 2000, NEAR remained in its vicinity for more than one year, performing a wide array of measurements. It made it possible for the first time to calculate precisely the density of an asteroid, including its internal distribution, and to determine a high fidelity shape model among other achievements. Eros has a mean radius of 16.84 km and a mass of 6.69×10^{15} kg, and is thus rather

Figure 2.2. Sequence of pictures of Lutetia during Rosetta's flyby. The asteroid rotation is visible between consecutive photographs. Credit: ESA.

large compared to the other NEAs. At the end of its mission, NEAR slowly descended onto the asteroid's surface, where it soft-landed and continued relaying data to Earth for many days. NEAR was the first mission of its kind, and had to face a number of design challenges that had not been experienced by any previous space endeavor. The main difficulties were due to the asteroid's highly non-spherical shape, as well as its short rotation period and highly inclined rotation axis.

The next rendezvous mission was the JAXA probe Hayabusa, which arrived at NEA Itokawa in 2005 and returned a sample of its surface to the earth in 2010. It was the first sample return mission to an asteroid. A more detailed description of the mission follows in Section 2.4.

The NASA spacecraft DAWN, at the moment, is the last asteroid rendezvous mission that has been commenced, and it is currently being carried out. DAWN's objectives are the two largest objects of the main asteroid belt, Vesta and Ceres. The probe reached Vesta in July 16, 2011, and kept orbiting around it for little less than 14 months. Vesta, with a mean diameter of about 525 km, is an important member of the main belt population, and it gives the name to the V-type (Vestoid) category of asteroids. These are thought to be in good part originated from Vesta during a violent impact.

DAWN observed Vesta from orbits of different altitude, down to 210 km, with detectors in the visible, infrared and gamma bands, among other things. The results of the measurements are still under study, but it will probably be possible to deduce important information about Vesta's origins and internal structure. DAWN left Vesta in September 5, 2012, and is currently on its way to Ceres. In case of success, it will be the first man-made object to orbit two different extraterrestrial bodies.

2.3 Future Missions

As mentioned in the introduction, scientific interest and security concerns for the possibility of an Earth impact have caused, in recent years, an increase of interest in asteroid exploration, and several such projects are under development around the world.

Hayabusa 2, the successor of Hayabusa, will launch in late 2014 headed for NEA 1999 JU3, as explained in Section 2.5. Like Hayabusa, it will collect samples of the asteroid's surface and take them back to the earth in 2020. Orbits for an extended mission phase of Hayabusa 2 are the object of this thesis.

NASA has also approved a sample return mission, named OSIRIS-REx, which is scheduled to reach its target in 2020. The target, Bennu, is a small near earth asteroid with mean diameter of about 500 m. Being of the same scale of 1999 JU3, the orbital dynamics about Bennu will be similar to those experienced by Hayabusa 2. Extensive study in this field is under way to design trajectories for OSIRIS-REx [58].

Still to be confirmed is MarcoPolo-R, a sample return mission developed by ESA. Currently it is competing with three other mission proposals for the M3 medium-scale mission slot opened as part of the ESA Cosmic Vision program. The proposed mission profile envisages a launch in 2022 and rendezvous with NEA 2008 EV5.

2.4 Hayabusa's Journey

The Japanese probe Hayabusa was the first mission to return an asteroid sample to the earth, and in doing so it gave an important contribution to the advancement of asteroid science, and of many aspects of rendezvous mission technology and design [26]. Among other things, it was the spacecraft driven by ion propulsion that went farthest from the sun (a record now taken by DAWN), it used its ion engines for the longest time in a single mission with 40 000 h and it performed the longest round-trip to an object of the solar system. It also tested autonomous descent, touch-down and take-off methods and technology.

The Japanese mission is even more remarkable because of the difficulties that it encountered, and of the methods that were used to overcome them against all odds. It certainly constitutes an invaluable experience that will guide the development of many future missions. It is useful, and of interest for the object of this dissertation, to retrace the missions critical moments.

Hayabusa, whose pre-launch name was MUSES-C, was launched on May 9, 2003 from the Uchinoura Space Center, and used an orbital maneuver sequence called EDVEGA (Earth-Δv-Earth Gravity Assist) to reach 25143 Itokawa. After 6 months of flight part of its solar panels were damaged by a powerful solar flare, reducing the ion engine thrust and forcing mission control to adopt a slightly longer orbit than scheduled. Before completing with success an earth swing-by, the first one ever accomplished with the aid of ion thrusters, Hayabusa suffered its first hardware failure in one reaction wheel. It was forced to use only the remaining two for its attitude control.

The probe arrived close to its target on September 2005, where it started hovering

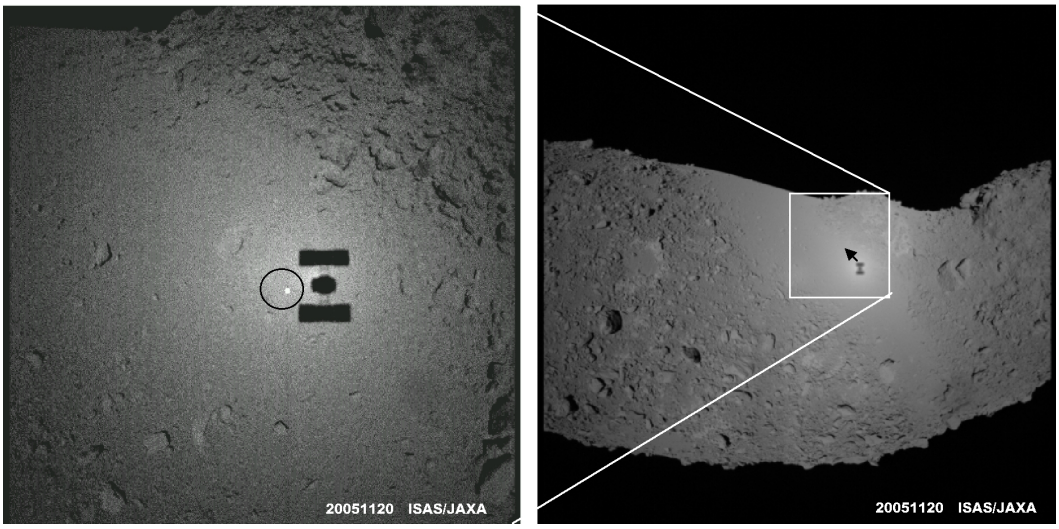

Figure 2.3. Picture taken by Hayabusa before touch-down. The shadow of the spacecraft is seen projected on Itokawa. In the enlarged picture on the left, next to the shadow, there is a point of light. It is a highly-reflective target marker deposited on the asteroid beforehand to guide the descent. Credit: ISAS/JAXA.

at its so-called *gate position*. This is a point on the earth-asteroid line at a distance of 20 km from the asteroid. It later moved closer and farther again several times to perform tests and observations of Itokawa. Apart from short periods of time during the touch-down phases, Hayabusa never entered an orbit in the traditional sense, preferring hovering as its operational and stand-by strategy.

In October another reaction wheel failed, leaving Hayabusa with only one, unable to control its attitude without the use of the reaction control system (RCS). Due to the low precision of RCS control, it became difficult, sometimes impossible, to point the earth well enough to establish a link using the high-gain antenna. The probe then carried out some descent trials to test the various instruments and methods, and encountered difficulties due to the low-precision attitude control. Finally Hayabusa attempted its first touch-down on November 20, but close to the surface it detected an obstacle and became unable to determine its exact position. After several minutes of silence, mission control sent the command to take off, and discovered that the probe had remained laying on the surface of the asteroid for 30 minutes, instead of the scheduled 1 second touch-and-go.

On November 26 Hayabusa touched down again in a different area of Itokawa, and this time the sequence went as planned. The exception was the sampling system, in which a small software error prevented the firing of a bullet that was supposed to produce easily collectible rocky fragments. Following this discovery, there was fear that the sampling capsule would be empty. In reality many microscopic fragments were captured, but this was only confirmed after the capsule had returned to the earth.

Immediately after the second touch-down a fuel leak from the RCS system was discovered and blocked. This leak, however, had deep consequences on the remainder of the mission. It was discovered much later that most of the fuel for the attitude

control had spilled out, making also the RCS unusable. Moreover, it is believed that the gasification of the spilled hydrazine caused a lowering of the internal temperature of Hayabusa. This, in turn, damaged some of the batteries and caused the reboot of several subsystems. Communication with Earth was lost for one day, then restored.

With two reaction wheels and the RCS out of order, Hayabusa could not control its own attitude. This was partly solved with the impromptu idea of substituting the reaction thrusters with the neutralizers of the ion engines. The neutralizers are needed in the electric propulsion system to avoid the accumulation of negative charge as the ions are ejected, and they were not designed to modify the attitude of the spacecraft. Nevertheless, the attempt was successful and Hayabusa stabilized its attitude on December 4.

Four days later, on December 8, the spacecraft started rotating in a precessing motion, perhaps because of the previously leaked propellant blowing out of the structure in gaseous form, and even with the neutralizers it was impossible to control. Soon the solar panels pointed away from the sun, the batteries depleted completely and all communication with Earth was lost.

The link was restored 46 days later on January 23 2006 when, by chance, the spacecraft pointed the sun again and gained enough power to power on. Fortunately the low-gain antenna was pointing roughly towards the earth, and a faint signal was detected by the ground station. In the following weeks the attitude was stabilized again using the ion engine neutralizers, and full control of the spacecraft was restored. The journey back to the earth started in March 2006.

Even after leaving Itokawa, Hayabusa's voyage was quite eventful. Out of concerns for the amount of xenon gas left for the ion engines, the use of the neutralizers for attitude control was reduced. In exchange, the spacecraft's spin axis was kept pointing toward the sun using solar radiation pressure (SRP). The torque generated by the solar radiation pressure was a slowly spiraling precession which, when under control, ensured that the solar panels always had access to sunlight [27].

After tens of thousands of hours of operation, most of the ion thrusters were degraded. In November 2009, the neutralizer of thruster D, the one used during most of the return trip, broke, raising concerns for the achievement of the necessary Δv for the final maneuvers. The problem was solved with the use of two engines in tandem: the ion source of thruster D was coupled with the neutralizer of thruster A. This expedient made it possible to produce the necessary Δv.

The now severely fatigued Hayabusa succeeded in its last orbital maneuvers, and finally reached the earth on June 13, 2010. After releasing the capsule, it managed to take one last picture (Figure 2.4), but communication was lost before it could be completely transmitted to ground station. The capsule landed safely on the Australian desert, a little over seven years after the mission's launch. The samples returned from Itokawa, as well as the lessons learned during the long mission, have been and will continue to be of great importance for the scientific community and for any institution willing to explore asteroids in the future.

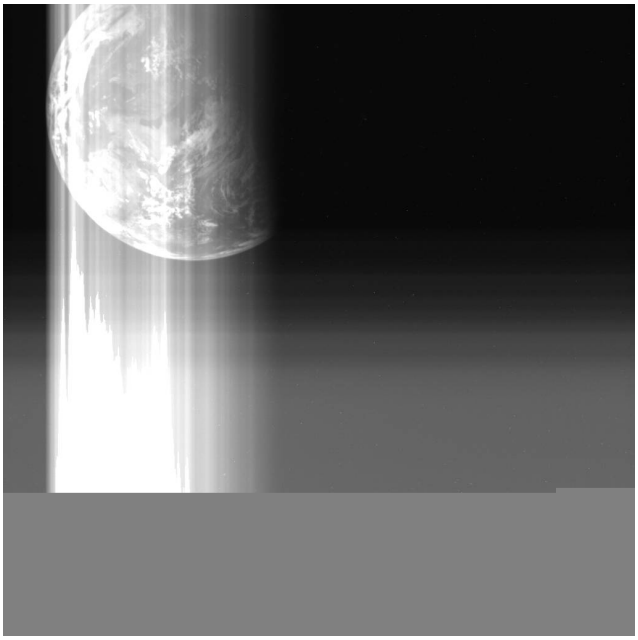

Figure 2.4. The last picture taken by Hayabusa. Credit: ISAS/JAXA.

2.5 Hayabusa 2

Development of the successor of Hayabusa started even before the first spacecraft had returned to the earth from Itokawa. The Hayabusa 2 mission is now in its final phases of preparation, with its launch scheduled for the end of 2014. Whereas Hayabusa was for a good part an engineering experiment, Hayabusa 2 is meant to build on the predecessor's achievements and to solidify JAXA's expertise with this kind of mission. Most aspects of the new mission are directly inherited from Hayabusa, but also many changes have been introduced [62].

The transfer to and back from the target asteroid, 1999 JU3, will be an EDVEGA like the previous one, with an earth gravity-assist to propel the spacecraft into an encounter trajectory with the asteroid. If launched in 2014, Hayabusa 2 will reach 1999 JU3 in mid-2018 and rendezvous with it for approximately 1.5 years until December 2019. Arrival at the earth is expected in 2020.

One of the driving motivations behind the mission is the nature of the target body. It is in fact a C-type asteroid, relatively rare among the near-earth population and different from Itokawa, which was an S-type. As a carbonaceous asteroid, 1999 JU3 could contain organic materials as well as water. The discovery of these substances would contribute to the understanding of the primordial solar system and to the hypothesis of extraterrestrial origin of life. Section 2.6 details other important properties of 1999 JU3.

Based on the difficulties encountered during the first mission, JAXA has made several improvements to Hayabusa 2, while still maintaining the same structure and overall design. In place of the single parabolic high-gain antenna of Hayabusa, the new mission will carry two smaller flat array high-gain antennas, one working in the X band and the other in the Ka band. The four ion engines will see some

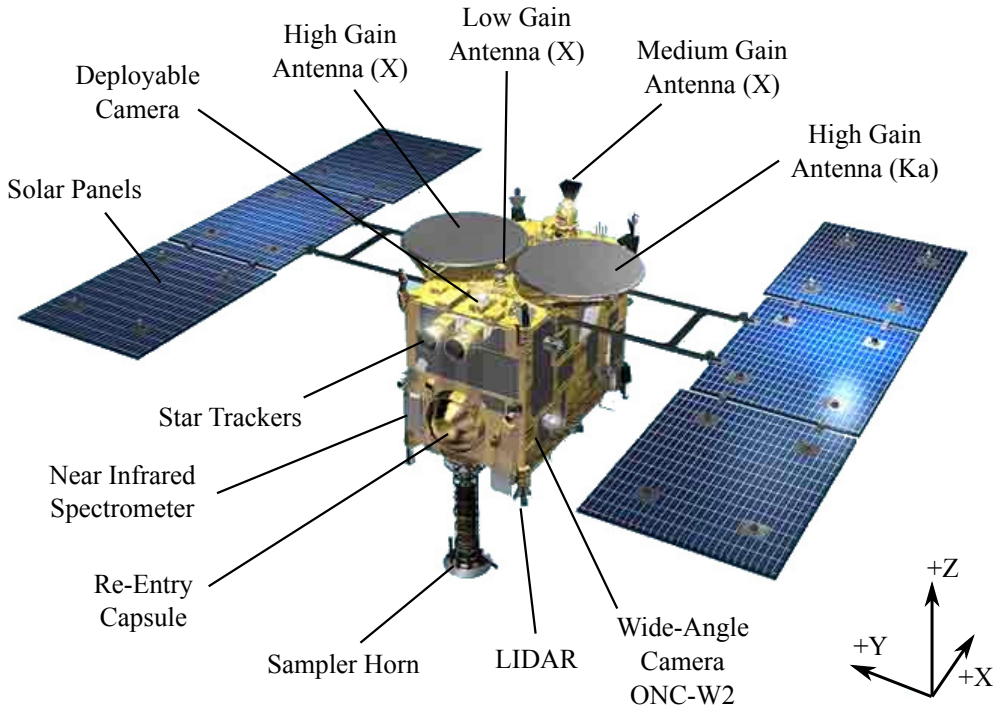

Figure 2.5. Some of Hayabusa 2's instruments, top view. Credit: ISAS/JAXA.

improvements, most notably in their thrust, which will be strengthened from 8.5 mN to 10 mN. The reaction control system, on the other hand, will be more thoroughly re-designed in response of the problematic leak that is suffered with Hayabusa. Also the reaction wheels have been updated for better reliability. On the z-axis an additional wheel has been added, bringing the number of wheels on board to four.

The surface sampling phases are subject to changes, too. The shape of the projectile used to create the fragments has been changed, and a fish-eye lens camera will be able to monitor what happens during touch-down. The biggest innovation, however, consists in the introduction of an explosive impactor device to create a crater on the asteroid. After collecting samples with the same procedure as Hayabusa, the spacecraft will release the cylindrical device and retreat on the opposite side of the asteroid. When Hayabusa 2 will be in a safe position, the device will fire a high-speed bullet towards the designated spot on 1999 JU3's surface, producing a crater of up to a few meters in width. When all the ejecta from the explosion will be far enough, the spacecraft will be able to return once more to the front to inspect the surface. If the conditions will be favorable, it will then proceed to collect more samples from the center of the crater. Access to samples of these deeper strata of the asteroid would be of great interest for the scientific community.

The mission payload will be composed of the following instruments:

- multi-band optical cameras ONC-W1 and ONC-W2;
- LIDAR, a laser altimeter like the one used by Hayabusa;

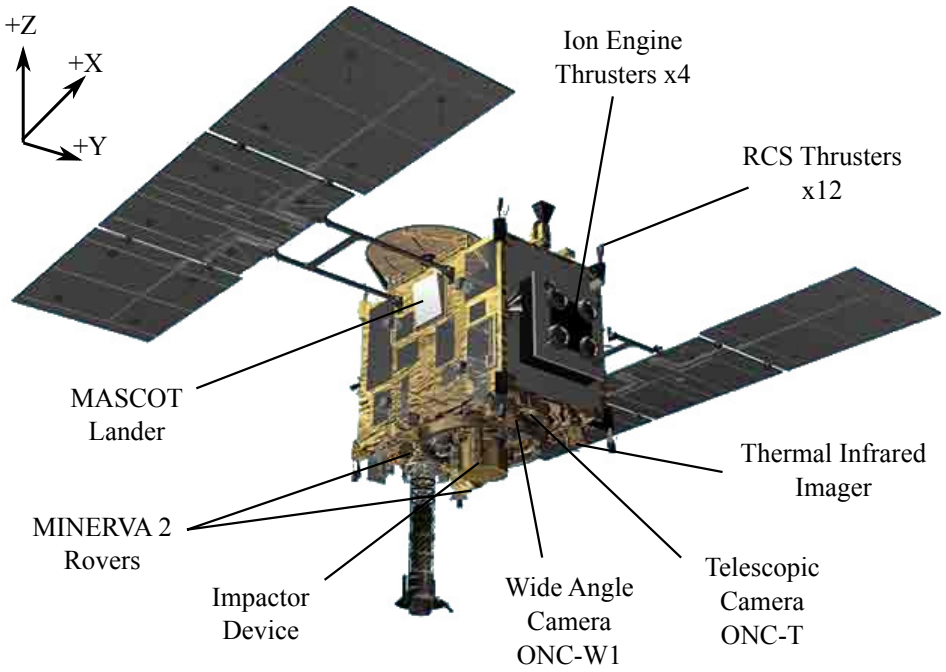

Figure 2.6. Some of Hayabusa 2's instruments, bottom view. Credit: ISAS/JAXA.

Table 2.1. Orientation of Hayabusa 2's relevant instruments.

Acronym	Description	Orientation
IES	ion engines	$+X$
ONC-W2	wide-angle camera	$-Y$
HGA	high-gain antenna	$+Z$
LGA	low-gain antenna	$+Z$
MGA	medium-gain antenna	$+Z$
NIRS3	NIR spectrometer	$+Z$
SAP	solar panels	$+Z$
LIDAR	laser altimeter	$-Z$
ONC-T	telescopic camera	$-Z$
ONC-W1	wide-angle camera	$-Z$
TIR	Thermal IR imager	$-Z$
RCS	reaction control s.	$\pm X, \pm Z$

- NIRS3, a near-infrared spectrometer similar to that of Hayabusa, but with its band adapted to better detect water;
- TIR, a medium-infrared camera inherited from the JAXA Venus exploration mission Akatsuki;
- MINERVA 2, a small rover to be dropped on the surface; a similar rover was also carried by Hayabusa, but failed to land on Itokawa; there may be more

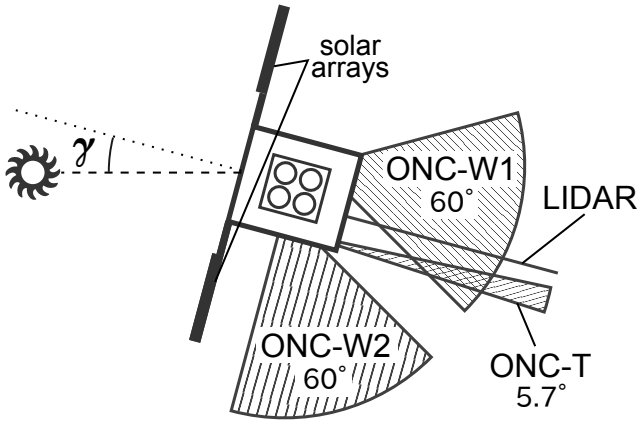

Figure 2.7. Field of view of Hayabusa 2's instruments. The sun-angle γ between the sun direction and the solar panel normal is also shown.

than one rover;

- MASCOT (Mobile Asteroid Surface Scout), a lander developed by the German Aerospace Center (DLR) in collaboration with CNES.

Table 2.1 contains a list of instruments relevant to the design of orbits for Hayabusa 2, including their orientation with respect to the spacecraft-fixed reference frame.

Regarding the trajectories close to the asteroid, the approved mission plan only contemplates hovering, mostly on the line connecting earth and asteroid. No free trajectories of any kind are included in the plan except, like with the predecessor, for the short times prior to and after touch-down, when the tangential velocity will need to be adapted to the asteroid's rotation. Moreover, the probe will have to move to and from the opposite side of the asteroid upon activation of the impactor device, but these trajectories are likely to be highly controlled and far from natural.

The hovering strategy has been selected because it reduces the risks due to the uncertainties in the orbit determination and design. Because the asteroid is very small, the propellant required to counter the gravitational pull is modest, and such an approach is efficient. Were the asteroid much bigger, there would be no choice but to orbit it, and a touch-down would be more difficult to achieve. It is only in recent years that our knowledge of the astrodynamics near a small body has started to grow, and the purpose of this dissertation is to contribute in this field.

2.5.1 Hayabusa 2 Requirements

There are several restrictions that influence the kind of orbit that is desirable for Hayabusa 2. The scale of the orbits should be similar to the gate position distance of 20 km, but at least one close approach per period would be necessary to accomplish the radio science goals.

The position of the instruments also plays an important role. For navigation and orbit determination purposes, Hayabusa 2 uses a laser altimeter (LIDAR), a telescopic camera (ONC-T) and two wide-angle optical cameras (ONC-W1 and ONC-W2), all of which need to point towards the asteroid to operate. Due to the

Table 2.2. Orbital and Physical information for 1999 JU3. Orbital data from the JPL Small-Body Database; physical data from Müller et al. [43].

Symbol	Name	Value	Uncertainty	Unit
e	eccentricity	0.190 245 13	3×10^{-8}	—
a	semi-major axis	1.189 558 056	3×10^{-9}	AU
q	perihelion distance	0.963 250 42	4×10^{-8}	AU
Q	aphelion distance	1.415 865 691	4×10^{-9}	AU
i	inclination	5.884 033	3×10^{-6}	deg
Ω	long. of asc. node	251.616 47	4×10^{-5}	deg
ϑ	arg. of perihelion	211.420 04	4×10^{-5}	deg
T_a	period	473.889 287	2×10^{-6}	days
ω	mean motion	0.759 671 109	3×10^{-9}	deg/day
t_r	rotation period	7.63	1×10^{-2}	hours
R_a	effective radius	435	15	m
H	absolute magnitude	18.82	2×10^{-2}	mag
α	geometric albedo	0.070	6×10^{-3}	—

hovering-centered design of the mission, most of the cameras and the LIDAR point in the opposite direction of the solar panels. The orientation and field of view of the four main instruments are shown in the schematic in Figure 2.7 (the LIDAR divergence is assumed to be 0°). To guarantee continuity in the solar power supply, the angle between the solar array normal and the direction of the sun γ, called *sun angle* should always be $\gamma < 45°$. Moreover, the spacecraft's velocity is mostly measured using the Doppler effect from Earth. It is thus preferable that the velocity vector points towards the earth for as long as possible during a period of the orbit. A final restriction is the necessity to avoid passing through the asteroid's shadow. This automatically invalidates nearly all planar and axi-symmetric trajectories.

These requirements are the focus of Section 10.5, with the objective of identifying the best candidate orbits for Hayabusa 2 among the several studied.

2.6 The Target Asteroid

The target chosen for the Hayabusa 2 mission is asteroid (162173) 1999 JU3, discovered in 1999 by the Lincoln Near-Earth Asteroid Research (LINEAR) project in the United States. It was chosen because of its orbit, which is close to that of the earth and thus relatively easy to reach. In fact 1999 JU3 belongs to the Apollo population of asteroids, having a semi-major axis of 1.2 AU, an eccentricity of 0.19 and a period of 1.3 years. Table 2.2 lists the orbital parameters of 1999 JU3.

Another point of interest of the target is the fact that it is a carbonaceous or C-type asteroid. While accounting for most of the main belt population, C-type asteroids are less common among NEAs, and their lower albedo makes them harder to detect. However, they are spectrally similar to carbonaceous chondrite meteorites, with a composition very similar to the primordial nebula that condensed to form the solar system. To acquire samples of one such body would mean access to first-hand information on the origin of the sun and of its satellite bodies, with great benefit for

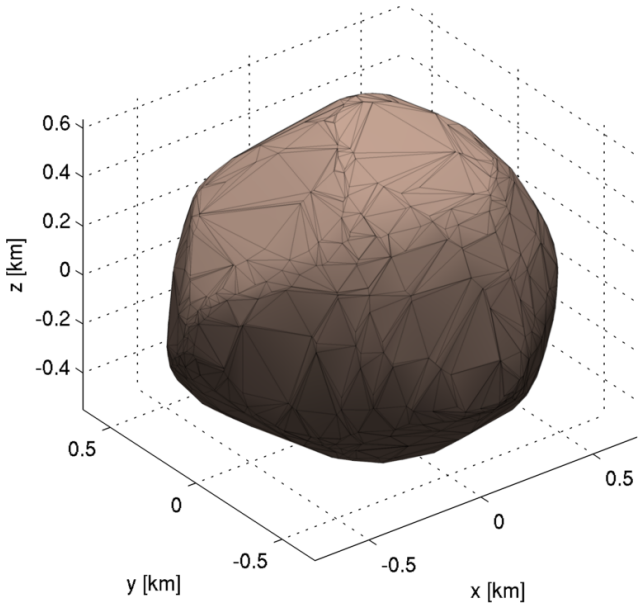

Figure 2.8. View of model `7_1` from Müller et al. [43].

the scientific community. Moreover, carbonaceous asteroids are known to contain hydrated minerals and, sometimes, organic compounds. There is interest among researchers of astrobiology and related fields to study such materials. They could help shed light on the mechanisms of transport and modification of organic matter, and give us hints regarding the beginning of life.

Hasegawa et al. [12] studied observational data on 1999 JU3 from the Subaru Observatory and the Akari infrared astronomy satellite and gave first estimates of the object's physical parameters. The period and spin axis orientation were first estimated by Abe et al. [1] based on light-curve fitting. Further solutions for the asteroid's parameters were given by Campins et al. [7] with data from NASA's Spitzer space telescope, but a more complete revision of all the possible models was performed by Müller et al. [43]. The results of the latter are included in Table 2.2. Further observations with other telescopes confirm and expand these results [30, 44]. Lazzaro et al. [33] studied 1999 JU3's spectra obtained by the SOAR telescope and found no traces of aqueous or thermal alteration on its surface, and suggested that it could be relatively uniform and featureless.

To this moment, no radar observations have been performed on Hayabusa 2's target. Consequently, any information on the asteroid's shape has to be inferred from its light curves. The best estimates are those given by Müller et al., where a total of 84 shape and spin models are tested, covering the full range of possible orientations and conformations. Out of these models, the one that best fits the light-curve data is the one labeled `7_1` (Figure 2.8), whose rotation axis has ecliptic longitude and latitude, respectively, $\lambda_{ecl} = 73.1°$ and $\beta_{ecl} = -62.3°$. However, the data tends to be noisy, and the asteroid's shape is expected to be close to spherical [29]. Therefore, the reliability of model `7_1` is still in doubt until further data is added to the existing pool. The fact that the next two most likely models, `8_2` and `14_8`, have considerably different orientations also hints toward this conclusion.

Throughout this dissertation, we will adopt the values from JPL and from [43] contained in Table 2.2. Note that $e = 0$ is automatically assumed for the simulations in the circular Hill's problem, while the approximation $e = 0.2$ is used for the elliptic problem. We do not use the shape model directly, because in Section 11, where the spherical harmonic terms of the potential are considered, we approximate the shape with a tri-axial ellipsoid. The density, and therefore the mass, of 1999 JU3 is unknown, and probably no additional data on this regard will be available until the rendezvous is actually carried out.

2.7 Previous Results in Small-Body Astrodynamics

The restricted 3-body problem model, developed between the 18^{th} and 19^{th} century by great mathematicians like Euler, Lagrange, Jacobi and Poincaré, approximates very well the motion of a great number of bodies, inside and outside of the solar system. The problem has been studied extensively since then, and listing all the results is outside the scope of this dissertation. Particularly relevant references include Poincaré [50], Broucke [5], and the comprehensive book by Szebehely [61]. The main properties of this formulation are described in Section 4.1.

Hill's problem, described in Section 4.2, is a further approximation of the restricted 3-body problem, valid for orbits close to small secondary bodies. It is a first step towards the accurate modelization of an asteroid or a small moon. Hill's problem is only slightly more recent than the restricted 3-body problem and has been studied extensively itself. It was first used as a basis for a new description of the moon's trajectory [17], and it proved to be more precise than what was previously in use. It was then explored in depth in its planar form, first by Matukuma [35, 36, 37], then by Hénon [14], who found a number of periodic orbits and constructed their families. He and others also applied Hill's problem to various astronomical systems, like binary asteroids and planetary rings [49, 8]. Hénon [16] also found spatial solutions and, more recently, several works provided further insight into the 3–dimensional version of Hill's problem, such as Lara and Scheeres [32], who obtained spatial orbits from bifurcations of the planar ones, and Russel [52] who performed a wide survey of a great number of orbits around Jupiter's moon Europa with a grid search.

More realistic models of an asteroid's environment have been studied somewhat less until now, with a good portion of the results provided by Dr. Daniel J. Scheeres. Most of these results are integrated into the comprehensive book Scheeres [57]. The full problem is dominated by three perturbations that are not considered by the classical Hill's problem:

- the ellipticity of the asteroid's orbit,
- the irregular gravity field and
- solar radiation pressure.

With methods similar to those used in the circular case, Ichtiaroglou [20] derived planar periodic solutions in the elliptic Hill's problem. Scheeres et al. studied the dynamics close to irregular bodies, both for uniform and complex rotators [19, 54]. Constraints on the radius of a circular orbit in the presence of gravity perturbations

and solar radiation pressure are also derived by Scheeres [53, 56]. Of special interest for this work are the results of the averaged effects of solar radiation pressure in the elliptic case, computed by Scheeres [55, 57]. This analysis is based on the result by Mignard and Hénon [40] who showed that the radiation pressure effects, when averaged, are integrable and possess periodic solutions. Scheeres shows that elliptic trajectories around the asteroid are subject to periodic changes in their orbital elements, functions of only the asteroid's true anomaly. He also identifies families of frozen orbits whose elements remain stable as the true anomaly changes. Of these frozen orbits, only one is attainable for a missions like Hayabusa 2, NEAR and OSIRIS-REx. This type or trajectory, called *sun-terminator orbit* lays on a plane that is always perpendicular to the sun-asteroid line, and for the system of interest has a low eccentricity. The properties and some variations of this solution have been studied in detail, and the OSIRIS-REx mission will be the first to apply it [58]. However, sun-terminator orbits are not adequate for the needs of Hayabusa 2 because of their limited observational access to the asteroid (see Section 10.5).

Concerning the solar radiation pressure perturbation with exact methods (as opposed to averaged methods), Morrow et al. [42] and Giancotti and Funase [11] also studied the dynamics of solar sails close to asteroids, and some of the latter's results apply to traditional spacecraft and very small asteroids. Katherine and Villac [24] studied Hill's problem with solar radiation pressure, the same formulation used in this work, and with the same purpose of exploring periodic orbits. However, they applied continuation starting from known solutions in the classical Hill's problem, only for low values of the solar radiation pressure parameter ($\beta < 5$) and only for the circular case.

The most recent results relevant to missions like Hayabusa 2 are by Broschart et al. [4] and Lantoine et al. [31]. They identify the family of *terminator orbits*, strictly related to the sun-terminator orbits studied by Scheeres et al. [58], as the basis for two types of quasi-periodic motions: "sun-side" and "dark-side" *quasi-terminator orbits*. As special cases of these, they also characterize some properties of what they call *resonant terminator orbits* (i.e. periodic orbits) which exist for a wide range of solar radiation pressure regimes.

The work described in this thesis accomplishes two objectives. The first one is to provide a clearer picture, compared to what was previously available, of the solutions of Hill's problem with solar radiation pressure, including information on their stability and on the bifurcation structure of their families. The result on this front, in Chapter 10, is a catalog of 31 plane-symmetric periodic orbits, of which 9 are analyzed in detail with numerical continuation and related tools. Chapter 12 also provides non-periodic stable orbits existing in the elliptic version of the same dynamical problem. The second objective, which is indeed the main motivator for this work, is to provide solutions relevant specifically to the Hayabusa 2 mission. This is done by considering the periodic orbits in the light of various Hayabusa 2 mission design restrictions and requirements (listed in Section 2.5) to recognize the best solutions, and by establishing one way in which the motion could be stabilized through active control.

Part I

Theory and Methods

Chapter 3

The Effects of Solar Radiation on Orbital Dynamics

For most orbital applications in the inner solar system, radiation from the sun is treated as one of the most important disturbances to a satellite's motion. Overlooking its contribution in high-fidelity models for planetary or moon orbiters could lead to grave discrepancies on the medium and long term. When treating with some small-asteroid orbiters, however, radiation pressure may become much more than a perturbation: it can assume the role of fundamental force in the dynamics, at the same level as gravitational attraction. This chapter briefly describes the nature of the different contributions of solar radiation to orbital dynamics, including but not limited to the pressure exerted by photons on the matter they interact with.

3.1 Radiation Pressure

As part of his groundbreaking work on a unified theory of electromagnetism, James C. Maxwell found that light carries, along with energy, its own momentum and thus must exert a force on any body it interacts with [38]. That assertion was published in 1862, but it took roughly 40 more years for someone to prove the claim with a scientific experiment. Too weak to be observed by humans on earth, radiation pressure plays nonetheless an important role in space applications and in the dynamics of the solar system.

The momentum content of a photon is directly related to its energy through the relation $p = E/c$, with c the speed of light. Pressure is momentum transferred for unit time and unit surface, therefore for a given distance R from the sun, the pressure due to its radiation is

$$P = \frac{L_\odot}{4\pi c R^2} \ ,$$

where $L_\odot = 3.839 \times 10^{26}\,\mathrm{W}$ is the solar luminosity, and the energy is spread out on the surface of a sphere of radius R and surface $4\pi R^2$. At the earth, this pressure is $P_\oplus \simeq 4.56\,\mu\mathrm{Pa}$.

Let us now focus on a body of mass m positioned at distance R from the sun and which, for simplicity, has the shape of a bi-dimensional flat surface of area

A. Assume that the body surface is initially oriented perpendicularly with respect to the incident light, so as to have the highest possible cross section, and that it absorbs and reflects the light according to a reflectivity parameter $\rho \in [0, 1]$. Then the acceleration experienced by it is

$$a = \frac{(1+\rho)\, L_\odot}{4\pi c R^2 B} \ , \tag{3.1}$$

where $B = m/A$. The term $(1+\rho)$ accounts for the amount of light that is absorbed (all of it) and that which is reflected specularly (a fraction ρ). This is a simplification, because other radiative effects, like diffuse reflection and thermal radiation, are present in reality. These, however, are generally small and good first approximations can be made even when they are ignored.

In the above description, the acceleration is always parallel to the incident light, whose direction we call $\hat{l}$. On the other hand, when the normal vector to the body's surface has a generic direction $\hat{n}$, the cross section of the body with respect to the light changes. Additionally, the direction of the thrust is affected by the angles, resulting in the following expression valid for perfectly reflecting bodies ($\rho = 1$):

$$\boldsymbol{a} = a\, (\hat{l} \cdot \hat{n})^2\, \hat{n} \ . \tag{3.2}$$

A perfectly absorbing body ($\rho = 0$) follows the modified expression

$$\boldsymbol{a} = a\, (\hat{l} \cdot \hat{n})\, \hat{l} \ , \tag{3.3}$$

while for intermediate values of ρ the acceleration is a combination of (3.2) and (3.3).

Solar radiation pressure's effect is irrelevant for planets and bodies of similar size, but in the long term it can affect the orbital motion of dust particles, asteroids and even the moon [63]. For spacecraft orbiting around planets or the sun, solar radiation pressure is usually a small perturbation, which can be neglected as a first approximation. The exception are solar sails, whose shape, mass and optical properties are selected specifically to maximize the acceleration in (3.1), making possible a new method of propulsion with equivalent specific impulse approaching infinity.

The last case, most relevant to this thesis, is that of a spacecraft orbiting close to a small asteroid. The gravitational field of the asteroid is so small that solar radiation pressure becomes the dominant force for all but the closest approaches. The dynamics is deeply affected by this perturbation, as we will show in Section 4.4.

3.2 Yarkovsky and YORP Effects

The Yarkovsky effect is a small force that arises on any rotating body that orbits in the proximity of a star. It was first described in a pamphlet by Russian engineer Ivan O. Yarkovsky about the effects of the ether (which was still assumed to exist) on small orbiting bodies [65]. The idea was widely ignored and forgotten until it was published again in 1951 in a more modern context by Öpik [47].

The distribution of temperature on a rotating body heated by the sun is always offset in the direction of rotation (see Figure 3.1). The amount of this offset depends

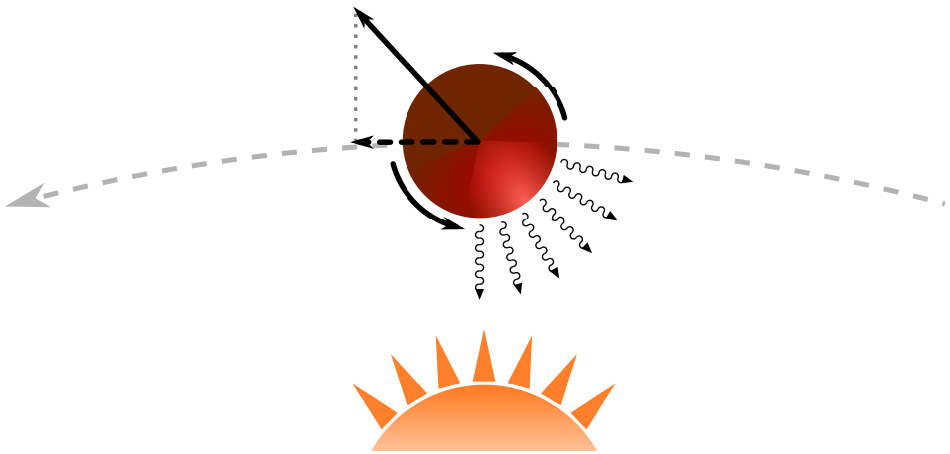

Figure 3.1. Schematic of the Yarkovsky effect.

on several parameters of the body, such as its spin rate and surface thermal properties. As a consequence of this lag, the re-emission of photons in the form of infra-red radiation, as the body cools down, is not completely aligned with the direction of the sun. A small component of the force acts in the direction of motion, directly altering the semi-major axis of the orbit, which takes the form of a spiral. Clearly, the heat distribution on a body in retrograde rotation will tend to lag toward the direction of motion, slowing the body down into an inward spiral. Conversely, a prograde rotator tends to speed up into an outward spiral.

The Yarkovsky effect is usually extremely weak, and can be safely ignored for planets and moons. However its effect might be important, in the long term, for small asteroids. For instance, the first evidence of this effect measured on a natural body was for asteroid 6489 Golevka after several measurements in the 1990s [9]. This 1 km-sized Apollo asteroid receives a thrust of approximately $10^{-10}\,\mathrm{m\,s^{-2}}$, enough to perturb its orbit by 15 km in the course of 12 years. Although small the Yarkovsky effect is considered an important factor when computing the precise trajectories of small bodies and to explain the transport of some asteroids from the main belt to the inner solar system.

The Yarkovsky–O'Keefe–Radzievskii–Paddack (YORP) effect is an additional phenomenon, related to the Yarkovsky effect, responsible for the gradual change of the spin rate of a celestial body. The same cause of the orbital changes described above, i.e. the anisotropy of the thermal emission, can produce torques when the shape of the body is irregular. An emitting surface that is not parallel to the radial direction, forces can arise that speed up or slow down the axial rotation.

This effect was observed for the first time only recently with asteroid 50509 YORP [34], whose spin rate increases by roughly 0.07 °/day in the course of one year. It is believed that such a process might explain in part the distribution of rotational speeds of the known small asteroids, which have higher probabilities of rotating very fast or very slowly compared to the larger bodies.

3.3 Poynting–Robertson Effect

As a final perturbation caused by solar radiation, we mention the Poynting–Robertson effect. This causes a slow decrease in the semi-major axis of a body, which gradually spirals down into the sun. The effect is best understood in the reference frame of the orbiting body: due to the tangential component of its velocity, the *perceived* direction of the incoming light is slightly moved forward. The momentum received from the solar photons, thus, is not perfectly radial, producing a force that slows down the body. This effect is however so small that only objects the size of a grain of dust can be affected by it in reasonably short time-frames. When discussing about asteroids this phenomenon can be generally neglected without consequences. There are nonetheless indications that it may play a measurable role in rare cases [64].

Chapter 4

N-Body Problems

Since the publication of Isaac Newton's *Philosophiae Naturalis Principia Mathematica* in 1687 [46], mathematicians and astronomers have possessed the basic tools to study the motion of planets and stars. These fundamental equations made the dynamics of two gravitationally-bound bodies solvable exactly. This so-called "two-body problem" can in fact be divided into two separate problems, each referring to the motion of a single particle in an external potential. Kepler's three laws of planetary motion, formulated roughly eighty years before Newton's seminal work, were thus explained in a way that was at the same time elegant and irrefutable, at least until the beginning of the twentieth century.

Solution is harder when more than two bodies are considered together. In general, the acceleration of the n particles of an n-body system is described by

$$\ddot{\mathbf{r}}_j = G \sum_{k \neq j} \frac{m_k(\mathbf{r}_k - \mathbf{r}_j)}{|\mathbf{r}_k - \mathbf{r}_j|^3} \qquad j = 1, \ldots, n \ ,$$

where $\mathbf{r}_i$ and m_i are the position vector and the mass of the i-th body, and $G = 6.674 \times 10^{-11}\,\mathrm{N\,m^2\,kg^{-2}}$ is the gravitational constant.

Finding a general analytical solution for such a problem requires a number of constants of motion, or *first integrals* , at least equal to the number of degrees of freedom in the system. For a 3-dimensional n-body system, the latter would be equal to $6n$. Unfortunately, it has been proven in the nineteenth century by Bruns and Poincaré [50] that only exactly 10 algebraic first integrals exist for this kind of dynamics, thus allowing for a reduction of the degrees of freedom to $6n - 10$. A method by Jacobi called "reduction of the nodes" [23] makes use of some symmetries of the system to further reduce by two the number of variables, now down to $6n - 12$. This means that any problem with $n > 2$ is not solvable with the method of first integrals.

Sundman [60] proved that the 3-body problem can be solved with an uniformly convergent infinite series. However, this solution gives little insight on some aspects of the dynamics, and is also impractical due to the extremely high number of terms of the series necessary to reach reasonable accuracy.

Although the $n = 3$ problem is not easily solvable in general, it is still possible to find *particular* solutions for special cases. This kind of approach has been pursued extensively for two centuries, mainly centered on the 3-body problem. Only a

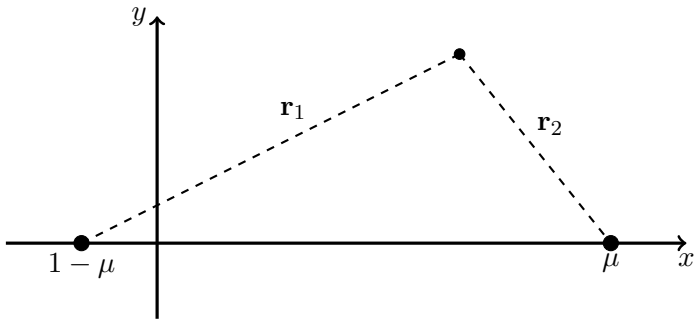

Figure 4.1. The rotating reference frame of the restricted 3-body problem.

handful of solutions are available for three generic masses: among these are the collinear solution, the equilateral triangular solution and the figure eight solution [50, 13, 59]. Besides these exact calculations, numerical methods can in general find an approximation of the solution for any initial configuration. In this work all the trajectories are propagated using the MATLAB function `ode113`, a variable order solver based on the Adams–Bashforth–Moulton multi-step method.

4.1 The Restricted 3-Body Problem

Scholars of celestial mechanics had a greater success with a more specific case of the 3-body problem: the *restricted* 3-body problem [22, 61]. In this case one of the three bodies is assumed to have a much smaller mass then the other two. The two large bodies, called the *primaries*, orbit each other with simple 2-body dynamics, unaffected by the third mass, sometimes called the *particle*. This configuration is of particular interest, because it closely resembles real-world systems like sun-planet-moon or sun-planet-spacecraft. Note that unless otherwise stated, here and throughout this work we assume point-like masses for all the bodies.

4.1.1 Equations of Motion and Jacobi Constant

In order to make the expressions of the dynamics easier to handle, we can transform the coordinates and the physical units of the system. We apply a scaling so that the sum of the masses of the primaries is unitary. As a consequence, the mass of the smaller primary becomes

$$\mu = \frac{m_2}{m_1 + m_2} \ ,$$

where m_1 and m_2 are the original masses of the larger and smaller primary, respectively. Consequently, the mass of the larger one is scaled $1 - \mu$, while the mass of the particle here is always equal to zero. We then define the new unit of length such that the distance R between the primaries is, again, unitary. Finally, the choice of $G = 1$ gives us also a new time unit. In fact, the expression of the period of a

circular Kepler orbit is

$$\frac{T}{2\pi} = \frac{1}{\omega} = \sqrt{\frac{R^3}{G(m_1 + m_2)}} \ , \tag{4.1}$$

where T is the orbital period and ω the angular velocity, and if we apply the above normalizations, we see that $T/2\pi = 1$.

We then position the origin of the reference frame at the center of mass of the primaries and assume that the x and y axes lie on the orbital plane. The whole frame rotates around the angular momentum vector at the same mean rate $\omega = 1$. If the primaries draw the shapes of two circles, the problem is called *circular* restricted 3-body problem, otherwise the term is preceded by the word *elliptic*. The latter case is more complex, involving a forced pulsation of the equations of motion. In the scope of this thesis, the term "restricted 3-body problem" will refer to the circular restricted case, unless differently stated.

The distance of the two bodies from the center of mass is inversely proportional to their masses. Then, if we fix the primaries on the x axis, the larger one will occupy the position $(-\mu, 0, 0)$ and the smaller one $(1-\mu, 0, 0)$. Only the particle is free to move around. Figure 4.1 illustrates the various aspects of this rotating reference frame. After defining the two distances of the particle from the primaries as

$$\begin{aligned} r_1 &= \sqrt{(x+\mu)^2 + y^2 + z^2} \\ r_2 &= \sqrt{(x-1+\mu)^2 + y^2 + z^2} \ , \end{aligned}$$

we can express the effective potential of the system,

$$U(x, y, z) = \frac{x^2 + y^2}{2} + \frac{1-\mu}{r_1} + \frac{\mu}{r_2} \ . \tag{4.2}$$

This potential accounts not only for the gravitational attractions, but also for the centrifugal force that arises in a rotating reference frame.

The equations of motion of the restricted 3-body problem are

$$\ddot{x} = U_x + 2\dot{y} \tag{4.3a}$$

$$\ddot{y} = U_y - 2\dot{x} \tag{4.3b}$$

$$\ddot{z} = U_z \ , \tag{4.3c}$$

where the expression U_q means differentiation of U with respect to variable q and the dot ($\dot{}$) and double dot ($\ddot{}$) respectively indicate the first and second derivatives with respect to time. The first two equations contain, besides the derivatives of the potential, also terms due to the Coriolis Force. Associated with these equations is an integral of motion, the *Jacobi constant* or energy. It is promptly derived by multiplying each of (4.3) respectively by $\dot{x}$, $\dot{y}$ and $\dot{z}$, then summing the three equations and integrating them in time,

$$\int (\dot{x}\ddot{x} + \dot{y}\ddot{y} + \dot{z}\ddot{z}) \ dt = \int \left(\frac{\partial U}{\partial x}\frac{dx}{dt} + \frac{\partial U}{\partial y}\frac{dy}{dt} + \frac{\partial U}{\partial z}\frac{dz}{dt} \right) dt \ ,$$

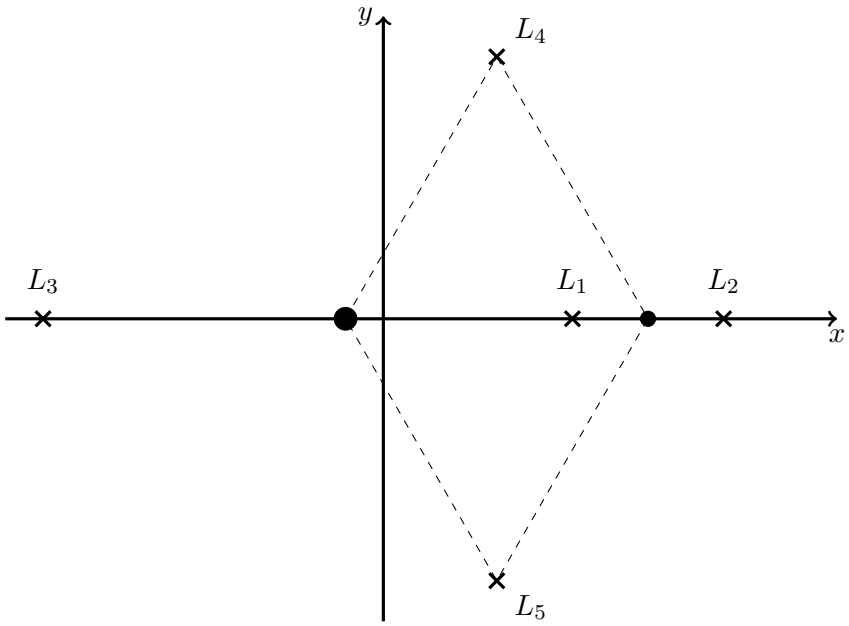

Figure 4.2. The equilibrium points in the restricted 3-body problem.

which leads to

$$C = \frac{1}{2}\left(\dot{x}^2 + \dot{y}^2 + \dot{z}^2\right) - U \ , \tag{4.4}$$

where C is the Jacobi constant. Note that another expression of the Jacobi constant is often used, related to the above definition as $C^* = -2C$. In this work we select Eq. (4.4) as the preferred definition. Following the normalization of the previous subsection, the values of C are hereafter considered adimensional.

4.1.2 Equilibrium Points and Zero-Velocity Surfaces

The above equations give us information about the kind of motion that is allowed to the particle. Central to the discussion of these 3-body problem dynamics are the equilibrium points that arise from (4.3) when the left side of the system is equal to zero. In the current configuration five such *libration points* exist, labeled L_i, $i = 1, \ldots, 5$ (see Figure 4.2). If the particle is placed on one of these points with zero velocity, it will remain there forever.

The first three libration points, L_1, L_2 and L_3, all lie on the x axis, and their positions are found by solving a quintic equation [61]. L_4 and L_5, on the other hand, are located symmetrically above and below the x axis, forming two equilateral triangles with the primaries. The energy required to remain still at one libration point is different in every case, except L_4 and L_5, which have the same energy.

After fixing the mass ratio μ and a particular value of the Jacobi constant C^*, (4.4) translates into a constraint on the regions of space where motion is allowed, called *Hill's regions*. The condition $\dot{x}^2 + \dot{y}^2 + \dot{z}^2 = 0$ determines the boundary surfaces between regions of space where motion is possible and those where it is

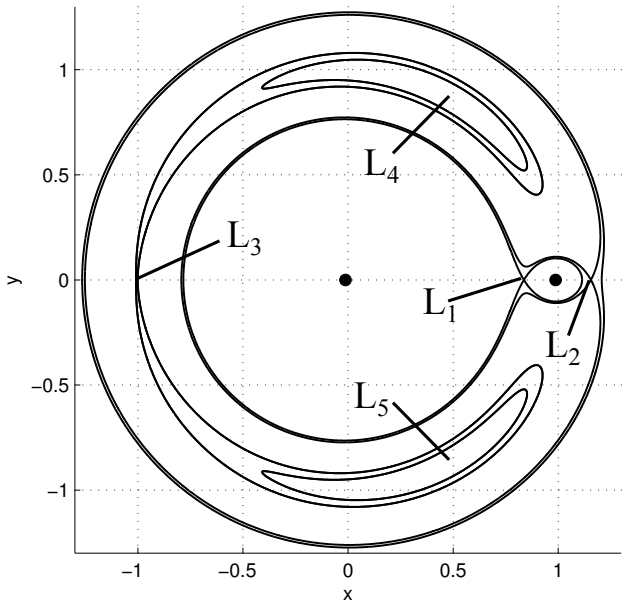

Figure 4.3. Section of the zero-velocity surfaces for the restricted 3-body problem with earth-moon masses.

impossible:

$$S_{ZVC} = \{(x, y, z) \,|\, C(x, y, z, 0, 0, 0) = C^*\} \ . \tag{4.5}$$

These surfaces are called *zero velocity surfaces* (ZVS) in the spatial case, and *zero velocity curves* (ZVC) in the planar restricted 3-body problem. Figure 4.3 shows the shape of the zero-velocity surfaces for the earth-moon system ($\mu = 0.0122$) and for different values of C, limited to the x–y plane.

As can be seen in Figure 4.3, the zero-velocity surfaces are shaped around these libration points. If we call C_i the value of the Jacobi constant for which the velocity is null at L_i, the following cases are possible:

1. $C^* \leqslant L_{4/5}$: motion is allowed everywhere;

2. $L_{4/5} < C^* < L_3$: two regions, around L_4 and L_5, are not reachable;

3. $L_3 < C^* < L_2$: the zero-velocity surfaces form a "barrier" between the region close to the earth and distances greater than 1, but passage is still possible around the smaller primary;

4. $L_2 < C^* < L_1$: the passage at L_2 is closed, and the particle can either remain forever in the outer region or move between the regions close to the two primaries

5. $C^* > L_1$: also the L_1 passage is closed, confining any motion either around one of the primaries or in the outer region.

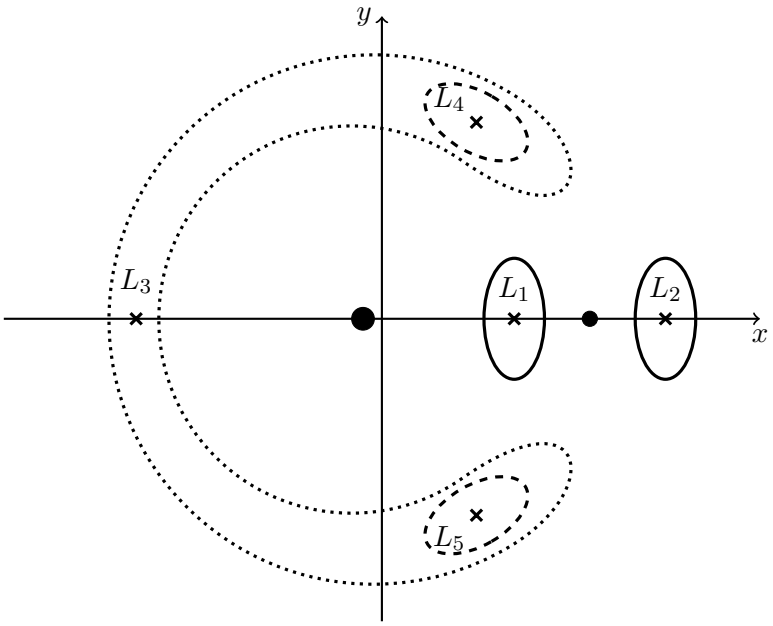

Figure 4.4. Schematic representation of planar periodic orbits in the restricted 3-body problem. Solid lines: Lyapunov orbits. Dashed lines: tadpole orbits. Dotted line: horseshoe orbit.

4.1.3 Periodic Orbits

Although, as stated previously, the 3-body problem admits in practice no general solution, researchers in the past decades have found with numerical methods and studied in detail a plethora of periodic orbits in the restricted 3-body problem [61]. In the planar case, each libration point is associated to a family of orbits revolving around it. Orbits around one of the collinear points are called *Lyapunov orbits*, whereas those around the equilateral points L_4 and L_5 are known as *tadpole orbits*. These orbits are shown schematically in Figure 4.4.

For each value of C the orbits take on different sizes and shapes, eventually bifurcating into new families, such as the *horseshoe orbits* that oscillate back and forth between L_4 and L_5 passing close to L_3. Numerical methods can also reveal other types of periodic orbits that revolve around the primaries in some kind of resonance with the system's rotation.

In the spatial case, we know of an even wider variety of trajectories. Of greatest interest are the orbits close to L_1, L_2 and the smaller primary, such as the vertical orbits, halo orbits and an intricate network of other orbits that connect them to the planar ones. A graphical overview of the various solutions and their relations is given, for instance, in [10].

Quasi-periodic orbits are another important set of solutions in the restricted 3-body problem. Although not periodic in the strict sense, they display a bounded and repetitive behavior. The intuitive reason behind these properties is that they are the composition of an oscillation in the x–z plane and another on in the z direction. In general these two oscillations have non-commensurable periods, thus the trajectory never closes but always remains in the same subspace. Families of

quasi-periodic orbits called *Lissajous orbits* exist in relation to the Lyapunov orbits, close to the first two equilibrium points [18]. Halo orbits are also accompanied by vast families of quasi-periodic orbits.

4.2 Hill's Problem

While the restricted 3-body problem is a special case of the generic 3-body problem, Hill's problem is itself a special case of the restricted 3-body problem. It was first studied by George W. Hill at the end of the nineteenth century in his efforts to produce a reliable theory that could describe the perturbations of the orbit of the Moon [17]. His formulation, later improved upon by Ernest W. Brown raised considerably the quality of the Moon's orbital predictions and was used systematically for most of the twentieth century.

4.2.1 The Potential in Hill's Approximation

The approximation introduced in Hill's theory is to consider trajectories very close to the smaller primary ($r_2 \ll r_1$) whose mass, moreover, is much smaller than that of the other primary ($\mu \ll 1$). Starting with the potential of the restricted 3-body problem in (4.2) we first move the origin to coincide with the smaller primary (*central body* from now on), i.e. $x \to x - (1-\mu)$. The potential becomes

$$U = \frac{x^2+y^2}{2} + (1-\mu)\,x + \frac{1-\mu}{\sqrt{(x+1)^2+y^2+z^2}} + \frac{\mu}{\sqrt{x^2+y^2+z^2}} \ , \qquad (4.6)$$

where constant terms have been dropped, being irrelevant to the dynamics.

We then apply the first approximation, expanding the third term on the right in Eq. (4.6) and discarding all terms with powers greater than 2 (which is equivalent to discarding powers greater than 1 from the equations of motion):

$$\frac{1-\mu}{\sqrt{(x+1)^2+y^2+z^2}} \simeq (1-\mu)\left[1 - x + x^2 - \frac{1}{2}(y^2+z^2)\right]$$

The potential becomes

$$U = \frac{\mu}{2}\left(x^2+y^2+z^2\right) + \frac{3}{2}(1-\mu)\,x^2 - \frac{1}{2}z^2 + \frac{\mu}{\sqrt{x^2+y^2+z^2}} \ ,$$

after, once again, dropping constant terms. Because both the components (x, y, z) and the massμ are small in the current units, we neglect those terms where they are multiplied. We obtain

$$U = \frac{3}{2}x^2 - \frac{1}{2}z^2 + \frac{\mu}{r} \ ,$$

where $r = \sqrt{x^2+y^2+z^2}$. As a last modification, we convert the units so that $\mu \to 1$. The final form of the potential in Hill's problem is

$$U = \frac{3}{2}x^2 - \frac{1}{2}z^2 + \frac{1}{r} \ . \qquad (4.7)$$

Note that the unit of time remains unchanged from the restricted 3-body problem as $1/\omega$ and we also keep $G = 1$. Consequently the above change in mass unit affects the unit of length. In fact from (4.1) we notice that only a transformation $r \to r\,(m_2\,/\,m_1)^{1/3} \simeq r\mu^{1/3}$ would keep the term in the square root constant. The new unit of length is thus $r_H = R\mu^{1/3}$, where r_H is called Hill's radius. This is a critical distance in Hill's problem. In fact, if we re-expand temporarily μ into its defining form,

$$r_H = R\left(\frac{m_2}{m_1+m_2}\right)^{\frac{1}{3}} = \left(\frac{m_2}{(m_1+m_2)\,/R^3}\right)^{\frac{1}{3}} = \left(\frac{Gm_2}{\omega^2}\right)^{\frac{1}{3}} \ ,$$

which leads to

$$\omega = \sqrt{\frac{Gm_2}{r_H^3}} \ ,$$

hence r_H is a "resonance radius" with which a circular orbit would revolve around the central body at the rate ω.

4.2.2 Equations of Motion and Jacobi Constant

The equations of motion in Hill's problem have the same form as (4.3). Carrying out the differentiation of $U(x, y, z)$, we obtain a more explicit expression:

$$\ddot{x} - 2\dot{y} = -\frac{x}{r^3} + 3x \tag{4.8a}$$

$$\ddot{y} + 2\dot{x} = -\frac{y}{r^3} \tag{4.8b}$$

$$\ddot{z} = -\frac{z}{r^3} - z \ . \tag{4.8c}$$

Like in the restricted 3-body problem, also in Hill's problem there is a constant of motion called Jacobi constant. Its expression and derivation is identical to that of (4.4),

$$C = \frac{1}{2}\left(\dot{x}^2 + \dot{y}^2 + \dot{z}^2\right) - U \ ,$$

where now the potential has the new form of Eq. (4.7)

4.2.3 Equilibrium Points and Zero-Velocity Surfaces

In a way analogous to that followed for the 3-body problem, the boundaries of the regions of allowed and forbidden motion are found from considerations on the potential U. Their shapes, however, differ slightly from the preceding case, as shown in Figure 4.5.

Unlike those shown in Figure 4.3, in this case the zero-velocity surfaces are exactly symmetrical with respect to the smaller primary. This is because of our approximation, where the larger primary is considered to be located at an infinite distance to the left of the plot. What was previously very close to an arc of a circle, in these new formulation takes on a rectilinear shape.

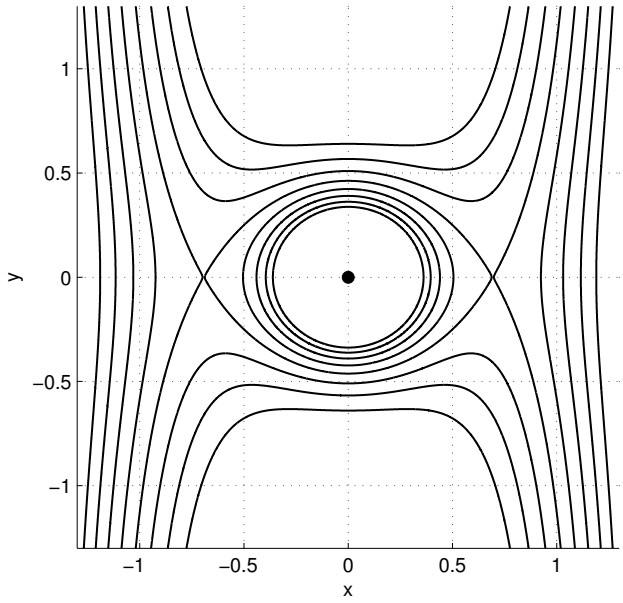

Figure 4.5. Zero-velocity surfaces and libration points in Hill's Problem.

Out of the five equilibrium points of the restricted case, only L_1 and L_2 remain in Hill's problem. Their locations are easily obtained by equating (4.8) to zero,

$$x = \pm \left(\frac{1}{3}\right)^{\frac{1}{3}} \qquad y = 0 \qquad z = 0 \ .$$

L_1 and L_2 are shown in Figure 4.5.

4.3 Hill's Problem with Radiation Pressure

This research concentrates on a special case of Hill's problem where, along with the real and apparent forces described above, there is an additional term accounting for the solar radiation pressure effect on the spacecraft. This is sometimes called *augmented Hill's problem*.

The nominal magnitude of the solar radiation pressure acceleration is given by (3.1). To use it in Hill's problem, its expression needs to be normalized along with the other terms. After dividing by the unit of acceleration $G\, m_1^{2/3} m_2^{1/3}/R^2$, we obtain the following parameter that no longer depends on the distance from the sun:

$$\beta = \frac{(1+\rho)\, L_\odot}{4\pi c B G m_1^{2/3} m_2^{1/3}} \ .$$

The value of β thus depends on the properties of the spacecraft (mass, exposed area and reflectivity) and on the mass of the asteroid, but not on the sun-asteroid distance. There is some uncertainty in the values related to the spacecraft, especially for the actual mass during the rendezvous, which is affected by the previous operations.

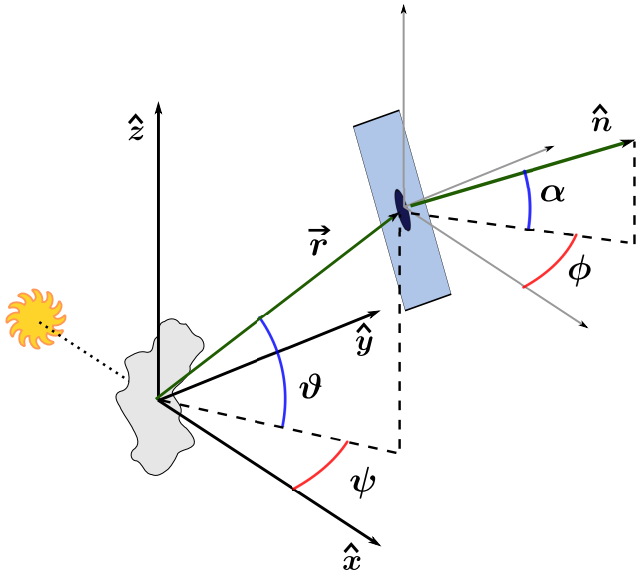

Figure 4.6. Solar sail coordinate system and angles.

However the asteroid's mass is the largest unknown in the problem, with a range of possible values from 1.7×10^{11} kg to 14×10^{11} kg [21]. As a consequence of these uncertainties, β could have a minimum value of roughly 20 to a maximum one of 55, with the most probable candidates around 30. In the following chapters, we will explore scenarios with different values for β, mostly focused on the range from 27 to 33.

The behavior of the spacecraft with radiation pressure is determined by the model that we choose. Here the preferred formulation is the so-called *cannonball model*, which assumes a spherical shape and homogeneous optical properties. In this case, then, the acceleration is always directed away from the sun, just like the case of the flat spacecraft perpendicular to the light direction discussed in Section 3.1.

Before describing the augmented Hill's problem in the form that will be used for the rest of this dissertation, let us briefly look at a more general formulation of the problem, valid for spacecraft with very high area-to-mass ratio such as solar sails.

4.3.1 Solar Sail Model and Artificial Equilibrium Points

A solar sail's attitude close to a small asteroid can drastically change the structure of Hill's problem's solutions. We can see this, for instance, by looking for the equilibrium points that can be attained by the spacecraft by adjusting its attitude. Instead of just two points, a solar sail can create whole surfaces of artificial equilibrium points [11].

We begin by expressing the acceleration in spherical coordinates. The position of the spacecraft is given by its distance r from the asteroid, its angle ψ on the x–y plane with respect to the x axis, and its angle ϑ out of the x–y plane (Figure 4.6). The attitude of the sail is similarly defined by the two angles formed by the sail normal vector $\hat{n}$: φ parallel to the x–y plane and α in the direction normal to it.

From Eqs. (3.2) and (3.3) we obtain the three components of the acceleration,

$$\begin{aligned} a_x &= \rho\, a_r \cos^3\alpha \cos^3\varphi + (1-\rho)\,\frac{a_r}{2}\cos\alpha\cos\varphi \\ a_y &= \rho\, a_r \cos^3\alpha \cos^2\varphi \sin\varphi \\ a_z &= \rho\, a_r \cos^2\alpha \cos^2\varphi \sin\alpha \ , \end{aligned}$$

where, for ease of formulation, we have defined the acceleration of the reflecting part as $a_r = \beta(\rho = 1)$ and that of the absorbing part as $a_r/2 = \beta(\rho = 0)$. Because the equations of motion in Cartesian coordinates are

$$\begin{aligned} \ddot{x} - 2\dot{y} &= -\frac{x}{r^3} + 3x + a_x \\ \ddot{y} + 2\dot{x} &= -\frac{y}{r^3} + a_y \\ \ddot{z} &= -\frac{z}{r^3} - z + a_z \ , \end{aligned}$$

imposing all the derivatives to be null gives us the equations for the equilibrium points,

$$\begin{aligned} 0 = &\left(3r - \frac{1}{r^2}\right)\cos\vartheta\cos\psi \\ &+ \rho\, a_r \cos^3\alpha\cos^3\varphi + (1-\rho)\,\frac{a_r}{2}\cos\alpha\cos\varphi \qquad (4.9a) \\ 0 = &-\frac{1}{r^2}\cos\vartheta\sin\psi + \rho\, a_r\cos^3\alpha\cos^2\varphi\sin\varphi \qquad (4.9b) \\ 0 = &-\left(r + \frac{1}{r^2}\right)\sin\vartheta + \rho\, a_r\cos^2\alpha\cos^2\varphi\sin\alpha \ . \qquad (4.9c) \end{aligned}$$

Next, we will study the above equations in three cases.

In the hypothesis that the spacecraft is a perfectly absorbing body, which doesn't reflect any light, the identity $\rho = 0$ and Eqs. (4.9b) and (4.9c) imply that ϑ and ψ are 0 or π, while φ and α are independent from them. The only equation left is

$$3r^3 \pm \frac{a_r}{2} r^2 \cos\gamma - 1 = 0 \ , \qquad (4.10)$$

where γ is the angle of the sail with respect to the $+x$ axis in any direction, i.e. $\cos\gamma = \cos\alpha\cos\varphi$. The equilibrium points are thus located on the x axis, and their positions are given by the solutions of (4.10).

The second case is that of a perfectly reflecting solar sail with $\rho = 1$. Here the attitude of the spacecraft becomes important, and solutions exist outside of the x axis, forming 2-dimensional surfaces in 3-dimensional space. Figure 4.7a shows the $z = 0$ section of the equilibrium solutions in this case, including the attitude angles required to obtain them. The dotted circle is equal to Hill's radius r_H, to which the positions are normalized.

Finally we come to the case of a generic $\rho \in (0, 1)$. Here the solutions must satisfy Eqs. (4.9), and the equilibrium solutions vary strongly depending on the value of ρ. This variation is displayed in Figure 4.7b, for $\mu = 1 \times 10^{16}$ kg and the assumed value of β. The night-side curves quickly shrink towards the x axis, because the

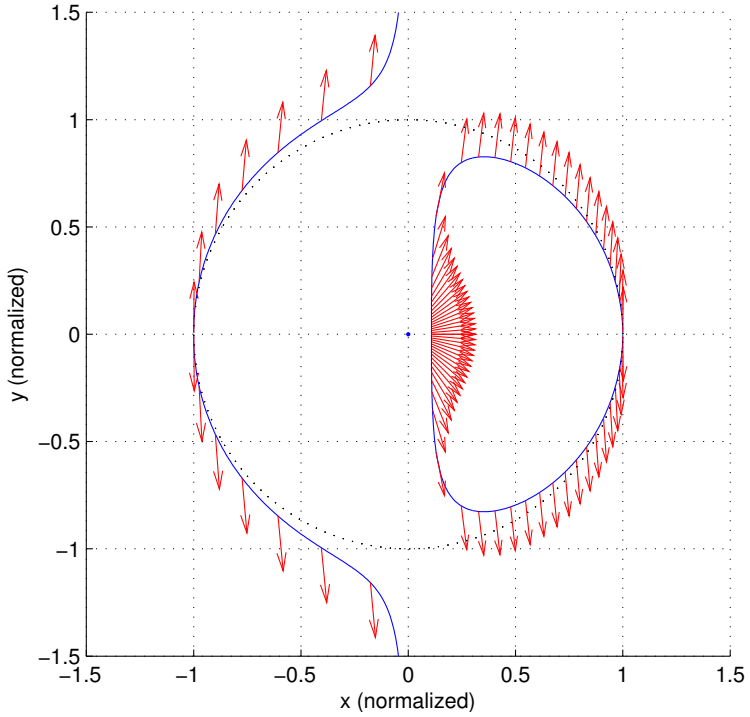

(a)

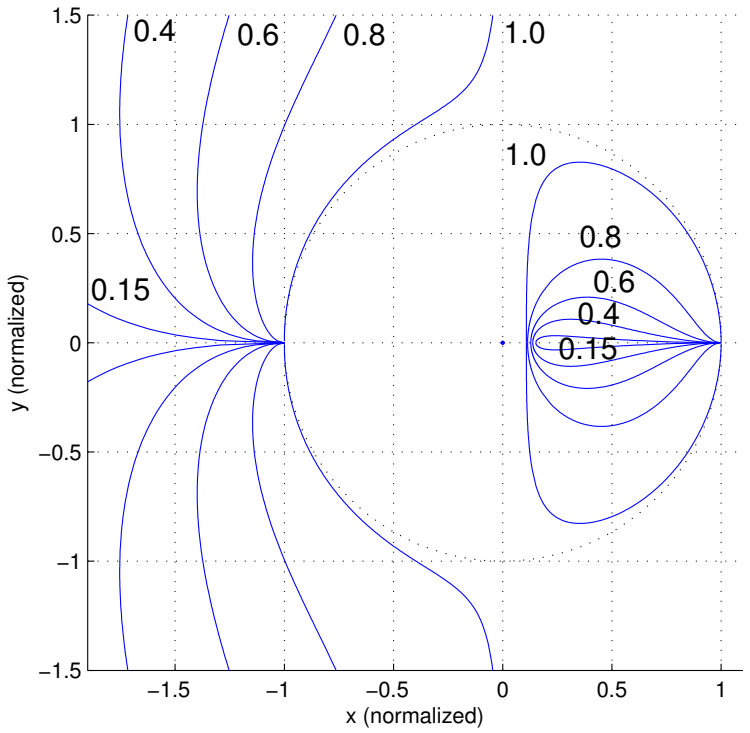

(b)

Figure 4.7. (a) Equilibrium solutions for a perfectly reflecting solar sail, x–y plane section. The φ attitude angle is shown with red arrows, while $\alpha = 0$ everywhere. (b) Section of the equilibrium surfaces for different reflectivity indices (labeled) when $\mu = 1 \times 10^{16}$ kg.

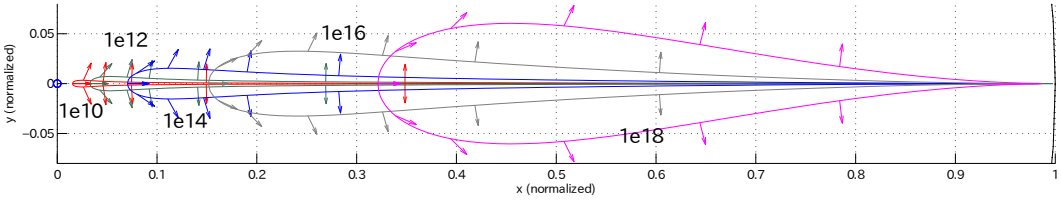

Figure 4.8. Night-side equilibrium surfaces when $\rho = 0.15$ for different asteroid masses (labeled, units in kg).

increasing absorption leads to lower tangential accelerations. On the day side the solutions move away from the $r = r_H$ sphere as ρ is reduced, but on both sides they remain tangent to it at the libration points, which again are when the sail angle is normal to the radiation. The shapes are similar also on the x–z plane section. The curves on the night side of the asteroid are shown in more detail for $\rho = 0.15$ in Figure 4.8, comparing the solutions for different asteroid masses.

Apart from the equilibrium points, the dynamics of a solar sail close to an asteroid have not been studied in detail yet. Hayabusa 2 has a relatively high area-to-mass ratio, but its properties are still far from those of a solar sail. Therefore we will not attempt to delve into the detailed dynamics of this general problem, and we will concentrate on the more manageable cannonball approximation.

4.3.2 Cannonball Model

The radiation pressure on a spacecraft like Hayabusa 2 is well described by the cannonball model, a special case of the solar sail model where the attitude angles α and φ are identically zero. Now the pressure term has the useful property of being constant. In this case we can formulate the perturbation as a simple contribution to the potential:

$$U(\boldsymbol{x}, \beta) = \frac{1}{r} + \frac{3}{2}x^2 - \frac{1}{2}z^2 + \beta x \ .$$

The Jacobi constant takes the same form as Eq. (4.4). The related equations of motion are

$$\begin{aligned} \ddot{x} - 2\dot{y} = U_x &= -\frac{x}{r^3} + 3x + \beta \\ \ddot{y} + 2\dot{x} = U_y &= -\frac{y}{r^3} \\ \ddot{z} = U_z &= -\frac{z}{r^3} - z \ . \end{aligned}$$

For numerical applications, this kind of second-order system is usually transformed

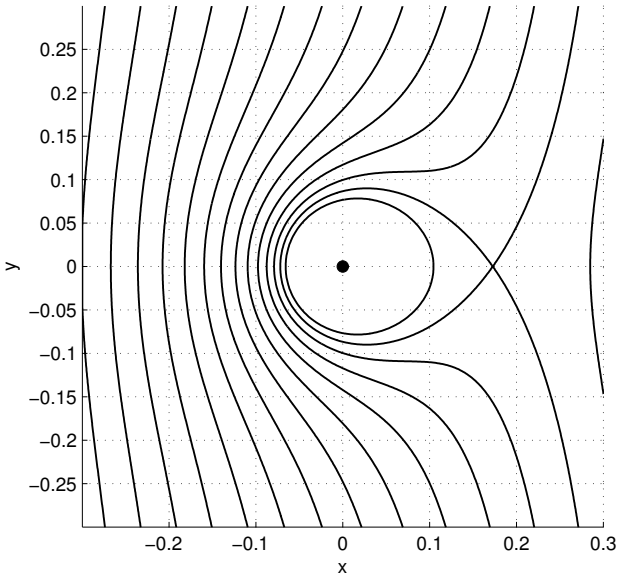

Figure 4.9. Zero velocity surfaces in the augmented Hill's problem with $\beta = 33$.

into a first-order one, namely

$$\begin{aligned}
\dot{x} &= v_x \\
\dot{y} &= v_y \\
\dot{z} &= v_z \\
\dot{v}_x &= -\frac{x}{r^3} + 3x + 2v_y + \beta \\
\dot{v}_y &= -\frac{y}{r^3} - 2v_x \\
\dot{v}_z &= -\frac{z}{r^3} - z \ ,
\end{aligned} \tag{4.11}$$

where we have defined the x, y and z components of the velocity as v_x, v_y and v_z respectively. This form of the dynamics, which we will call "augmented Hill's problem", will be assumed in the rest of this work, except for the computations that involve a non-zero ellipticity of the asteroid's orbit.

We can have an idea of the influence of β on the motion of the spacecraft by looking, once again, at the zero-velocity surfaces. These appear in Figure 4.9, where they are shown for different values of C keeping β constant. The force, acting from left to right, makes these shapes asymmetric, and alters the positions of the equilibrium points. As β increases, L_2 moves closer to the asteroid, while L_1 moves farther and farther until it is too far to be of interest for rendezvous operations. For high-β (or low-energy) regimes the passage on the left of the asteroid, at L_1, is usually closed, restricting the motion to close distances from the origin. This is always the case for Hayabusa 2 and similar missions. On the opposite side the region at L_2 remains open until much higher values of β, making an right-side escape from the asteroid's gravity a concern for a real mission.

4.4 Elliptic Hill's Problem with Radiation Pressure

We now go one step further and generalize the equations to work with a central body on an elliptic orbit around the sun. Not only we include the effect of solar radiation pressure, but also that of the non-constant distance from the sun. The steps of this derivation are the same as those we followed for the circular problem, but additional care is needed because of the time-dependence of the elliptic problem's dynamics.

In the equations of motion of the restricted 3-body problem, Eqs. (4.3), we assumed the angular velocity ω of the system to be constant, and we normalized it to unity. We could therefore, omit it from the expression of the equations of motion. When the orbits are no longer circular, ω, as well as the distance R between the primaries, vary with time. They are expressed as

$$R(\nu) = \sigma^{-1} p \tag{4.12}$$

$$\omega(\nu) = \dot{\nu} = \sigma^2 p^{-\frac{3}{2}} \ , \tag{4.13}$$

where ν is the true anomaly of the smaller primary's orbit, e its eccentricity, p its semi-latus rectum and

$$\sigma = 1 + e\cos\nu$$

is a pulsating quantity that we will call *elliptic factor*. The normalization of distances is still valid for the orbit's semi-major axis a, which is constant and unitary. The semi-latus rectum is related to the semi-major axis by $p = a(1 - e^2)$.

4.4.1 Equations of Motion in the Pulsating Reference Frame

We rewrite the equations of motion (4.3) in the general problem where $e \neq 0$. We now have to include explicitly ω because it is not constant any more:

$$\ddot{\xi} = \Omega_\xi + 2\,\omega\dot{\eta} + \dot{\omega}\eta \tag{4.14a}$$

$$\ddot{\eta} = \Omega_\eta - 2\,\omega\dot{\xi} - \dot{\omega}\xi \tag{4.14b}$$

$$\ddot{\zeta} = \Omega_\zeta \ , \tag{4.14c}$$

where, compared to (4.3), (4.14) each have one additional term in $\dot{\omega}$. This term is the Euler force, absent only in uniformly rotating reference frames. The potential is

$$\Omega(\xi,\,\eta,\,\zeta) = \frac{\xi^2 + \eta^2}{2}\omega^2 + \frac{1-\mu}{r_1} + \frac{\mu}{r_2} + a_{\mathrm{srp}}\,\xi \ , \tag{4.15}$$

where a_{srp} is the radiation pressure acceleration (3.1) and the derivative of ω is

$$\dot{\omega} = \ddot{\nu} = -2\,\omega^2\sigma^{-1} e\sin\nu \ .$$

In the following developments we will also need the first derivatives of R with respect to ν, represented as a prime mark ($'$):

$$R' = \sigma^{-2} p\, e\sin\nu \tag{4.16}$$

$$R'' = p\left(2\,\sigma^{-3}e^2\sin^2\nu + \sigma^{-2}e\cos\nu\right) \ . \tag{4.17}$$

At this point we can make a transformation of the coordinates that factors out the pulsating distance term, $(\xi,\, \eta,\, \zeta) = (Rx,\, Ry,\, Rz)$. From (4.16) and (4.17), we can write the time derivatives of ξ as

$$\dot{\xi} = p^{-\frac{1}{2}} \left(x'\sigma + xe \sin \nu \right) \tag{4.18}$$

$$\ddot{\xi} = \sigma^3 p^{-2} \left[x'' + x \left(1 - \sigma^{-1} \right) \right] \ , \tag{4.19}$$

where we have used the chain differentiation rule. Similar expressions hold for η and ζ. Apply the coordinate transformation and substitute (4.18)–(4.19) into the equations of motion to obtain

$$x'' = \sigma^{-2} p \, \Omega_x + 2\, y' - x \left(1 - \sigma^{-1} \right) \tag{4.20a}$$

$$y'' = \sigma^{-2} p \, \Omega_y - 2\, x' - y \left(1 - \sigma^{-1} \right) \tag{4.20b}$$

$$z'' = \sigma^{-2} p \, \Omega_z - z \left(1 - \sigma^{-1} \right) \tag{4.20c}$$

We then apply the transformations necessary to arrive at the elliptic formulation of Hill's problem. In our new pulsating reference frame, (4.15) becomes

$$\Omega(x,\, y,\, z) = \frac{x^2 + y^2}{2} R^2 \omega^2 + \frac{1 - \mu}{R\, r_1} + \frac{\mu}{R\, r_2} + a_{\text{srp}} R x \ .$$

Then, in a single step, we apply the approximation $\mu \ll 1$, move the origin to coincide with the second primary and expand the fraction in r_1 to the second order in x, y and z. We also use Eq. (4.12):

$$\Omega = \sigma^2 p^{-1} \Bigg[\left(\frac{1}{2} + \sigma^{-1} \right) x^2 + \frac{1}{2} \left(1 - \sigma^{-1} \right) y^2 - \frac{1}{2} \sigma^{-1} z^2 + \\ + \left(1 - \sigma^{-1} \right) x + \sigma^{-1} \frac{\mu}{r_2} + \sigma^{-1} a_{\text{srp}} R^2 x \Bigg] \ ,$$

where we have dropped any term that does not depend on the coordinates.

We proceed from here by defining a new function

$$\hat{U} = \left(\frac{3}{2} x^2 + \frac{\mu}{r_2} + a_{\text{srp}} R^2 x \right) \ ,$$

so that Ω can be written as

$$\Omega = \sigma^2 p^{-1} \left[\sigma^{-1} \hat{U} + \frac{1}{2} \left(1 - \sigma^{-1} \right) \left(x^2 + 2x + y^2 + z^2 \right) - \frac{1}{2} z^2 \right] \ .$$

Inspection of Eqs. (4.20) reveals that many terms of Ω cancel out, leaving us with a cleaner form of the equations of motion:

$$\begin{aligned} x'' &= \sigma^{-1} \hat{U}_x + 2y' \\ y'' &= \sigma^{-1} \hat{U}_y - 2x' \\ z'' &= \sigma^{-1} \hat{U}_z - z \ . \end{aligned}$$

Hence, $\hat{U}$ is the new form of the potential equivalent to that in the circular case. We only need to apply one last scaling of the coordinates to make the equations

independent from μ. We multiply all lengths by the factor $\mu^{1/3}$ like we did in Section 4.2, then we redefine once more the potential as $U = \hat{U}\mu^{-2/3}$, i.e.

$$U = \frac{3}{2}x^2 + \frac{1}{r} + \beta x \ ,$$

where it is easy to verify that $\beta = a_{\mathrm{srp}}R^2/\mu^{1/3}$. The final equations of motion are unaffected by this transformation,

$$x'' = \sigma^{-1}U_x + 2y' \tag{4.21a}$$
$$y'' = \sigma^{-1}U_y - 2x' \tag{4.21b}$$
$$z'' = \sigma^{-1}U_z - z \ . \tag{4.21c}$$

The form is thus very similar to that of the circular Hill's problem, and it is interesting to note that the only term dependent on ν is the σ^{-1} factor with the derivative of U.

4.4.2 Jacobi Constant Equivalent and Zero-Velocity Surfaces

The introduction of an eccentricity greater than zero in the asteroid orbit makes Hill's problem a non-conservative system. No integral of motion like the Jacobi constant exists any more, and the conditions for the existence of periodic orbits become much more restrictive. Nevertheless it is sometimes useful to compute a non-constant quantity equivalent to C to study the motion on an instant-by-instant basis. It is found with the same procedure used in the previous cases, multiplying each equation of (4.21) by the first derivative of the corresponding variable and summing them all. Approximating the ν–dependent term σ as constant at any given time, this results in the expression

$$C_e(\nu) = \dot{x}^2 + \dot{y}^2 + \dot{z}^2 + z^2 - \sigma^{-1}U \ .$$

The quantity $C_e(\nu)$ oscillates with σ as ν progresses. At a fixed point in time, some of the properties of motion are equivalent to those of the circular Hill's problem with $C = C_e$. The zero-velocity surfaces are thus defined but constantly pulsating between the states corresponding to the minimum and maximum of σ.

Chapter 5

Grid Search for Periodic Orbits

When dealing with dynamical systems it is desirable to have a complete knowledge of the types and behaviors of their periodic solutions. Our knowledge is deepest for the most studied problems, such as the restricted 3-body problem, for which reviews of tens of families of periodic orbits abound [13, 15, 16, 66, 5, 48, 10, 52].

One method often used to obtain many periodic orbits is to apply numerical continuation starting from a known solution. This initial solution usually is an equilibrium point or an orbit in a limit case for one of the parameters, i.e. in a simpler or better known system. By slowly changing the parameters and following along a solution branch we can come across bifurcation points, which lead to new families with different structures. In this way a tree of several distinct orbit families are found, and the relations between them are clearly known. This method was followed, for instance, by Hénon and Doedel in the works cited above.

This work, however, applies continuation as a second step, after an initial grid search. Because the objective is to find orbits that are feasible in an exploration mission, it is important to obtain a large and varied set of solutions. We can then compare these and select those that are most appropriate for the purposes of the mission. Therefore, instead of starting from a single solution and continuing it as far and wide as possible, we perform a grid search for many solutions at the same time. Only then we use numerical continuation to study the properties and relations between them. A grid search method of this type has been used in several occasions [13, 28, 52].

This approach, in a sense, is a backwards version of the previous one, because it often finds a convergence of many families into a single one. From this point of view it might seem as an inefficient way to do the same thing. However it has the advantage of allowing for the discovery of independent family trees that are completely disconnected from each other, or which would be hard to reach through continuation.

The main disadvantage of a grid search is its high computational cost in searching though a great number of trajectories. Here we mitigate the problem by restricting the search space to the states and parameters most pertinent to Hayabusa 2's case, and by focusing on the continuation of only the most appropriate orbits.

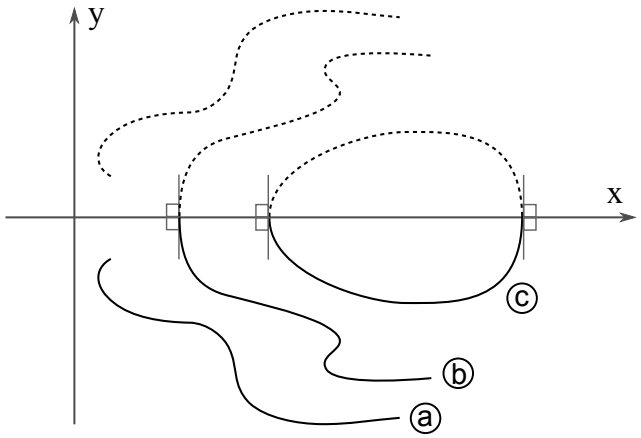

Figure 5.1. Symmetry with respect to the x–z plane. (a) Generic trajectory; (b) trajectory where $(y, v_x, v_z) = 0$ at one end; (c) periodic orbit, where the discontinuities vanish at both ends.

5.1 Symmetries and Periodic Orbits

The grid search for orbits is greatly aided by the symmetries that exist in the system in Eq. (4.8). A theorem of Miele [39], called *Theorem of Image Trajectories* states that the dynamics of the restricted 3-body problem is invariant under three types of symmetries:

$$(y, t) \rightarrow (-y, -t) \tag{5.1a}$$
$$(y, z, t) \rightarrow (-y, -z, -t) \tag{5.1b}$$
$$(z) \rightarrow (-z) \ . \tag{5.1c}$$

The theorem is still valid in the case of Hill's problem and even in the augmented Hill's problem.

These symmetries mean that for any trajectory that we obtain, there exist three more trajectories that are identical except for the reflections listed above. Symmetry (5.1c) gives trajectories with the same direction in time as the original one. The other two, on the other hand, require a time reversal, and can be exploited to find periodic orbits. It is straightforward to verify that symmetries (5.1a) and (5.1b) in position correspond to the following transformations of the velocity vector, respectively:

$$(v_x, v_z) \rightarrow (-v_x, -v_z)$$
$$(v_x) \rightarrow (-v_x) \ .$$

If we take two generic trajectories of finite duration, where each is the reflection of the other through one of the two above symmetries, in general there will be a discontinuity between the final point of one and the initial point of the other. This discontinuity is due to the change in sign, introduced by the transformation, of some components of position and velocity. The simplest situation in which the discontinuity disappears is when all the components that are reflected vanish at a point (Figure 5.1). If this occurs both at the beginning and at the end of both trajectories, then together they form a closed and continuous trajectory, or periodic

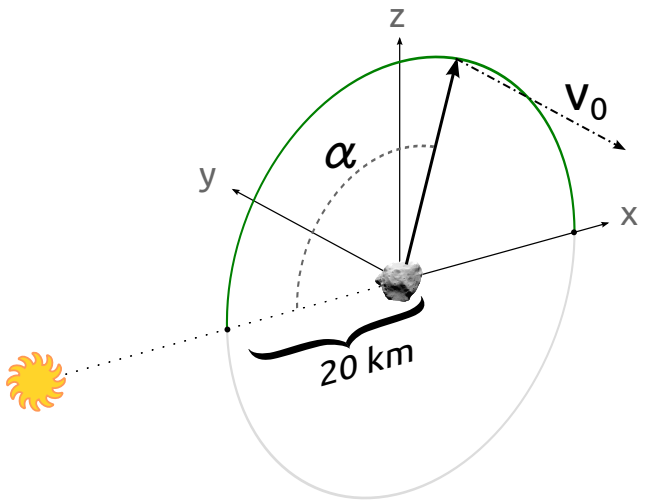

Figure 5.2. The search space is reduced to a circle of radius 20 km on the x–z plane, parametrized by the angle α, and to the magnitude of the initial velocity out of this plane.

orbit. Therefore, the sufficient conditions for a periodic orbit deriving from the two time-inverting symmetries are, respectively,

$$(y, v_x, v_z) = 0 \tag{5.2a}$$

or

$$(y, z, v_x) = 0 \tag{5.2b}$$

at two times t_1 and t_2 with $t_1 \neq t_2$.

Periodic orbits that satisfy condition (5.2a) are specularly symmetric with respect to the vertical plane passing through both primaries, or x–z plane. Those that satisfy (5.2b), on the other hand, are axi-symmetric with respect to the x axis or, equivalently, anti-symmetric with respect to the x–z plane.

5.2 Selection of an Appropriate Grid

The properties of symmetry detailed aid in the design of the grid search. Condition (5.2a) requires that the x–z plane is crossed twice with the x and z component of the velocity equal to zero. For condition (5.2b) to be satisfied there must be two crossings of the x axis with $v_x = 0$. The grid search thus consists in taking a range of initial states that satisfy one of these conditions, propagating them in time and looking for those that come to satisfy the condition again at a later time.

A grid search of this kind is conceptually simple and can be implemented quickly, but the precise propagation of thousands of trajectories is a very slow endeavor for machines equipped with commercially-available processors. Trying to sample densely a wide 3-dimensional space, once for every value of the parameters, would make the operation time prohibitively long on a normal computer. As a consequence of this, we must adopt some measures to restrict the search space to a size explorable in reasonable times, while trying not to reduce too much the number of solutions.

We accomplish this by using the mission requirements that are available to us for Hayabusa 2.

Although both periodicity conditions (5.2a) and (5.2b) are equally valid in theory, one of the requirements for Hayabusa 2 is that it must never enter the asteroid's shadow. Most of the solutions that we would find with condition (5.2b) cross the x axis at least once on the positive side, where the asteroid's shadow is present. Therefore in our search algorithm we use only condition (5.2a), giving up a part of the possible solutions in exchange for a greatly reduced computational burden. Moreover, instead of sampling the x–z plane in two dimensions, we fix the initial distance from the asteroid to 20 km and parametrize the initial state with the angle α inside the circle, see Figure 5.2. Because of symmetry (5.1c), it is sufficient to sample the interval $0 < \alpha < \pi$, where 0 corresponds to the direction of the sun. We also vary the magnitude v_0 of the initial velocity, which is always normal to the plane due to condition (5.2a). Hence the grid search is carried out in the 2-dimensional subspace (α, v_0).

The reduction of the search space substantially restricts the number of discoverable solutions. Nevertheless, 20 km is the distance used by Hayabusa 2 for its hovering stance and, coincidentally, it is also close to the distance of the system's L_2 equilibrium point. It represents a good guess for the scale of the orbits that would have to be used. The search is repeated for different values of the SRP parameter β, providing the possibility to catch some of those orbits that passed undetected in a single run. Furthermore, we apply numerical continuation to some orbits in the next section, leading to a more general picture of the dynamics, independent from the 20 km scale imposed here.

After starting from its initial conditions, each trajectory may cross the x–z plane again several times, generally with different velocity directions and magnitudes. In this application, the program records up to the sixth crossing with the vertical plane with an adaptive map. For this reason, the complete map of each crossing is actually a mosaic of smaller maps, gradually added in order to order all meaningful ranges of the two parameters. When a complete map of a crossing is computed, it provides the v_x and v_z components of the velocity at that crossing. By showing the lines where each of these is zero independently, it becomes possible to identify those points where the two lines intersect, and consequently the trajectories that satisfy the sufficient conditions for periodicity. This procedure is detailed, with figures, in Chapter 10. In general, the accuracy of the intersection points between the $v_x = 0$ and the $v_z = 0$ lines is low, making it necessary to use differential correction to improve the periodic orbit's initial guesses. Differential correction is described in Chapter 6.

Chapter 6

Properties of Periodic Orbits and Tools for Their Analysis

This section presents some of the methods and tools used to study or to influence the dynamical properties of periodic orbits. They will be applied in the following sections for various tasks such as numerical continuation of the solutions and a study of their stability.

6.1 Variational Equations and Monodromy Matrix

Suppose we have a system of differential equations, such as the 6-dimensional equations of motion of Hill's problem defined in Eqs. (4.11). It is convenient to refer to the state at a given time t along a trajectory through the *flow map* $\varphi(t, \boldsymbol{x}_0)$. This form shows explicitly the dependence of the current state on the initial state $\boldsymbol{x}_0$. φ generally depends also on the initial time t_0, but in a time-independent system like the augmented Hill's problem it is safe to choose $t_0 = 0$. Obviously, $\varphi(0, \boldsymbol{x}_0) = \boldsymbol{x}_0$. The equations of motion along a trajectory starting at $\boldsymbol{x}_0$, thus, are

$$\frac{\partial \varphi}{\partial t} = f\left(\varphi(t, \boldsymbol{x}_0)\right) \quad . \tag{6.1}$$

We now introduce a small deviation in the initial conditions, in the form of the error vector $\delta\boldsymbol{x}_0 = \delta\boldsymbol{x}(0)$. Too see how the whole trajectory is affected by this change, we write the expression of the error at time t:

$$\delta\boldsymbol{x}(t) = \varphi(t, \boldsymbol{x}_0 + \delta\boldsymbol{x}_0) - \varphi(t, \boldsymbol{x}_0) \quad . \tag{6.2}$$

We then expand the first term on the right of (6.2) in Taylor series around $\delta\boldsymbol{x}_0 = 0$,

$$\varphi(t, \boldsymbol{x}_0 + \delta\boldsymbol{x}_0) = \varphi(t, \boldsymbol{x}_0) + \frac{\partial \varphi}{\partial \boldsymbol{x}_0}(t, \boldsymbol{x}_0)\delta\boldsymbol{x}_0 + \mathcal{O}\left(\delta\boldsymbol{x}_0^2\right) \quad ,$$

where $\mathcal{O}\left(\delta\boldsymbol{x}_0^2\right)$ represents terms of higher order. If $\delta\boldsymbol{x}_0$ is small enough, we can truncate the series at the first order and thus approximate (6.2) as

$$\delta\boldsymbol{x}(t) = \frac{\partial \varphi}{\partial \boldsymbol{x}_0}(t, \boldsymbol{x}_0)\delta\boldsymbol{x}_0 \quad . \tag{6.3}$$

The term $\partial\varphi/\partial\boldsymbol{x}_0$ in (6.3) is sometimes called *state transition matrix*, and encodes the sensibility of the state on the initial condition. The state transition matrix, here abbreviated as $\Phi(t, \boldsymbol{x}_0)$, is the solution of the *variational equations*

$$\dot{A} = JA \ , \tag{6.4}$$

where $J = \partial f/\partial\boldsymbol{x}$ is the *Jacobian matrix* of f. For the restricted 3-body problem, as well as Hill's problem, the Jacobian matrix has the following form:

$$J = \begin{bmatrix} 0 & 0 & 0 & 1 & 0 & 0 \\ 0 & 0 & 0 & 0 & 1 & 0 \\ 0 & 0 & 0 & 0 & 0 & 1 \\ U_{xx} & U_{xy} & U_{xz} & 0 & 2 & 0 \\ U_{xy} & U_{yy} & U_{yz} & -2 & 0 & 0 \\ U_{xz} & U_{yz} & U_{zz} & 0 & 0 & 0 \end{bmatrix} \ , \tag{6.5}$$

where the double subscripts represent second partial derivatives.

The fact that Φ solves (6.4) is easily demonstrated by differentiating (6.1) with respect to the initial state,

$$\frac{\partial}{\partial\boldsymbol{x}_0}\left(\frac{\partial\varphi}{\partial t}\right) = \frac{\partial f}{\partial\boldsymbol{x}_0} = \frac{\partial f}{\partial\boldsymbol{x}}\frac{\partial\varphi}{\partial\boldsymbol{x}_0} \ ,$$

where we can switch the order of the partial derivatives on the left side by virtue of Schwarz' theorem, leading to

$$\dot{\Phi} = J\Phi \ . \tag{6.6}$$

Thus the value of $\Phi(t, \boldsymbol{x}_0)$ is obtained by numerically propagating each of the N^2 members of (6.6) using $\Phi(0, \boldsymbol{x}_0) = I$ as initial condition.

In the case of a periodic orbit of period T, the value of Φ when $t = T$ is of particular importance, because it contains all the information about the orbit's linear stability. In this case it is called *monodromy matrix* and is defined as

$$M = \Phi(T, \boldsymbol{x}_0) \ .$$

Differentiating Eq. (6.1) with respect to t reveals that also $d\varphi/dt$ is a solution of the homogeneous variational equation (6.4). From this it follows that we can express the time evolution of f along the trajectories as

$$f(\varphi(t, \boldsymbol{x}_0)) = \Phi(t)\, f(\varphi(0, \boldsymbol{x}_0)) \tag{6.7}$$

and that

$$M\, f(\varphi(0, \boldsymbol{x}_0)) = f(\varphi(T, \boldsymbol{x}_0)) = f(\varphi(0, \boldsymbol{x}_0)) \ . \tag{6.8}$$

This is equivalent to saying that f belongs to the null space of $M - I$, and that 1 is always an eigenvalue of M. In the dynamical systems employed in this work, this unitary eigenvalue always has multiplicity 2.

Entities analogous to the state transition and monodromy matrices can also be defined for errors in the system's parameters. For example, given an error $\delta\beta$ for the solar radiation pressure constant in (4.11), the following identity is valid:

$$\delta\boldsymbol{x}(t) = \frac{\partial\varphi}{\partial\beta}(t, \boldsymbol{x}_0)\delta\beta \ ;$$

$\partial\varphi/\partial\beta$ is the solution of the system

$$\frac{\partial}{\partial t}\left(\frac{\partial\varphi}{\partial\beta}\right) = J\frac{\partial\varphi}{\partial\beta} + \frac{df}{d\beta} \ ,$$

with $\partial\varphi(0, \boldsymbol{x}_0)/\partial\beta = \mathbf{0}$.

6.2 Differential Correction of Grid Search Solutions

In some cases we are provided with approximate trajectories that are not suitable for detailed analysis. In particular, this is true for the periodic solutions found in our grid search phase. Because the grid is inevitably a coarse approximation of a continuous space, the points of intersection satisfying $v_x = 0$ and $v_z = 0$ lead to trajectories *close* to periodic orbits, but not quite periodic themselves. We then have to improve these guesses taking them to much higher levels of precision. One straightforward way to do this is through *differential correction*.

The linear relation in (6.3) tells us how to control the terminal value of any trajectory by slightly altering the initial state. For a periodic orbit of period T, this relation gives

$$\delta\boldsymbol{x}(T) = M\delta\boldsymbol{x}_0 \ . \tag{6.9}$$

Our goal is to obtain a trajectory, close to the approximate one, where the initial and final state coincide to within a chosen high precision. If the approximate solution has a final state $\boldsymbol{x}(T) \neq \boldsymbol{x}_0$, then the above statements translate into the following condition to be satisfied:

$$\boldsymbol{x}(T) + \delta\boldsymbol{x}(T) = \boldsymbol{x}_0 + \delta\boldsymbol{x}_0 \ . \tag{6.10}$$

Substitute (6.9) into (6.10) to obtain

$$\delta\boldsymbol{x}_0 = (M - I)^{-1}\left(\boldsymbol{x}_0 - \boldsymbol{x}(T)\right) \ .$$

If the starting approximation is good enough, applying this $\delta\boldsymbol{x}_0$ yields a new trajectory where the error $\boldsymbol{x}_0 - \boldsymbol{x}(T)$ is smaller than before. Repeating the procedure a few more times eventually leads to convergence. This procedure is easily recognized to be a formulation of Newton's method.

The period of the final precise orbit found with this procedure is still T. More sophisticated differential correction equations can be developed to satisfy some other conditions, such as a return exactly on the x–z plane, but with a different period. However it is not necessary to enforce such stricter requirements for our simple application.

6.3 Floquet Multipliers and Stability Indices

The stability information of a periodic orbit is encoded in the eigenstructure of its monodromy matrix M. In the system described by Eqs. (4.11) the 6 eigenvalues are divided into three pairs of reciprocal eigenvalues:

$$\left[\lambda_1, \quad \frac{1}{\lambda_1}, \quad \lambda_2, \quad \frac{1}{\lambda_2}, \quad \lambda_3, \quad \frac{1}{\lambda_3}\right] \ ;$$

furthermore, two of them are always unitary, i.e. $\lambda_3 = 1$. The stability or instability of the orbit, then, depends on the values of λ_1 and λ_2, called *Floquet multipliers*. When $|\lambda_i| = 1$ for both multipliers, any initial perturbation is not amplified along the trajectory, and the orbit is linearly stable. If, on the other hand, any of the two has a non-unitary absolute value, the orbit is unstable.

Stability and other information about a family are more easily visualized with the introduction of four new indices related to λ_1 and λ_2 [3, 6]. The eigenvalues of M are the roots of the characteristic polynomial, and thus it is possible to write

$$\begin{aligned}
(\lambda-1)^2\left[(\lambda-\lambda_1)\left(\lambda-\frac{1}{\lambda_1}\right)(\lambda-\lambda_2)\left(\lambda-\frac{1}{\lambda_2}\right)\right] &= 0 \\
\Rightarrow (\lambda-1)^2\left[\left(\lambda^4+a_1\lambda^3+a_2\lambda^2+a_1\lambda+1\right)\right] &= 0 \\
\Rightarrow (\lambda-1)^2\left[\left(\lambda^2-k_1\lambda+1\right)\left(\lambda^2-k_2\lambda+1\right)\right] &= 0 \ .
\end{aligned}$$

It follows that the newly introduced a_1, a_2, k_1 and k_2 indices are

$$a_1 = -\left(\lambda_1+\frac{1}{\lambda_1}+\lambda_2+\frac{1}{\lambda_2}\right) \tag{6.11a}$$

$$a_2 = 2+\frac{\lambda_1}{\lambda_2}+\frac{\lambda_2}{\lambda_1}+\frac{1}{\lambda_1\lambda_2}+\lambda_1\lambda_2 \tag{6.11b}$$

$$k_1 = \lambda_1+\frac{1}{\lambda_1} \tag{6.11c}$$

$$k_2 = \lambda_2+\frac{1}{\lambda_2} \ . \tag{6.11d}$$

The above formulas are further simplified using the following relations, which do not require the computation of the eigenvalues [3]:

$$\begin{aligned}
a_1 &= 2-\mathrm{Tr}\,M \\
a_2 &= \frac{1}{2}\left(a_1^2+2-\mathrm{Tr}\,M^2\right) \\
k_{1,2} &= \frac{1}{2}\left(-a_1 \pm \sqrt{a_1^2-4a_2+8}\right) \ ,
\end{aligned}$$

where Tr is the trace operator on a matrix. The $a_{1,2}$ indices provide a visual representation of the different types of stability of an orbit. Figure 6.1 shows the a_1–a_2 plane, divided into seven regions. Only the region in the center contains stable orbits, whereas all the others have one or two eigenvalues in different types of unstable regimes.

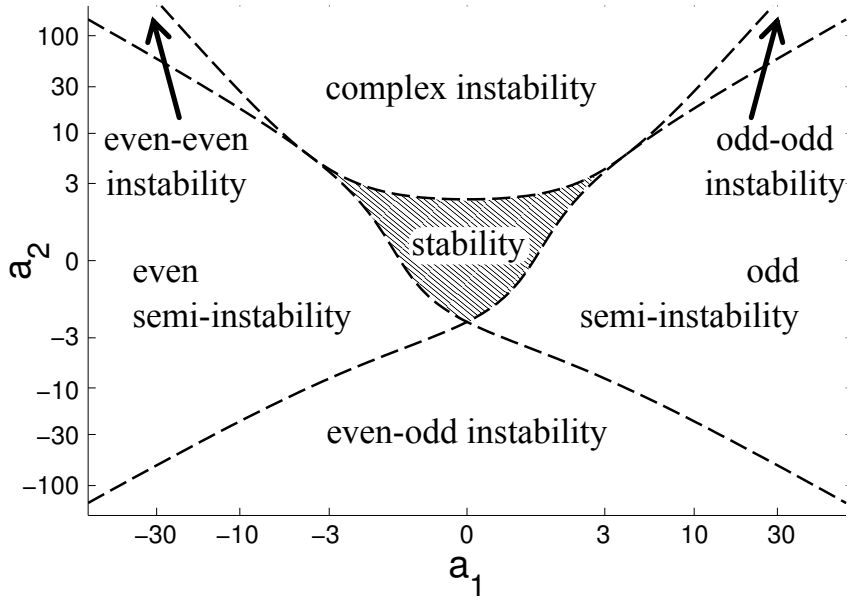

Figure 6.1. Stability regions with the $a_{1,2}$ indices defined by Broucke [6].

Indices $k_{1,2}$, on the other hand, provide easier access to information about family bifurcations. If $|k_i| > 2$ for either index, one eigenvalue has magnitude greater than one and the orbits are unstable. The case $k_i = -2$ corresponds to $\lambda_i = -1$ or, in polar coordinates, $\lambda_i = e^{\pi i}$. This means that a small displacement in the direction of the eigenvector of λ_i results in a equal and opposite displacement after one period of the orbit. After a second period, then, the orbit closes onto itself and is thus still periodic. Therefore the situation $k_i = -2$ often, but not always, gives birth to a new family of orbits with double period. Such points are called *period-doubling bifurcations*. Similar bifurcations arise also for higher multiples of the period. The values at which these occur is given by (6.11c) and (6.11d),

$$k_i = \exp\left(2\pi\frac{p}{q}i\right) + \exp\left(-2\pi\frac{p}{q}i\right) \ ,$$

where p is the number of periods of the original orbit and q that of the new orbit completed in the same time. For instance, a period-tripling bifurcation has $p = 1$, $q = 3$ and $k_i = -1$.

Another type of bifurcation, called fold bifurcation, occurs when the family reaches an extremal value of the continuation parameter and inverts the direction of continuation. A fold bifurcation generally leads to a change in stability, where $|k_i| = 2$ for one of the indices.

Chapter 7

Numerical Continuation

Whenever we have a solution to a parametrized non-linear set of equations, we may face the problem of obtaining new solutions for different values of the parameters. In this case, instead of starting the search from the beginning each time, we can use the already known solution as starting point, and an algorithm to extract neighboring solutions. Such algorithms are called *numerical continuation* methods.

Local continuation of solutions is based on the *implicit function theorem*. Let a smooth mapping $R : \mathbb{R}^m \to \mathbb{R}^n$

$$R(\boldsymbol{u}) = 0 \ , \tag{7.1}$$

have a solution in $\boldsymbol{u}_0 \in \mathbb{R}^m$. If the Jacobian matrix $\partial R/\partial \boldsymbol{u}$ i surjective in $\boldsymbol{u}_0$, i.e. it has full row rank m, then the implicit function theorem states that in the neighborhood of $\boldsymbol{u}_0$ there exists an $(m-n)$–dimensional submanifold of solutions. The task of a continuation algorithm is to move on this submanifold and obtain new solutions, discovering the *family* or *branch* to which the initial solution belonged.

7.1 Pseudo-Arclength Continuation

This work is focused on a case where $m - n = 1$, which leads to a one-dimensional curve of solutions. When this is true, there are several different methods to follow along the curve starting from $\boldsymbol{u}_0$.

The most straightforward method is to vary a single parameter, say, $s \in \boldsymbol{u}$, by a small amount, producing a first rough guess of where the new solution vector $\boldsymbol{u}_1$ might be in phase space:

$$s_1^{(0)} = s_0 + \Delta s \ , \tag{7.2}$$

keeping all the other elements of $\boldsymbol{u}_1$ equal to $\boldsymbol{u}_0$ (Figure 7.1a). Then a corrector method improves the guess iteratively keeping s constant. With Newton's method, one step is expressed as

$$\boldsymbol{u}_1^{(j+1)} = \boldsymbol{u}_1^{(j)} + \Delta \boldsymbol{u} \qquad \text{with} \qquad \frac{\partial R}{\partial \boldsymbol{u}} \left(\boldsymbol{u}_1^{(j)} \right) \Delta \boldsymbol{u} = -R \left(\boldsymbol{u}_1^{(j)} \right) \ .$$

This *natural parameter continuation* method is easily implemented and produces solutions equally spaced in s, but it is sub-optimal for most problems. When the

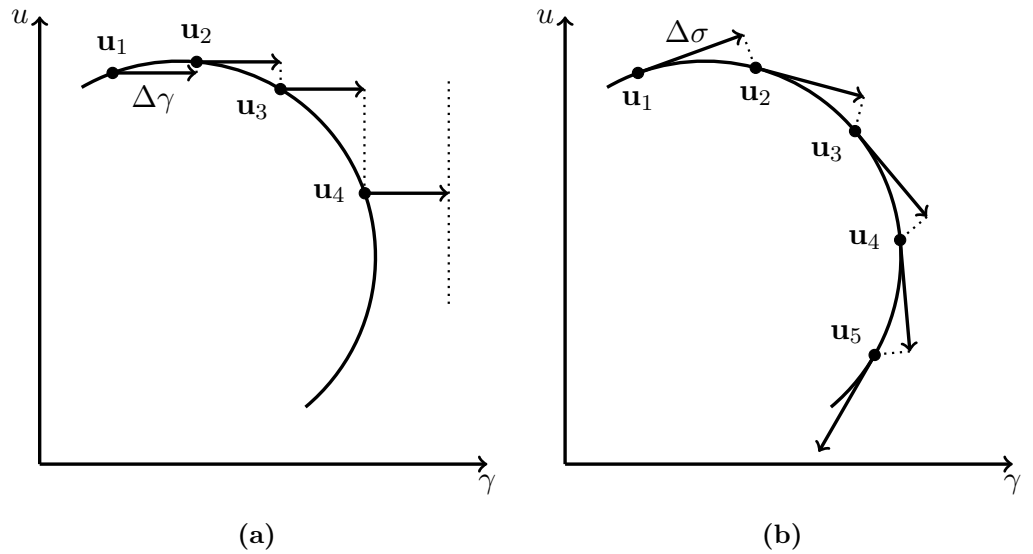

Figure 7.1. Two types of continuation. Arrows correspond to predictor steps, dotted lines to corrector sequences. (a) Natural parameter continuation. Only parameter s is changed at every step, but the algorithm halts at folding points. (b) Pseudo-arclength continuation. The algorithm can follow the path beyond folding points with tangent steps of length $\Delta\sigma$. Step lengths may be variable in both cases.

derivative $\partial R/\partial s$ is large, the initial guesses become poor, and make convergence difficult. Moreover, the solution curve could fold back so that no solution at all can be found by the corrector algorithm. This situation is shown in Figure 7.1a.

Although other alternative strategies have been devised, here we use the method called *pseudo-arclength continuation* because of its efficiency. It is based on the concept of arclength, the natural parametrization of a curve upon which all of the parameters and variables depend. Thus, instead of changing a single element of $\boldsymbol{u}$ independently, this method approximately follows along the arclength parameter σ. Arclength in itself is a theoretical tool. The algorithm is actually divided into a predictor phase and a corrector phase like natural parameter continuation, using first order approximations of the arclength to produce good initial guesses.

Starting from a solution $\boldsymbol{u}_i$, the predictor step moves in the direction $\partial\boldsymbol{u}/\partial\sigma$, tangent to the line of solution of (7.1). The condition to be satisfied in a step is

$$\Delta\sigma = (\boldsymbol{u}_{i+1} - \boldsymbol{u}_i)^* \cdot \frac{\partial \boldsymbol{u}}{\partial \sigma} \ , \tag{7.3}$$

where $\Delta\sigma$ is the step length chosen for the continuation and the * symbol represents the conjugate transpose operation. Hence the predictor step consists in a first guess $\boldsymbol{u}_{i+1}^{(0)} = (\partial\boldsymbol{u}_i/\partial\sigma)\,\Delta\sigma$, where $\partial\boldsymbol{u}_i/\partial\sigma$ is the unit null vector of the Jacobian $\partial R/\partial\boldsymbol{u}$ evaluated at $\boldsymbol{u}_i$. This is generally better than the guess given in (7.2) for natural continuation, because it adapts to the curve and is capable of following it beyond folds (Figure 7.1b).

Then the guess is improved iteratively using Newton's method with condi-

tion (7.3)

$$\begin{bmatrix} \left(\dfrac{\partial R}{\partial \boldsymbol{u}}\right)^{(n)} \\ \left(\dfrac{\partial \boldsymbol{u}_i}{\partial \sigma}\right)^{*} \end{bmatrix} \Delta \boldsymbol{u}^{(n)} = - \begin{bmatrix} R^{(n)} \\ (\boldsymbol{u}_{i+1} - \boldsymbol{u}_i)^{*} \cdot \dfrac{\partial \boldsymbol{u}_i}{\partial \sigma} - \Delta\sigma \end{bmatrix} , \tag{7.4}$$

solving for $\Delta \boldsymbol{u}^{(n)}$ and applying the change until a convergence condition is met.

7.2 Continuation of Periodic Orbits

Our purpose in using continuation is to find new periodic orbits in the augmented Hill's problem, therefore we proceed to express our specific problem in a form that can be used with the pseudo-arclength method. The equations of motion (4.11), in short form, are written as

$$\dot{\boldsymbol{x}} = f(\boldsymbol{x}, \beta) \ .$$

Let the period of a periodic orbit in this system be T. We make this duration into a parameter by mapping the independent variable to the interval $[0, 1]$, i.e. we introduce a new time variable $\tau = t/T$. The equation becomes

$$\boldsymbol{x}' = T f(\boldsymbol{x}, \beta) \ ,$$

where the prime ($'$) indicates differentiation with respect to τ. Note that after this transformation the condition for periodicity of a trajectory becomes

$$\boldsymbol{x}(1) = \boldsymbol{x}(0) \ . \tag{7.5}$$

For the rest of this discussion we will omit the dependence of f on β, which will remain constant throughout the continuation, and focus on varying the Jacobi constant C instead. C is an implicit parameter of the system, and cannot be varied directly like the others. We therefore introduce a perturbation and an associated *unfolding parameter* λ to regulate it,

$$\boldsymbol{x}' = g(\boldsymbol{x}, T, \lambda) = T f(\boldsymbol{x}, \beta) + \lambda \Lambda(\boldsymbol{x}) \ . \tag{7.6}$$

Here $\Lambda(\boldsymbol{x})$ is some appropriate function. Muñoz-Almaraz et al. [45] show that an appropriate choice is $\Lambda(\boldsymbol{x}) = \nabla C(\boldsymbol{x})$, but the simpler form $\Lambda(\boldsymbol{x}) = (0,\, 0,\, 0,\, v_x,\, v_y,\, v_z)$ also works well. The latter will be used in the following developments. When $\lambda \neq 0$ the perturbation makes the problem dissipative, and therefore prohibits the existence of periodic orbits. For this reason the pseudo-arclength algorithm looking for periodic orbits is forced to always respect the condition $\lambda = 0$, ensuring that the conservativity of the system is preserved while the state and the other

parameters change along the family. The full equations of motion, then, are

$$\begin{aligned} x' &= T v_x \\ y' &= T v_y \\ z' &= T v_z \\ v_x' &= T\,(2v_y + U_x) + \lambda v_x \\ v_y' &= T\,(-2v_x + U_y) + \lambda v_y \\ v_z' &= T U_z + \lambda v_z \ . \end{aligned}$$

We then frame the periodicity condition for a new orbit as a function Γ that depends on the 8 parameters of a periodic orbit. The first six parameters are the components of the initial state $\boldsymbol{x}_0$, and the remaining two are the period T and the unfolding parameter λ. For simplicity of formulation, we group all of these parameters into one vector $\boldsymbol{u} = (\boldsymbol{x}_0, T, \lambda)$. Let $\varphi_\tau = \varphi(\tau, \boldsymbol{x}_0)$ represent the flow of $g(\boldsymbol{u})$ at some time τ after starting from $\boldsymbol{x}_0$, and denote as $\boldsymbol{u}_i = (\boldsymbol{x}_{0,\,i},\, T_i,\, \lambda_i)$ a known i-th solution. Then, the condition for the periodicity of a new orbit close to $\boldsymbol{u}_i$ is

$$\Gamma(\boldsymbol{u}_{i+1}, \boldsymbol{u}_i) = \begin{bmatrix} \varphi(1, \boldsymbol{x}_{0,\,i+1}) - \boldsymbol{x}_{0,\,i+1} \\ \\ (\boldsymbol{x}_{0,\,i+1} - \boldsymbol{x}_{0,\,i})^* \cdot g_{0,\,i} \end{bmatrix} = \boldsymbol{0} \ , \tag{7.7}$$

where $g_{0,\,i}$ is the right-hand side of (7.6) evaluated at $\tau = 0$. The first six out of seven equations correspond to condition (7.5). The last element, on the other hand, ensures that the continuation effort moves in a direction that is orthogonal to the direction of motion $g_{0,\,i}$. Because any point along a periodic orbit satisfies (7.5), this additional orthogonality condition serves the purpose of reducing the search to a single direction and of avoiding an undesirable drift in the phase of the solution. In other words, by introducing this condition we have $\Gamma : \mathbb{R}^8 \to \mathbb{R}^7$, and according to the implicit function theorem the submanifold of solutions becomes a 1–dimensional line in $\mathbb{R}^8$.

Equation (7.7) has the form of (7.1), and we can apply the pseudo-arclength method to it to construct families of periodic orbits. As described in the previous subsection, the predictor step requires the computation of the Jacobian matrix of Γ. It is

$$\frac{\partial \Gamma}{\partial \boldsymbol{u}}(\boldsymbol{u}_{i+1}, \boldsymbol{u}_i) = \begin{bmatrix} \dfrac{\partial \varphi_1}{\partial \boldsymbol{x}_0} - I_{(6)} & \dfrac{\partial \varphi_1}{\partial T} & \dfrac{\partial \varphi_1}{\partial \lambda} \\ \\ g_{0,\,i}^* & 0 & 0 \end{bmatrix} \ , \tag{7.8}$$

in which $I_{(6)}$ is the 6×6 identity matrix. Obviously, the term $\partial \varphi_1 / \partial \boldsymbol{x}_0$ in (7.8) is the monodromy matrix M of $g(\boldsymbol{u})$. This, along with the other two elements of the

first row of (7.8) are obtained with variational equations (see Subsection 6.1), i.e.

$$\frac{d}{d\tau}\left(\frac{\partial\varphi_\tau}{\partial\boldsymbol{x}_0}\right) = TJ\,\frac{\partial\varphi_\tau}{\partial\boldsymbol{x}_0} \tag{7.9a}$$

$$\frac{d}{d\tau}\left(\frac{\partial\varphi_\tau}{\partial T}\right) = TJ\,\frac{\partial\varphi_\tau}{\partial T} + \frac{\partial g}{\partial T} \tag{7.9b}$$

$$\frac{d}{d\tau}\left(\frac{\partial\varphi_\tau}{\partial\lambda}\right) = TJ\,\frac{\partial\varphi_\tau}{\partial\lambda} + \frac{\partial g}{\partial\lambda}\ , \tag{7.9c}$$

where $J = \partial f/\partial\boldsymbol{x}$ is the Jacobian matrix of f. Eqs. (7.9) are to be integrated in the interval $\tau \in [0,1]$ for the solution $\tilde{\boldsymbol{u}} = (\boldsymbol{x}_0, T, 0)$ (i.e. with $\lambda = 0$) and initial conditions, respectively,

$$\frac{\partial\varphi_0}{\partial\boldsymbol{x}_0} = I_{(6)} \qquad\qquad \frac{\partial\varphi_0}{\partial T} = 0 \qquad\qquad \frac{\partial\varphi_0}{\partial\lambda} = 0\ .$$

The vector $\partial\varphi_1/\partial T$ can be reduced to a simple form by means of the method of variation of constants on the non-homogeneous Eq. (7.9b). Knowing that the solution of the homogeneous problem (7.9a) is the state transition matrix $\Phi(\tau) = \partial\varphi_\tau/\partial\boldsymbol{x}_0$, we can proceed as follows:

$$\begin{aligned}
\frac{\partial\varphi_\tau}{\partial T} &= \Phi(\tau)\int^{\tau}\Phi^{-1}(\tilde\tau)\frac{\partial g}{\partial T}(\varphi_{\tilde\tau})\,d\tilde\tau = \\
&= \Phi(\tau)\int^{\tau}\Phi^{-1}(\tilde\tau) f(\varphi_{\tilde\tau})\,d\tilde\tau = \\
&= \Phi(\tau)\int^{\tau} f(\varphi_0)\,d\tilde\tau = \\
&= \Phi(\tau)\, f(\varphi_0)\,\tau\ ,
\end{aligned}$$

where we have used (6.7). This leads to $\partial\varphi_1/\partial T = f(\varphi_0)$. We can apply the same method to (7.9c) to yield

$$\frac{\partial\varphi_1}{\partial\lambda} = M\int_0^1\Phi^{-1}(\tilde\tau)\frac{\partial g}{\partial\lambda}(\varphi_{\tilde\tau})\,d\tilde\tau\ .$$

Once the Jacobian of Γ is computed, we can obtain its null vector with numerical methods, and use it to produce the first guess $\boldsymbol{u}_{i+1}^{(0)} = (\partial\boldsymbol{u}_i/\partial\sigma)\Delta\sigma$. Then the repeated corrections through (7.4) generally lead to convergence. The step length condition in this application is

$$\Delta\sigma = (\boldsymbol{x}_{0,\,i+1} - \boldsymbol{x}_{0,\,i})^*\,\frac{\partial\boldsymbol{x}_0}{\partial\sigma} + (T_{i+1} - T_i)\,\frac{\partial T}{\partial\sigma} + (\lambda_{i+1} - \lambda_i)\,\frac{\partial\lambda}{\partial\sigma}\ . \tag{7.10}$$

Chapter 8

Linear-Quadratic Regulator

The discussion in this section derives the equations needed to enforce a given trajectory through active control. They will be used to stabilize periodic orbits in the augmented Hill's problem in the presence of perturbations in Chapter 11.

8.1 Linear State Feedback

Suppose we have a trajectory described by the flow $\varphi(t)$ and that we want our system to follow this motion in the presence of small perturbations in an efficient way. The equations of motion along the trajectory are

$$\dot{\boldsymbol{x}} = f\left(\varphi(t)\right) \quad , \tag{8.1}$$

whereas if we introduce a small deviation $\delta\boldsymbol{x}$ they can be expanded to the first order as follows:

$$\dot{\boldsymbol{x}} + \delta\dot{\boldsymbol{x}} = f\left(\varphi(t) + \delta\boldsymbol{x}\right) = f\left(\varphi(t)\right) + J\,\delta\boldsymbol{x} \quad , \tag{8.2}$$

where $J = \partial f/\partial\boldsymbol{x}$ is the Jacobian matrix (6.5), dependent on time. The purpose is to correct the deviation and return to the nominal trajectory, therefore we need to use some form of thrust. We enforce this by adding a term $B\boldsymbol{u}$ to Eq. (8.2). Then, by subtracting (8.1) to (8.2), we obtain a linear system in $\delta\boldsymbol{x}$,

$$\delta\dot{\boldsymbol{x}} = J\delta\boldsymbol{x} + B\boldsymbol{u} \quad , \tag{8.3}$$

with $\delta\boldsymbol{x} = \delta\boldsymbol{x}(t)$ and $\boldsymbol{u} = \boldsymbol{u}(t)$. The optimal control problem we have to solve is to find the control strategy that minimizes the cost functional

$$\mathcal{J} = \int_{t_0}^{t_1} \mathcal{L}\left(\delta\boldsymbol{x},\, \boldsymbol{u},\, t\right) dt + \mathcal{K}\left(\delta\boldsymbol{x}_1\right) \quad ,$$

with $\delta\boldsymbol{x}_1 = \delta\boldsymbol{x}(t_1)$. The Lagrangian $\mathcal{L}$ is

$$\mathcal{L}\left(\delta\boldsymbol{x},\, \boldsymbol{u},\, t\right) = \delta\boldsymbol{x}^T Q \delta\boldsymbol{x} + \boldsymbol{u}^T R \boldsymbol{u} \quad ,$$

where Q in general is a symmetric positive semi-definite matrix and R is a symmetric positive definite matrix. This definition of $\mathcal{L}$ ensures that both the deviation and

the control are minimized according to the weights Q and R. The terminal cost $\mathcal{K}$ depends on the final deviation as

$$\mathcal{K}\left(\delta\boldsymbol{x}_1\right) = \delta\boldsymbol{x}_1^T S \delta\boldsymbol{x}_1 \ ,$$

where S is a symmetric positive semi-definite matrix. This is called the *linear quadratic regulator* (LQR) problem.

The *linear state feedback law* in the theory of LQR states that the optimal control $\boldsymbol{u}^*$ depends linearly on the state ($\delta\boldsymbol{x}$ in this case) with the following relation [2]:

$$\boldsymbol{u}^*(t) = -R^{-1}B^T P \delta\boldsymbol{x}^* \ , \tag{8.4}$$

and that the matrix P is a solution of the Riccati differential equation

$$\dot{P} = -PJ - J^T P - Q + PBR^{-1}B^T P \ , \tag{8.5}$$

subject to the terminal condition $P(t_1) = S$. Note that from the properties of B, R, Q and S follows that P is a symmetric positive semi-definite matrix.

The Riccati Eq. (8.5) can be solved directly using numerical methods with backwards integration from t_1 to t_0. However we can simplify it slightly by using application-specific assumptions on the various matrices at play. For instance, we can divide the Jacobian J from (6.5) into its minors,

$$J = \begin{bmatrix} 0_{(3)} & I_{(3)} \\ U_2 & D \end{bmatrix} \quad \text{with} \quad U_2 = \begin{bmatrix} U_{xx} & U_{xy} & U_{xz} \\ U_{xy} & U_{yy} & U_{yz} \\ U_{xz} & U_{yz} & U_{zz} \end{bmatrix} \quad D = \begin{bmatrix} 0 & 2 & 0 \\ -2 & 0 & 0 \\ 0 & 0 & 0 \end{bmatrix} \ .$$

The minors $0_{(3)}$ and $I_{(3)}$ are, respectively, the 3×3 null matrix and the 3×3 identity matrix. Furthermore, for the stabilization of the trajectories we can assume a generic thrust acceleration vector divided in three Cartesian components,

$$B = \begin{bmatrix} 0_{(3)} \\ I_{(3)} \end{bmatrix} \ ,$$

while we give the weights the following structure:

$$Q = \begin{bmatrix} q_1 I_{(3)} & 0_{(3)} \\ 0_{(3)} & q_2 I_{(3)} \end{bmatrix} \qquad R = k\, I_{(3)} \qquad S = 0_{(6)} \ ,$$

where q_1 and q_2 are positive real integers. The choice of S is motivated by the fact that the trajectories to stabilize are periodic, and the control will be performed over a single period. There is no need to force the system to return to nominal after exactly one period, and the running cost is the important factor to be minimized.

After decomposing also the matrix P into equal minors P_I, P_{II}, P_{III} and P_{IV}, we can now re-express (8.5) as

$$\dot{P}_I = -U_2\, P_{II}^T - P_{II}\, U_2 + k^{-1} P_{II}\, P_{II}^T - q_1 I_{(3)} \tag{8.6a}$$

$$\dot{P}_{II} = -U_2\, P_{IV} - P_I - P_{II}\, D + k^{-1} P_{II}\, P_{IV} \tag{8.6b}$$

$$\dot{P}_{IV} = -P_{II} + D\, P_{IV} - P_{II}^T - P_{IV}\, D + k^{-1} P_{IV}^2 - q_2 I_{(3)} \ , \tag{8.6c}$$

$$P(t_1) = 0_{(6)} \tag{8.6d}$$

noting that $P_{III} = P_{II}$, $P_I = P_I^T$ and $P_{IV} = P_{IV}^T$. In this way, the solution of the optimization problem (8.3) is reduced to the solution of the system of differential equations (8.6).

8.2 Integral Feedback

In some cases the control produced by the basic LQR is able to stabilize the motion, but cannot eliminate completely the displacement from the nominal trajectory. This might happen, for instance, when the perturbation is slowly varying or constant, as is the first case treated in Chapter 11. To cope with this limitation, we can introduce an additional term in Eq. (8.4) based on the integral of $(\delta x, \delta y, \delta z)$. The integral is computed along the equations of motion as three additional components $\boldsymbol{\mathcal{I}} = (\mathcal{I}_{(x)}, \mathcal{I}_{(y)}, \mathcal{I}_{(z)})$ defined as

$$\begin{aligned} \dot{\mathcal{I}}_{(x)} &= \delta x \\ \dot{\mathcal{I}}_{(y)} &= \delta y \\ \dot{\mathcal{I}}_{(z)} &= \delta z \ . \end{aligned}$$

The control is then expanded with an additional term,

$$\boldsymbol{u} \to \tilde{\boldsymbol{u}} = \boldsymbol{u} - K_{int}\, \boldsymbol{\mathcal{I}} \ , \tag{8.7}$$

where K_{int} is an appropriate weight matrix. In the present application, $K_{int} = k_{int} I_{(3)}$ and $k_{int} \in \mathbb{R}^+$. This term ensures that any steady-state displacement is reduced to zero.

8.3 Asteroid Orbit Ellipticity as a Perturbation

Because the periodic orbits found with the methods in the preceding chapters are all pertinent to the circular Hill's problem, they are not directly applicable to the more realistic elliptic problem, whose equations were defined in Section 4.4. It might, however, be possible to force the trajectories to follow periodic paths in the elliptic (pulsating) reference frame. The LQR is perhaps the simplest way to do this, when the difference between the elliptic and the circular problems is formulated as a perturbation. In general, the LQR does not need to know the nature of the perturbation it is attempting to hinder. However, when the perturbation is understood beforehand, like in the case of the elliptic problem, we can add one more term to (8.4) to counter it programmatically, at least up to its first order.

Suppose the equations of motion of the circular case are $\dot{\boldsymbol{x}} = f_c(\boldsymbol{x})$ and those of the elliptic case are $\dot{\boldsymbol{x}}_e = f_e(\boldsymbol{x}_e, e)$, where e is the eccentricity of the asteroid's orbit and $\boldsymbol{x}_e$ is the state in the elliptic problem's frame. From (4.11) and (4.21), it is clear that $f_e(\boldsymbol{x}_e, 0) = f_c(\boldsymbol{x})$. We can expand the elliptic problem equations to first order in e and in a small displacement $\delta\boldsymbol{x}$ as

$$\dot{\boldsymbol{x}}_e = f_e(\boldsymbol{x}_0 + \delta\boldsymbol{x}, e) \simeq f_c(\boldsymbol{x}_0) + \frac{\partial f_e}{\partial \boldsymbol{x}}(\boldsymbol{x}_0, 0)\, \delta\boldsymbol{x} + e\, \frac{\partial f_e}{\partial e}(\boldsymbol{x}_0, 0) \ .$$

Then the evolution of a displacement between the elliptic and the circular frame is governed by

$$\delta\dot{\boldsymbol{x}} = \dot{\boldsymbol{x}}_e - \dot{\boldsymbol{x}} \simeq \frac{\partial f_e}{\partial \boldsymbol{x}}(\boldsymbol{x}_0, 0)\, \delta\boldsymbol{x} + e\, \frac{\partial f_e}{\partial e}(\boldsymbol{x}_0, 0) = J\delta\boldsymbol{x} + e\, \left.\frac{\partial f_e}{\partial e}\right|_{e=0} \tag{8.8}$$

After including a control term $B\boldsymbol{u}$, system (8.8) becomes identical to system (8.3) except for the term in e. We can thus add an equal and opposite term to the control to directly cancel out its contribution to the dynamics in (8.3),

$$-e \left(\frac{\partial f_e}{\partial e} \right)_{e=0} \quad . \tag{8.9}$$

To compute $(\partial f_e/\partial e)_{e=0}$ for use in (8.9), we first need the derivative of $\sigma = 1 + e\cos\nu$:

$$\frac{\partial \sigma}{\partial e} = \frac{\partial \sigma}{\partial \nu}\frac{\partial \nu}{\partial e} + \frac{d\sigma}{de} = -e\,\sin\nu\,\frac{\partial \nu}{\partial e} + \cos\nu \quad ,$$

which, for $e \to 0$ reduces to $\cos\nu$ because $\partial\nu/\partial e$ is approximated by a series of integer powers of e and because $\lim_{e\to 0}\nu = t$. Then, from (4.21),

$$\frac{\partial f_e}{\partial e} = \frac{\partial f_e}{\partial \sigma}\frac{\partial \sigma}{\partial e} = \begin{bmatrix} 0 \\ 0 \\ 0 \\ -\sigma^{-2}U_x \\ -\sigma^{-2}U_y \\ -\sigma^{-2}U_z \end{bmatrix} \frac{\partial \sigma}{\partial e} \quad ,$$

and, for vanishing eccentricity,

$$\left(\frac{\partial f_e}{\partial e} \right)_{e=0} = -\cos t \begin{bmatrix} 0 \\ 0 \\ 0 \\ U_x \\ U_y \\ U_z \end{bmatrix} \quad .$$

Thus the control is augmented,

$$\boldsymbol{u} \to \hat{\boldsymbol{u}} = \boldsymbol{u} + e\cos t \begin{bmatrix} U_x \\ U_y \\ U_z \end{bmatrix}$$

This addition facilitates the work of the LQR making it, in general, more efficient.

Chapter 9

Gravity Irregularities

In all the previous developments, we have considered the potential of a point mass or, equivalently, of a perfectly spherical body with a uniform density distribution. In a real mission, this condition is never met, although it is an acceptable first approximation for planets and other roughly spherical bodies. For asteroids, the shape is seldom regular, and the density is often distributed unevenly as a result of their turbulent formation process. Thus the gravitational potential is more complex than that assumed in the ideal N-body problems described in Chapter 4. To simulate these irregular gravity fields, in this work we decompose it into spherical harmonic terms, which make an analytical, albeit approximated, expression of the potential possible.

9.1 Harmonic Expansion of the Potential

In a reference frame fixed with respect to the asteroid and centered in its center of mass, we can express the position of any point (x, y, z) in spherical coordinates as

$$\begin{aligned} x &= r\cos\theta\cos\varphi \\ y &= r\cos\theta\sin\varphi \\ z &= r\sin\theta \ , \end{aligned}$$

where r is the distance from the origin, θ is the latitude and φ is the longitude of the point. Our purpose is to decompose the potential into three independent components,

$$V = R(r)\,\Theta(\theta)\,\Phi(\varphi) \ . \tag{9.1}$$

Considerations on the properties of V, which must solve Laplace's equation, show that the radial term must have the form [25]

$$R(r) = Gm_2\frac{r_0^n}{r^{n+1}} \ , \tag{9.2}$$

for some positive integer n, with r_0 the maximum radius of the irregular asteroid. In a similar way, the longitudinal term must be

$$\Phi(\varphi) = C\cos m\varphi + S\sin m\varphi \ , \tag{9.3}$$

where C and S are two real constants and m is some positive integer. The term Θ, on the other hand, is best expressed with *associated Legendre polynomials* $P_{nm}(\sin\theta)$, where

$$P_{nm}(u) = \left(1-u^2\right)^{\frac{m}{2}} \frac{d^m}{du^m} P_n(u) \ ,$$

with $m \leqslant n$ and where $P_n(u)$ is the Legendre polynomial [41]

$$P_n(u) = \frac{1}{2^n n!} \frac{d^n}{du^n} \left(u^2-1\right)^n \ .$$

The potential (9.1) can then be rewritten as

$$V = \frac{Gm_2}{r} \sum_{n=0}^{\infty} \sum_{m=0}^{n} \left(\frac{r_0}{r}\right)^n P_{nm}(\sin\theta) \left(C_{nm}\cos m\varphi + S_{nm}\sin m\varphi\right) \ . \tag{9.4}$$

The number n is the *degree* of the spherical harmonics, while m determines its *order*. This series is convergent for $r > r_0$, but there is no guarantee of convergence when $r < r_0$.

All the information about the potential is carried by the spherical harmonic coefficients C_{nm} and S_{nm}. When the asteroid is a point mass, all the coefficients vanish except for that of the 0th degree and order, which is always $C_{00} = 1$. Moreover $P_{00} = 1$, so that the potential takes the traditional form Gm_2/r. The terms of the summation in (9.4) with $m = 0$ are called *zonal terms* and describe the part of potential that only depends on the latitude. By definition, S_{n0} for all n. When $0 < m < n$, the terms are called *tesseral*, and depend on both angles. Finally, when $m = n$ the terms are called *sectoral*.

The coefficients C_{nm} and S_{nm} tend to vary by many orders of magnitude based on degree and order, making comparisons inconvenient. In this work we use a common normalization defined as

$$\bar{C}_{nm} = KC_{nm} \qquad \text{and} \qquad \bar{S}_{nm} = KS_{nm} \ ,$$

with

$$K = \left[\frac{(n+m)!}{(2-\delta_{0m})(2n+1)(n-m)!}\right]^{\frac{1}{2}} \ ,$$

where δ_{0m} is the Kronecker delta, equal to 1 when $m = 0$ and 0 otherwise. According to the scaling of the coefficients, also the Legendre polynomials must be rescaled as $\bar{P}_{nm} = K^{-1}P_{nm}$. This makes the terms more manageable computationally.

9.1.1 Coefficients of a Tri-axial ellipsoid

As mentioned in the introductory sections, the exact shapes of most asteroids are not known, and it is impossible to know the spherical harmonic coefficients without a rendezvous mission with that specific purpose. Nevertheless we often have basic data about the shape from optical or radar remote observations. One way to use this data to estimate the coefficients is to approximate the body with a homogeneous tri-axial ellipsoid characterized by three semi-axis lengths a, b and c.

If $a > b > c$, then the maximum radius of the asteroid is $r_0 = a$ and its symmetries result in the following properties [51]

$$\begin{aligned} C_{nm} &= 0 \qquad \text{for } n \text{ or } m \text{ odd} \\ S_{nm} &= 0 \qquad \text{for all } n \text{ and } m. \end{aligned}$$

The following expressions give the remaining coefficients up to the fourth degree and order:

$$\begin{aligned} C_{20} &= \frac{2c^2 - \left(a^2 + b^2\right)}{10a^2} \\ C_{22} &= \frac{a^2 - b^2}{20a^2} \\ C_{40} &= 3\frac{3\left(a^4 + b^4\right) + 8c^4 + 2a^2b^2 - 8\left(a^2 + b^2\right)c^2}{140a^4} \\ C_{42} &= \frac{\left(a^2 - b^2\right)\left(2c^2 - a^2 - b^2\right)}{280a^4} \\ C_{44} &= \frac{\left(a^2 - b^2\right)^2}{2240a^4} \quad . \end{aligned}$$

9.2 Gravitational Acceleration

The gradient of the potential V gives the gravitational acceleration experienced by the orbiting body. Because the formulation above is in spherical coordinates, we need an expression that converts it back to Cartesian coordinates components. The chain rule gives us the form

$$\ddot{x} = \frac{\partial V}{\partial r}\frac{\partial r}{\partial x} + \frac{\partial V}{\partial \theta}\frac{\partial \theta}{\partial x} + \frac{\partial V}{\partial \varphi}\frac{\partial \varphi}{\partial x} \quad , \tag{9.5}$$

repeated identically for y and z. The differentials of the spherical and Cartesian coordinates are related by

$$\begin{bmatrix} dr \\ d\theta \\ d\varphi \end{bmatrix} = \Upsilon \begin{bmatrix} dx \\ dy \\ dz \end{bmatrix} \quad ,$$

with

$$\Upsilon = \begin{bmatrix} \cos\theta\cos\varphi & \cos\theta\sin\varphi & \sin\theta \\ -\dfrac{1}{r}\sin\theta\cos\varphi & -\dfrac{1}{r}\sin\theta\sin\varphi & \dfrac{1}{r}\cos\theta \\ -\dfrac{\sin\varphi}{r\cos\theta} & \dfrac{\cos\varphi}{r\cos\theta} & 0 \end{bmatrix} \quad .$$

With these relations the derivatives of r, θ and φ by x, y and z in (9.5) are easily executed. We are left with the task of computing the derivatives of V, which

corresponds to computing the derivatives of $R(r)$, $\Theta(\theta)$ and $\Phi(\varphi)$ by their respective variables. From (9.2) and (9.3) we see that the first two are

$$\begin{aligned}\frac{dR}{dr}(r) &= -Gm_2\frac{r_0^n\,(n+1)}{r^{n+2}}\\ \frac{d\Phi}{d\varphi}(\varphi) &= m\,(C_{nm}\sin m\varphi + S_{nm}\cos m\varphi)\quad .\end{aligned}$$

The derivative of an associated Legendre polynomial is given by the recursion

$$\frac{d\Theta}{d\theta}(\theta) = \frac{d}{d\theta}P_{nm}(\sin\theta) = -m\tan\theta\,P_{nm} + P_{n(m+1)}\quad ,$$

requiring the computation of an higher order Legendre polynomial $P_{n(m+1)}$. With these expressions we can now write the derivatives of the potential as

$$\begin{aligned}\frac{dV}{dr} &= \frac{dR}{dr}(r)\,\Theta(\theta)\,\Phi(\varphi)\\ \frac{dV}{d\theta} &= R(r)\,\frac{d\Theta}{d\theta}(\theta)\,\Phi(\varphi)\\ \frac{dV}{d\varphi} &= R(r)\,\Theta(\theta)\,\frac{d\Phi}{d\varphi}(\varphi)\quad .\end{aligned}$$

These, in turn, give the acceleration in Cartesian coordinates through the use of Υ. When working in Hill's problem, one more step is required to convert from the body-fixed reference frame to the standard frame in which the problem is formulated. This is done with simple trigonometrical methods such as through Euler angles or quaternions, but it has the complication of being twice time-dependent: the body-fixed frame rotates quickly around the asteroid's rotation axis, and the rotation axis precesses slowly as the asteroid moves along its orbit.

Part II

Results and Discussion

Chapter 10

Periodic Orbits in the Augmented Hill's Problem

In dynamical systems such as the 3-body problem and its variants, the motion is generally highly dependent on the initial conditions, and most trajectories degenerate into unpredictable chaos. This is why periodic motions are perhaps the most powerful tool with which we can challenge the problem. Periodic orbits are, in a sense, the "backbone" of the dynamics, and to know their behavior means to gain insight into the nature of the given system, and the potentialities hidden within it. This chapter applies the tools described in Chapters 4–7 to identify a variety of periodic orbits and their properties in the augmented Hill's problem. For the above reasons, this process is perhaps the fundamental result of this whole work.

10.1 Intersection Maps and Periodic Solutions

The grid search algorithm described in Section 5 was programmed to calculate up to the sixth crossing with the x-z plane. Therefore for each choice of β there are six maps from the (α, v_0) space to the space of transversal velocities (v_x, v_z). These maps are reported for $\beta = 33$ in Figure 10.1, where the lines corresponding to $v_x = 0$ and $v_z = 0$ are shown. Each intersection point between the two types of curves constitutes a point of a periodic orbit. The plots show v_0 in non-dimensional units.

A fraction of the orbits propagated during this phase escaped from the asteroid's gravity well at some point and never returned to the x-z plane again. These orbits are represented by gray areas in the plots in Figure 10.1. Moreover, not all the intersections appearing in the maps represent different orbits; in fact, after its first appearance at some n-th crossing, the intersection point of a periodic orbit is repeated at all the crossings numbers that are multiples of n. The white regions in the lower left of each map are untested because they are very unlikely to have any crossing. In fact, the grid search is adaptive, and the maps in Figure 10.1 are mosaics of many smaller meshes.

The plots are not symmetrical with respect to a change of sign of v_0, demonstrating the fact that direct and retrograde orbits are not specularly identical. Not always does an orbit exist in both directions, and when it does its properties such as period, size and stability are somewhat different in the two cases.

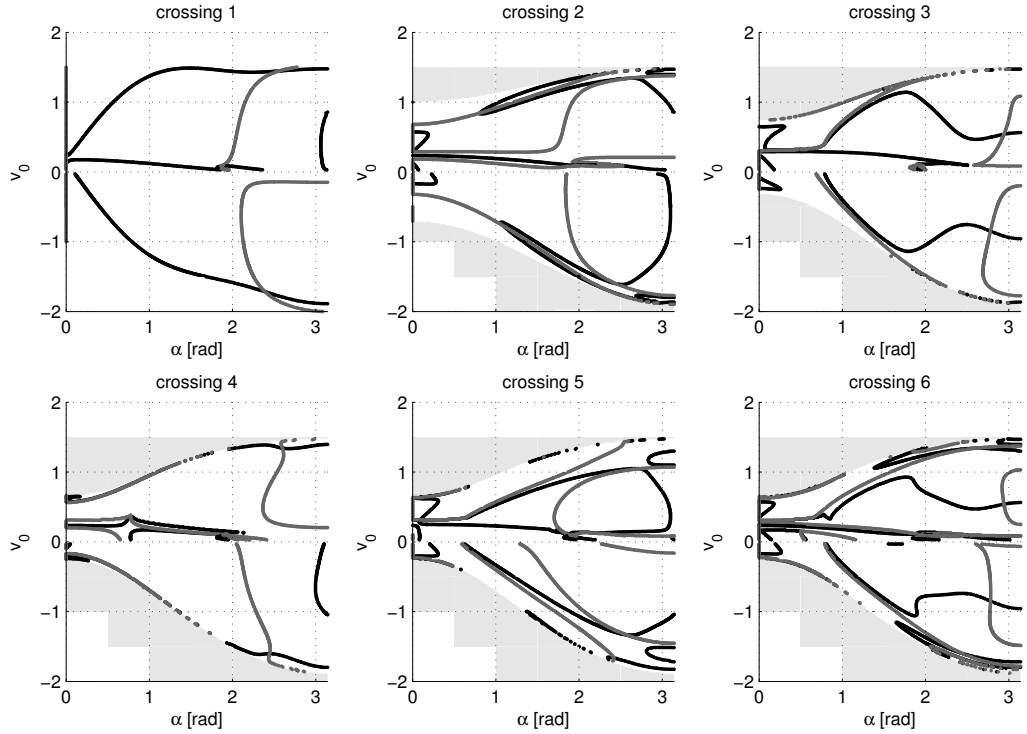

Figure 10.1. Maps resulting from the grid-search phase for $\beta = 33$. In order from left to right and top to bottom, they show the first through sixth crossing of the x-z plane. The black lines represent orbits with $v_x = 0$ at the crossing and the gray lines represent $v_z = 0$.

Note that in some areas of the maps close to the gray "escape regions" the structure of the lines becomes increasingly complex and higher and higher resolutions of the grid would be necessary to distinguish the lines. This makes it difficult to locate some periodic orbits. For the same reason for which these orbits are difficult to find, however, they also tend to be highly unstable. Therefore, for the purposes of the mission it is not effective to spend computational time to investigate them further.

The grid search process was repeated for $\beta = (27, 28, 29, 30, 31, 32, 33, 34, 35, 55)$. After accounting for duplicates appearing at different values of β, a total of 31 unique orbits were found. One example is displayed in Figure 10.2, while the complete catalog of solutions is included at the end of this section.

10.2 Periodic Orbit Families

Out of the 31 orbit types obtained in the previous step, we select 9 whose properties are most interesting for a real mission like Hayabusa 2. For each of these, we apply pseudo-arclength continuation to construct its full family branch. The family plot of the simplest orbit, A3311, is shown in Figure 10.3, and corresponds to the family of terminator orbits known from previous works [57, 4]. "Snapshots" of all the families are plotted in Section 10.4. Table 10.1 lists the orbits selected for continuation.

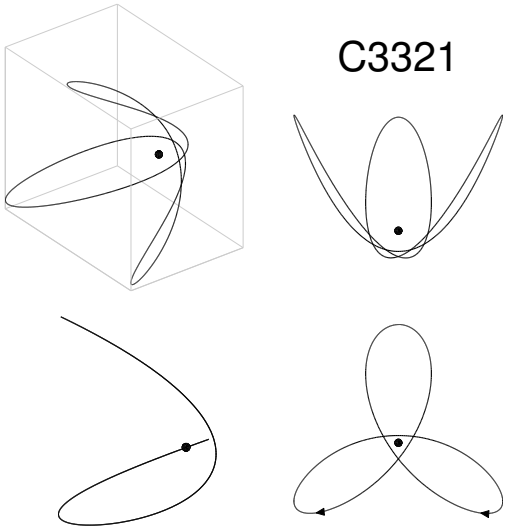

Figure 10.2. Periodic orbit C3321.

To each family we assign a code (Family ID). The last two columns of the table represent the range of the Jacobi constant C where the family exists and the range where the family is stable.

In addition to the orbits listed, in the following analysis we include a few other closely related families for comparison and to better understand the relations of the branches. Some of these additional families do not result from the grid search, but rather from continuation past bifurcation points. Such "branch-switching", however, is not the focus of this work, and is not pursued systematically.

10.2.1 Stability

The diagram in Figure 10.4a shows the values of k_1 and k_2 along the A (terminator) family. It starts at a Hopf bifurcation with the equilibrium point L2, then follows a complex path that touches the $k = -2$ line twice tangentially. As described before, the value $k = -2$ is often associated with period-doubling bifurcations, and two of these indeed occur at the two points of contact, d1 and d2. Similarly, three period-tripling bifurcations happen when $k_i = -1$: t1, t2 and t3. The path also has

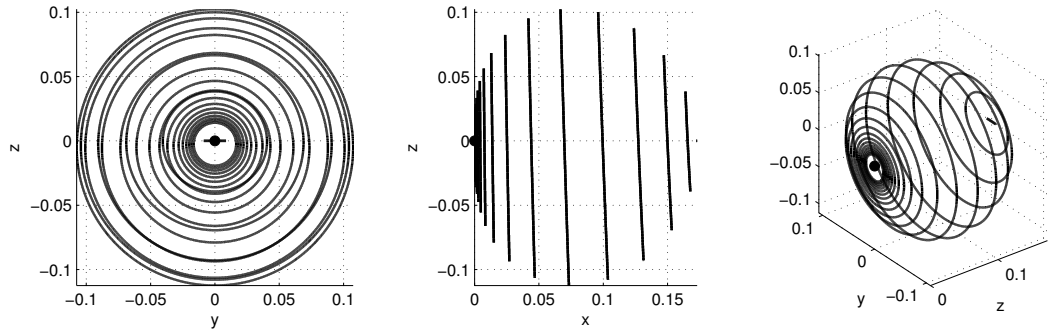

Figure 10.3. Family A of terminator orbits.

Table 10.1. Orbit families selected for continuation

Orbit ID	Family ID	C Range	Stable C
A3311	A	$[-\infty, -6.6312]$	whole range
B3323	B	$[C_{L2}, -6.8206]$	whole range
BB3324	BB	$[C_{L2}, -6.8206]$	none
C3321	C	$[-6.7636, -0.9408]$	$[-3.5980, -0.9408]$
CC3322	CC	$[-6.7636, -0.9408]$	$[-3.5980, -0.9408]$
D3331	D	$[C_{L2}, -6.6646]$	none
DD3332	DD	$[C_{L2}, -6.6646]$	$[-7.2684, -6.6646]$
EE3334	EE	$[C_{L2}, -7.3680]$	none
A2731	A27	$[-6.7794, -2.3037]$	whole range

a fold where it passes from instability to stability, at f1. The two indices then tend to $k_{1,2} = +2$ for $C \to -\infty$ as the family asymptotically approaches a simple Kepler orbit with decreasing radius. The same behavior is shown in Figure 10.4b, where the indices a_1 and a_2 are plotted. Here we see that a first portion of the family travels in the *even semi-instability* region on the left side of the plot (see Figure 6.1) until it enters the stability region in the middle.

The stability indices of three other orbits are shown in Figures 10.5 and 10.6. Like A, also B (Figure 10.5a) appears to bifurcate directly from the L_2 equilibrium point at one end, while at the other it is attached to A via d1, a period doubling bifurcation. B is stable for all values of C where it exists.

C (Figure 10.5b) stems from d2, the second period-doubling bifurcation of A. C has the peculiarity of having one of the two indices always equal to +2. In terms of monodromy matrix eigenvalues, this means that it has one more pair always +1, besides the already-acknowledged unitary pair characteristic of periodic orbits of this kind. As a result of this property, at each value of C the family has a

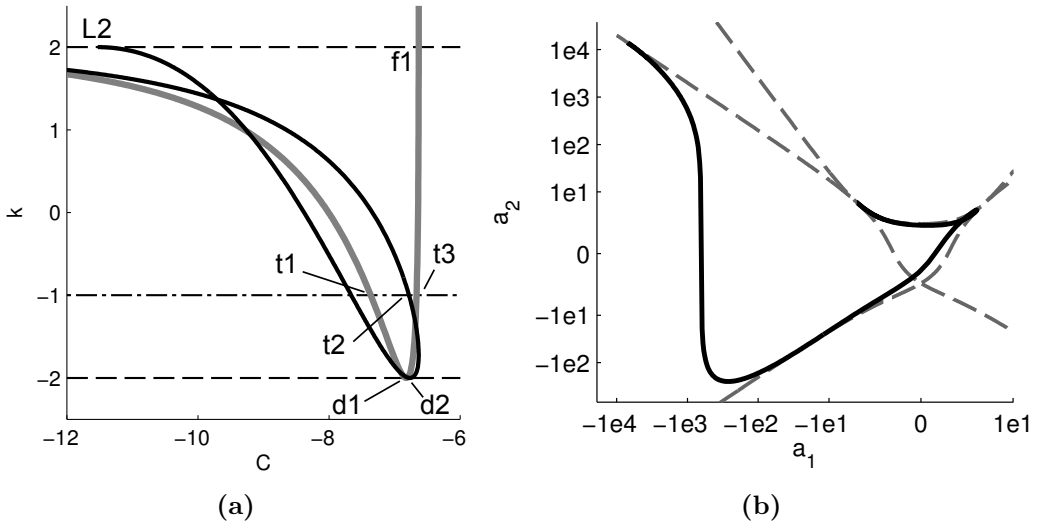

(a) **(b)**

Figure 10.4. (a) Stability diagram of family A. (b) Path of the same family on the a_1–a_2 plane.

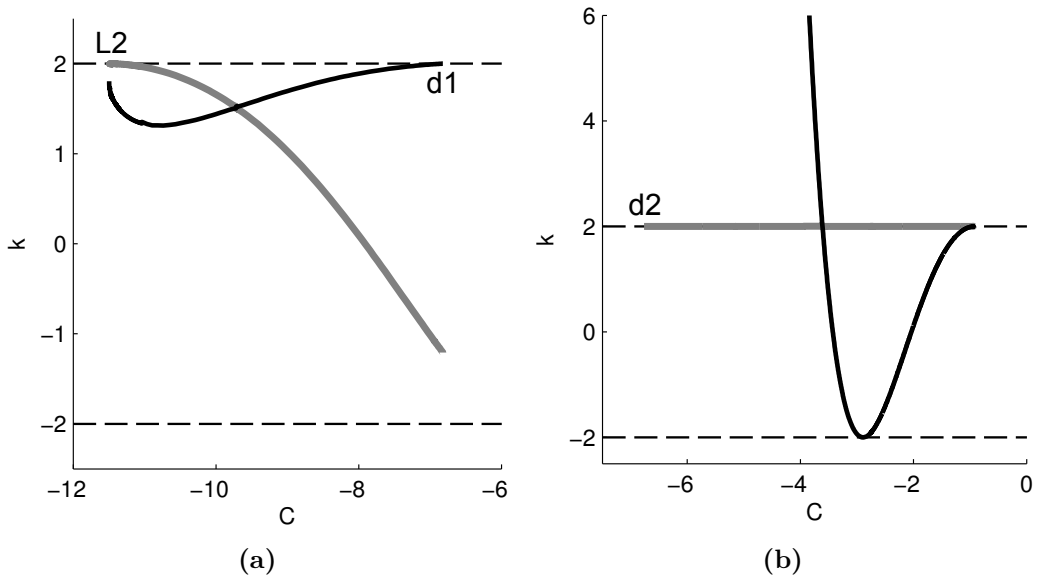

Figure 10.5. Stability diagrams of (a) B, (b) C and CC (identical paths).

bifurcation with another family with similar shape but rotated around the x axis. In fact, it is possible to construct this kind of trajectory with any orientation of its three "apocenters". Note that family CC is the reverse version of C and, while having slightly different shapes, they share the same eigenvalues. This sharing of the eigenvalues does not occur for any other family studied here, where prograde and retrograde orbits usually have different stability properties. We also note that family A27 has the same behavior and is indeed very similar to C except for the absence of a reversed version (which would be itself) and for the number of "apocenters", which in its case is four.

DD is an example of an orbit beginning with a period-tripling bifurcation of A, t3. It is the only one that enters the *odd semi-instability* region (Figure 10.6b) after passing through the stability region. A list of the energies of notable bifurcation points is included in Table 10.2. The first entry of the table, L2, has the energy of the L_2 equilibrium point.

Table 10.2. List of bifurcation points located during the numerical continuation.

Point ID	C	Connected Families
L2	−11.5342	A, B, BB, D, DD, EE
t1	−7.3680	A, EE
d1	−6.8221	A, B, BB
t2	−6.7794	A, A27
d2	−6.7640	A, C, CC
t3	−6.6646	A, D, DD
f1	−6.6312	A
b1	−0.9408	C, BB01

10.2.2 Period and Periapsis

Tracing the orbits along their families reveals the connections between different types of motion. Figure 10.7 shows the periods of seven families as C varies. A is the origin of most of the other families, which stem from it though period-doubling and period-tripling bifurcations. Families C and CC, whose periods are identical along their branches, bifurcate from A at d2 with twice its period (Figure 10.7a; the period of A is multiplied by two and its line is dashed). Then they evolve to higher energies up to bifurcation b1 at $C = -0.9408$, where they merge into a planar orbit (not shown) and with spatial orbit BB01 (see Section 10.4).

In a similar fashion, families B and BB, again with identical periods, detach from A at d1 with double period. They drift to lower values of C until they reach L2. Families C/CC and B/BB are bridged at their extremities by BB01.

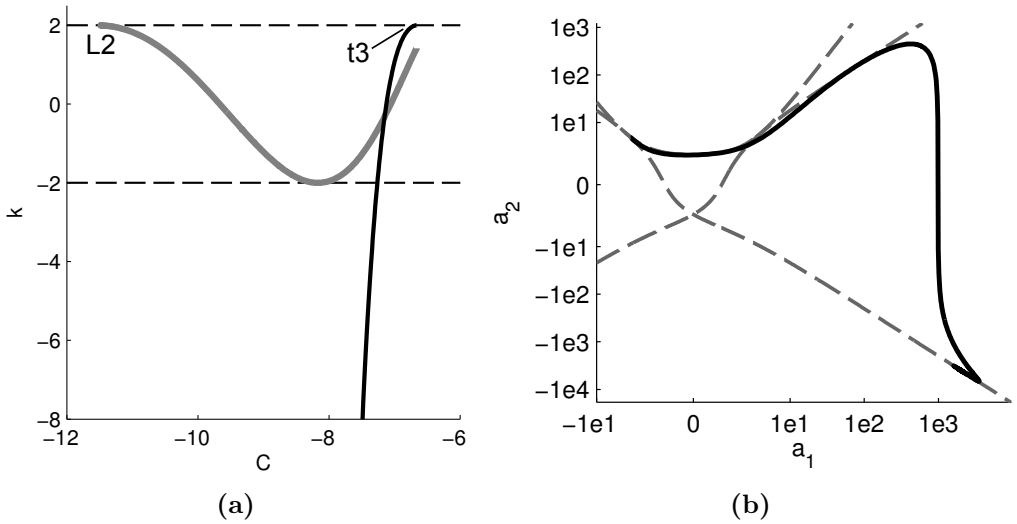

Figure 10.6. (a) Stability diagram and (b) a_1–a_2 plot of family DD3332.

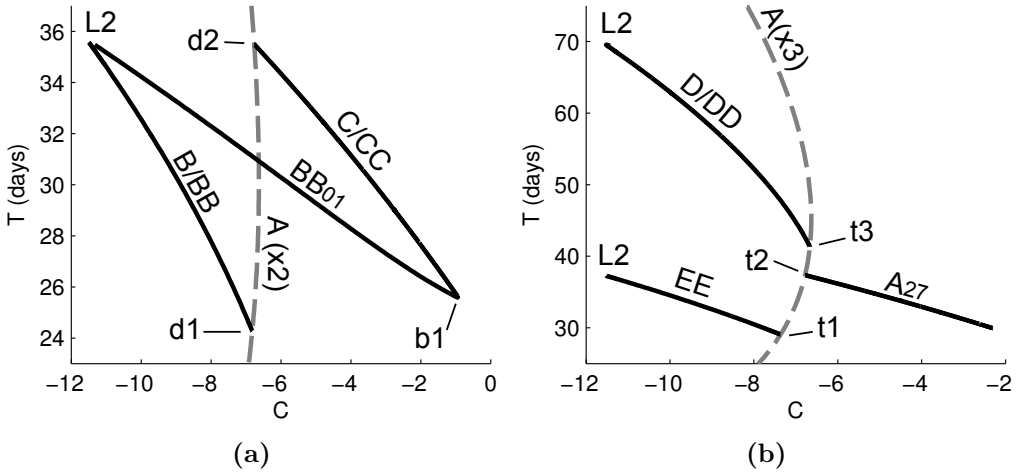

Figure 10.7. Period with respect to C. The A family is shown as a dashed gray line with its period multiplied (a) by a factor 2 and (b) by a factor 3.

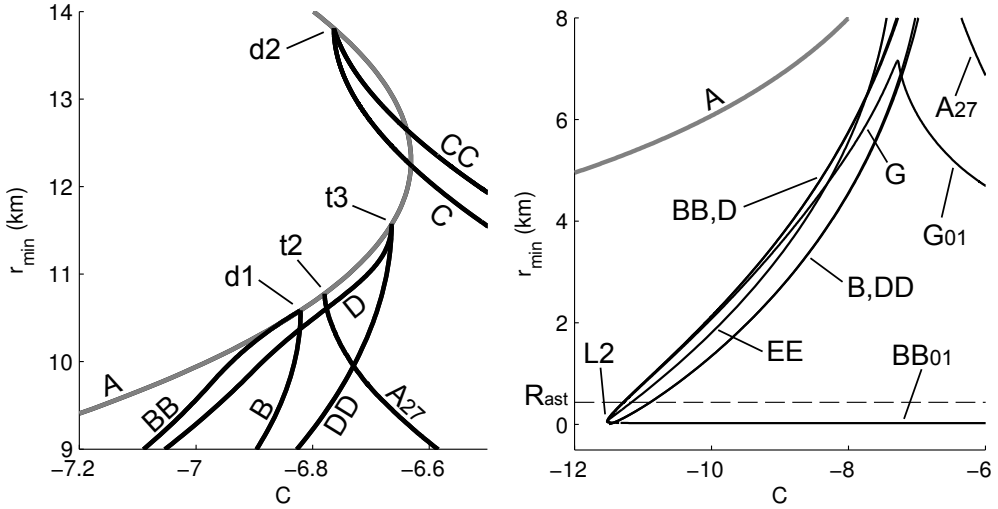

Figure 10.8. Distance of pericenter with respect to C. The gray line is family A, while the dashed line shows the radius of the asteroid.

Figure 10.7b shows three period-tripling bifurcation points on A from which E, EE, D and DD are originated. Both pairs of families evolve with identical periods down to L2, where they reduce to the equilibrium point through two respective Hopf bifurcations. Family A27, starting from t2, exists for higher values of C and becomes planar at its highest.

Figure 10.7 highlights a parallel between families B/BB with D/DD and EE, which exist for lower energies and extend in the $+x$ direction (away from the sun, see Section 10.3); and between families C/CC with A27, which have higher C and extend towards $-x$, or towards the sun. Indeed these two types of behavior are the "dark-side" and "sun-side" categories, respectively, described by Broschart et al. [4]. They exist for higher-order bifurcations from A, theoretically in a countable infinity.

The distance of closest approach to the asteroid, or pericenter distance, of all the selected families is shown in the two bifurcation diagrams in Figure 10.8. Diagram (a) shows A and the seven families bifurcating from it, already seen in Figure 10.7. Diagram (b) in Figure 10.8 shows another part of the same diagram, where the closest approach distance of most families tends to zero as the Jacobi constant approaches $C = C_{L2}$. In the vicinity of this point occur several Hopf bifurcations, and possibly also other types of bifurcations.

10.3 Periodic Orbits Resulting from the Grid Search Phase

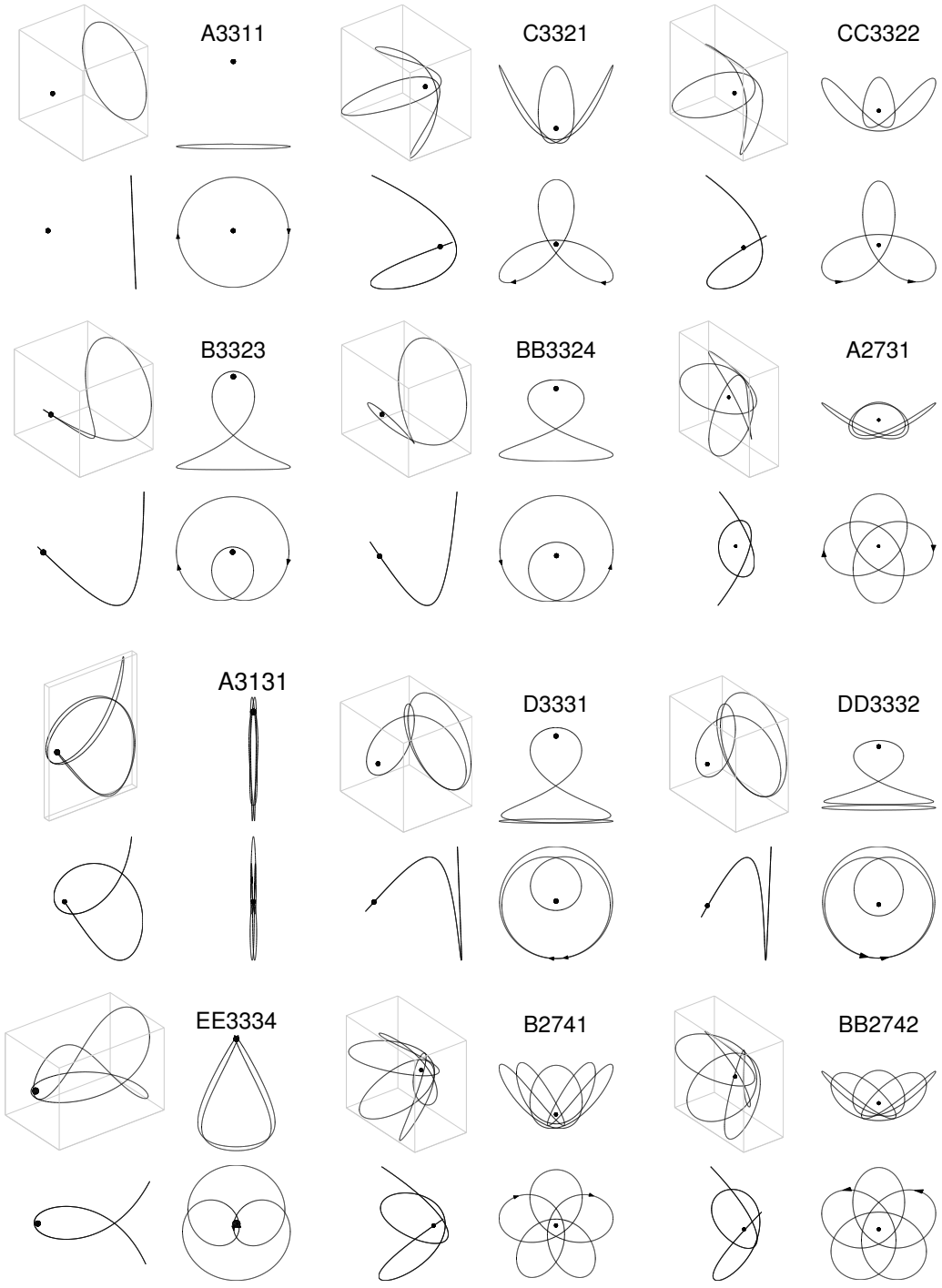

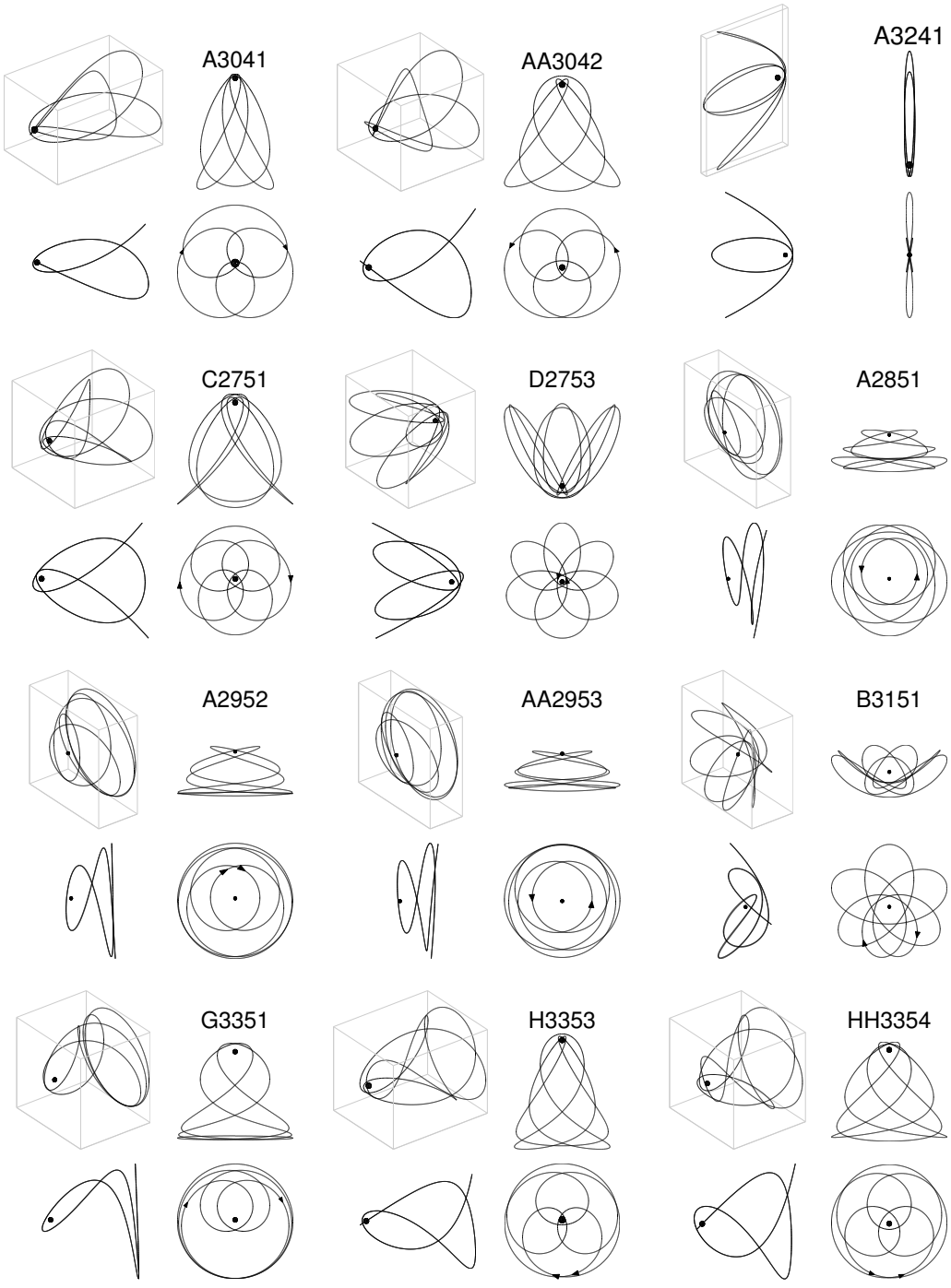
A3041
AA3042
A3241
C2751
D2753
A2851
A2952
AA2953
B3151
G3351
H3353
HH3354

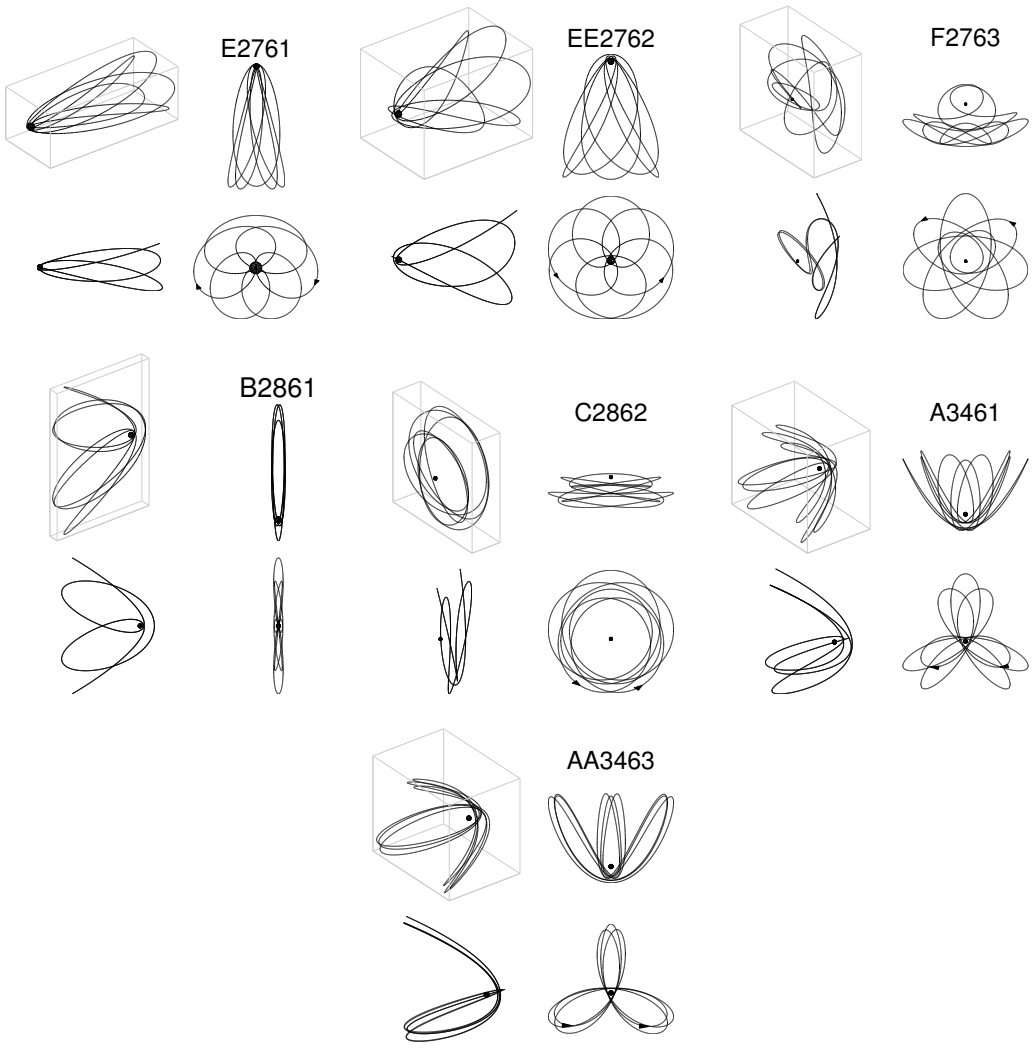
E2761
EE2762
F2763
B2861
C2862
A3461
AA3463

Table 10.3. Initial conditions of the orbits found with the grid search. $(y_0, \dot{x}_0, \dot{z}_0) = \mathbf{0}$ in all cases. Coordinates and periods are non-dimensional.

ID	Fam.	β	Cross#	x_0	z_0	$\dot{y}_0$	T
A3311	A	33	1	0.127680370	0.084952359	1.445775202	0.392906321
C3321	C	33	2	−0.106189341	0.110648109	0.842527695	0.382064198
CC3322	CC	33	2	−0.070929436	0.135971304	−0.772651580	0.410901143
B3323	B	33	2	0.131312562	0.079222416	1.341666098	0.431118325
BB3324	BB	33	2	0.117915183	0.098057075	−1.601496735	0.406528311
A2731	A27	27	3	−0.035946021	0.120217005	1.924384477	0.549535828
A3131	-	31	3	0.103337849	0.100379518	0.077713932	0.528742095
D3331	D	33	3	0.127764443	0.084825864	1.443440227	0.816916241
DD3332	DD	33	3	0.112510177	0.104214396	−1.714215194	0.753209388
EE3334	EE	33	3	0.143511864	0.054069632	−0.847949257	0.480473477
B2741	-	27	4	−0.082953645	0.094143175	1.449270392	0.551547849
BB2742	-	27	4	−0.058946064	0.110768254	−1.395079155	0.570961597
A3041	-	30	4	0.131369961	0.046682677	0.900129026	0.542990826
AA3042	-	30	4	0.122100486	0.067296436	−1.131003079	0.530348549
A3241	-	32	4	−0.102963600	0.107302700	0.208101786	0.417250366
C2751	-	27	5	0.109702753	0.060906079	1.330600144	0.600547693
D2753	-	27	5	−0.100742308	0.074801283	−0.720475579	0.571184567
A2851	-	28	5	0.080673171	0.102097607	−2.595302748	1.086970136
A2952	-	29	5	0.079888445	0.108540084	2.243929722	1.127767893
AA2953	-	29	5	0.074848315	0.112075167	−2.362945440	1.063046934
B3151	-	31	5	−0.034044166	0.139984833	1.396846341	0.938933506
G3351	-	33	5	0.127795217	0.084779495	1.441394171	1.240933538
H3353	-	33	5	0.140241640	0.062060153	1.047516701	0.923700280
HH3354	-	33	5	0.128773876	0.083285468	−1.331895398	0.886132265
E2761	-	27	6	0.123024500	0.024682323	0.636697326	0.640477509
EE2762	-	27	6	0.115735728	0.048471496	−0.852049270	0.631848120
F2763	-	27	6	0.107818903	0.064181998	−3.009013751	1.577520404
B2861	-	28	6	−0.091892490	0.092129541	0.244568674	0.541222994
C2862	-	28	6	0.035091133	0.125302412	−2.148750851	1.115359737
A3461	-	34	6	−0.099005695	0.123142416	0.710563863	1.115732413
AA3463	-	34	6	−0.113106469	0.110331812	−0.340150473	1.102526769

10.4 Plots of the Orbits Families

Families not listed in Table 10.1 are referred to by the name of their originating orbit.

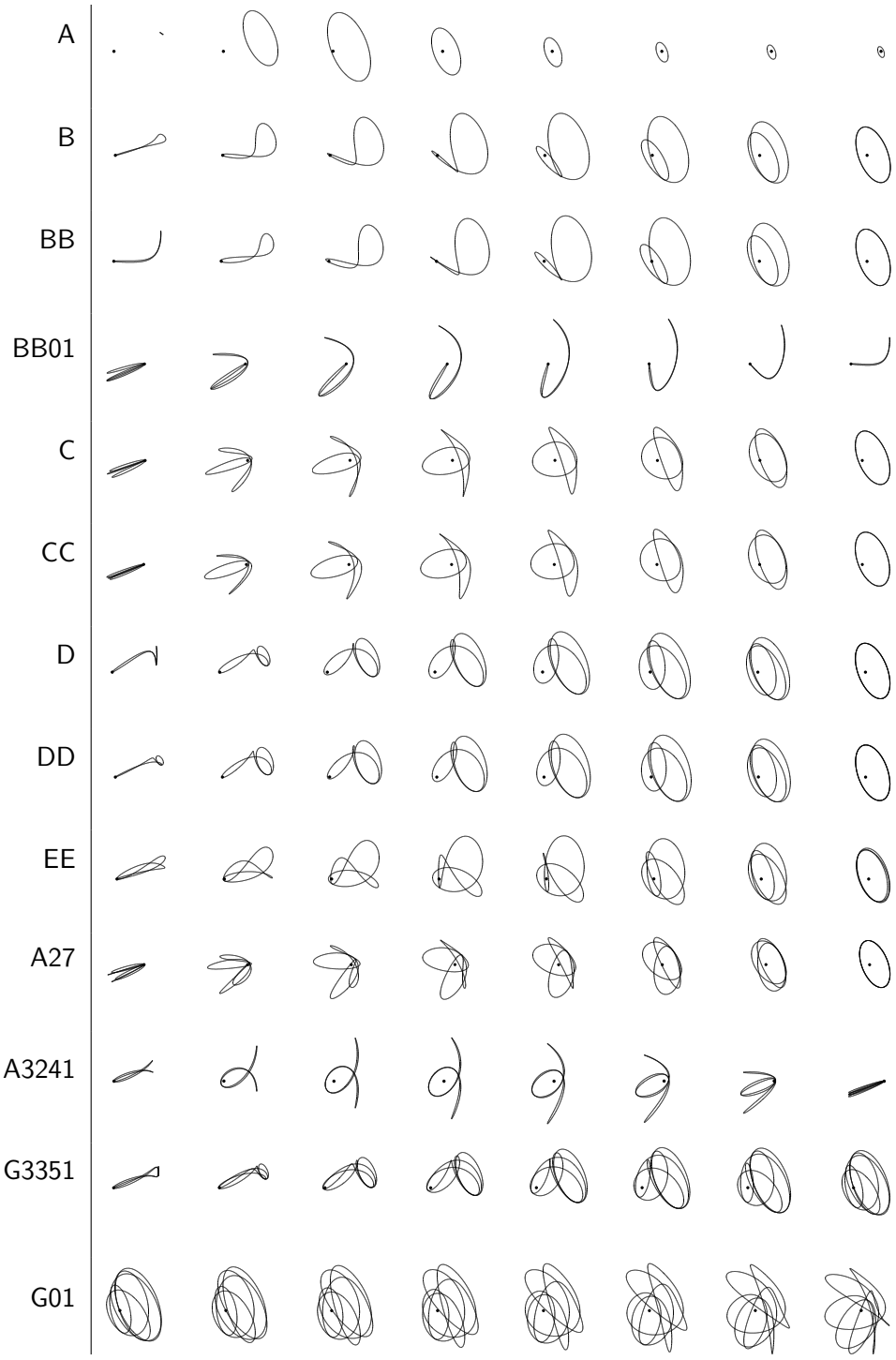

10.5 Solutions for Hayabusa 2

Not all of the orbits in the selected families are equally suited for Hayabusa 2's specific design requirements. We now proceed with the comparison of the families based on the following characteristics:

1. observability of the asteroid;
2. angles necessary for the observations;
3. sensitivity to Doppler measurements;
4. stability against parameter errors;
5. ground tracks.

These are described more in depth later in this discussion. The first three items in this list serve as a way to sieve out clearly unsuitable solutions. The remaining two, on the other hand, help us characterize and compare the most suitable ones.

Along a family branch the properties of the orbits may change drastically. It is thus necessary to select some orbits along each branch for a more complete comparison. For each branch, we sample six distinct orbits that capture the full variation of the family, excluding the trajectories that impact with the asteroid and those too close to bifurcation points, which would make them indistinguishable from the connected families. An example is given in Figure 10.9, where six orbits are taken along family BB on the C-r_{min} plane.

10.5.1 Comparison of Family Samples

The term "observability" (item 1 in the above list) here refers to the fraction of time in which each of the main navigation and observation instruments are capable of pointing towards the asteroid, given the 45° upper limit for γ, the sun angle. At any time, we consider the asteroid to be *observable* by an instrument if its geometrical center can be acquired inside the instrument's field of view without increasing γ above the limit. For instance, of all the instruments considered, ONC-W2 is the only one that can observe the asteroid both from the day side and from part of the night side, because it is mounted on the side of the spacecraft.

When the spacecraft's attitude (item 2) is changed to observe the asteroid, the direction of the solar radiation pressure force changes, affecting the dynamics. In Hayabusa 2's case the resulting deviation is very small, with an estimated maximum angle of the perturbing force vector of about 3° from the x axis. We therefore ignore this effect as a first approximation. Nevertheless, orbits that require large sun angles for long periods of time in order to use the instruments would make this simplification less realistic and lead to unpredictable outcomes. Thus we also compare the integral

$$\frac{1}{T}\int_0^T \cos\gamma(t)\,dt$$

of each orbit as a measure of how much the attitude is aligned with the sun direction. Clearly, $\gamma(t)$ depends on what instruments are being used and how they are selected

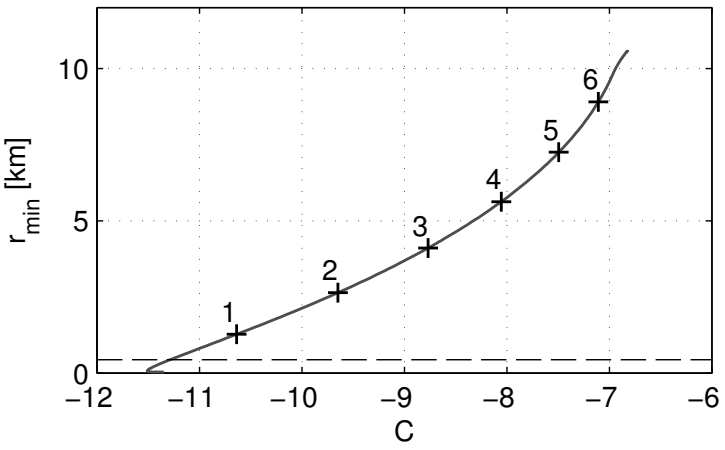

Figure 10.9. Six orbits selected along the whole branch of family BB.

at any given time. Several methods are possible, but here we employ the following simple strategy: use ONC-W1 whenever it is possible, and use ONC-W2 in the other cases (always respecting the 45° limit). The results for different strategies may differ, but this choice is a straightforward way to compare the orbits qualitatively.

Another measure of comparison is the ability to determine the spacecraft's velocity through the Doppler effect from the earth (item 3). While the exact direction of the earth in the Hill reference frame depends on the date, from the Japanese mission's design it is reasonable to assume that the earth would not be very far, angularly, from the sun as seen from the asteroid. Consequently, we can take the $-x$ direction, i.e. the direction of the sun, as the "Doppler sensitive" direction, and compare the orbits based on how much they are aligned with it during one period. This is measured by

$$\frac{1}{T}\int_0^T \frac{|\dot{x}|}{\sqrt{\dot{x}^2+\dot{y}^2+\dot{z}^2}}\,dt \ .$$

The comparison among different orbits is likely to remain valid even if the earth is not actually exactly in that direction.

Figure 10.10 shows the comparison measures for representative families BB and C, each divided in its six instances. The bars labeled "LIDAR", "ONCT", "ONCW1" and "ONCW2" refer to the observability of the asteroid with each of these instruments. An observability of 1 with an instrument shows that the asteroid can be acquired with it at all times from that orbit. The bars labeled "90°" show the fractions of time spent over the sunlit side of the asteroid. Finally, the "align." and "doppl." bars represent the sun angle integral (item 2), and the Doppler sensitivity integral (item 3) respectively. All these measures are defined in the range from 0 to 1.

For BB, the only instrument that gets a non negligible observable time fraction is ONC-W2, and only in the second part of the family. However, the orbits remain mostly over the dark side of the asteroid whenever ONC-W2 has good observation times. Also the sun-angles for observation and the Doppler sensitivity are generally lower than for C. The Doppler sensitivity, in particular, remains below 0.4 along

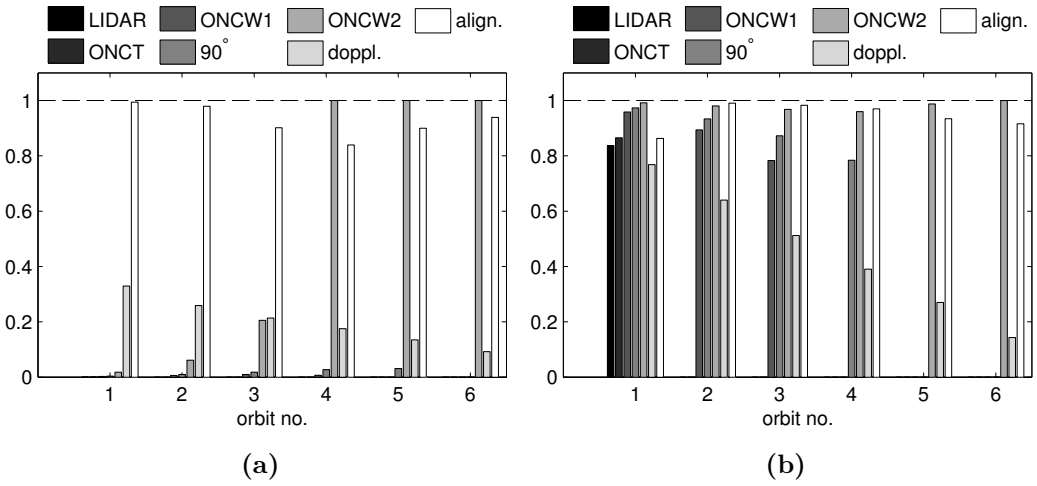

Figure 10.10. Comparison parameters of (a) BB and (b) C.

the whole family, showing that it would make velocity determination difficult.

Half of family C, on the other hand, has relatively high observation times for ONC-W1 and ONC-W2, including over the day side, and its orbit 1 also gives a coverage with LIDAR and ONC-T above 0.8. This particular orbit also shows high values of the last two measures, and is thus the most suitable choice between the two shown in the figure. Each of the other families closely follow the behavior of these two examples. Families B, D, DD and EE values similar to BB, as is to be expected from members of the "dark-side" group of solutions of Broschart et al. [4]. Conversely, A27 and CC are "sun-side" group solutions like C, and therefore have values very similar to it.

The exceptions, among the families studied in this work, are A and A3241, which are structurally different from all the others. A exists only on the night side, as can be seen in Figure 10.3, making observation impossible with anything except ONC-W2. Furthermore, these orbits have almost no sensitivity to Doppler measurements. For these reasons A is not a feasible option for Hayabusa 2. One extreme of family A has parameters similar to orbit 1 of family C, with the exception of lower LIDAR and ONC-T observability. It would be an interesting candidate for application, but it is invalidated by the fact that it crosses the asteroid's shadow.

10.5.2 Robustness and Ground Tracks

The result of the above comparisons is the restriction of choice to the three "sun-side" group orbits, C, CC and A27. All three behave in very similar ways relative to the measures given until now. Figure 10.11 shows the results of a set of simulations of C, CC and A27. For each of these, we simulate the sample orbit with the lowest pericenter distance of all six, which is also the one with the best parameters in the bar plots like those in Figure 10.10. To each orbit we apply errors in the parameters in gradual steps, and propagate the orbits for six periods. Two of the lines represent the time at which the distance from the origin becomes two or four times larger than the unperturbed maximum distance, indicating a risk of gravitational escape.

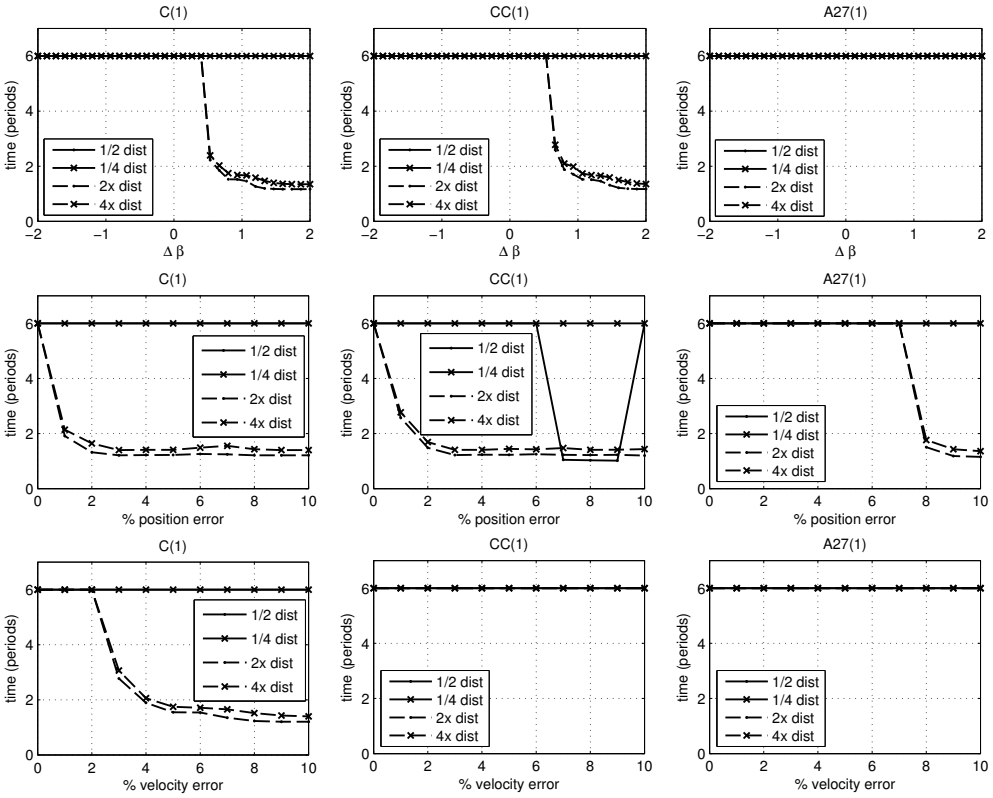

Figure 10.11. Outcomes of the simulations with errors in the SRP constant β (top row), in the initial position (middle row) and in the initial velocity (bottom row). See text for description.

The other two lines represent the time at which the distance becomes 1/2 or 1/4 of the unperturbed minimum distance, with high risk of impact. These data give a simple estimate of how resilient these orbits are in the presence of initial model or orbit determination errors. The trajectories that remain within the upper and lower limits for the full six periods of simulation are shown with ordinate values of 6, but this is only the lower limit, as they may remain bounded for longer durations.

The top row in Figure 10.11 shows the outcomes of the three orbits for an error in the estimated value of β, ranging from $\beta - 2$ to $\beta + 2$. The middle and bottom rows give the same type of data relative to initial errors in position and velocity, respectively. These errors are applied in steps from 0% to 10% of the initial value, i.e. the initial distance from the origin for the middle row and the initial velocity for the bottom row. In turn, the initial errors are applied in 14 directions uniformly distributed over the whole sphere, and only the worst outcome is saved.

Regarding the errors in β, the results in Figure 10.11 indicate that C and CC behave similarly, and become unstable when $\Delta\beta \simeq +0.5$, as they tend to escape from the asteroid within two periods. For the duration of the simulation they remain bounded for any lower value of β. Conversely, family A27 stays bounded in the whole tested range of β (all four lines coincide with the limit value of 6).

From the middle row of plots in Figure 10.11 it is evident that C and CC escape even with a 1% initial error in position, while A27 is bounded up to 8%. Family

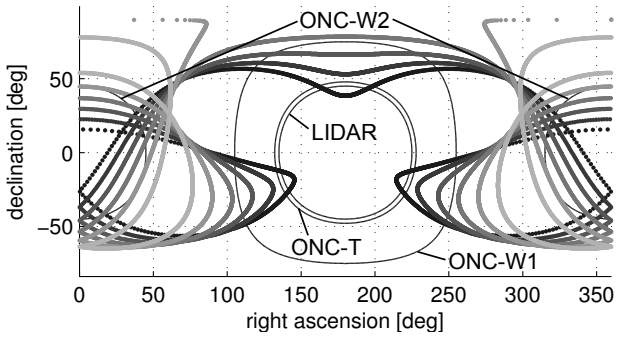

(a)

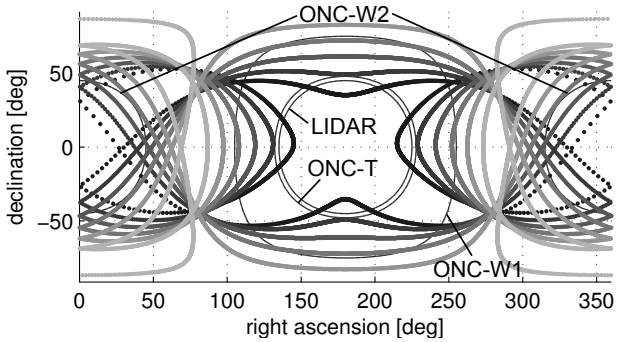

(b)

Figure 10.12. Angular tracks of six instances of families (a) C and (b) A27. Each orbit is shown in a different shade of gray, from darkest (orb. 1) to lightest (orb. 6).

CC also shows a tendency to get closer to the asteroid when the errors are large. Concerning the errors in velocity in the bottom row, both CC and A27 appear to be resilient at least up to 10% errors. Only C escapes from the asteroidal gravity when the velocity error is greater than 2%. In general, all three orbits appear to be prone to escaping, but their risk of impact with the asteroid is low.

Figure 10.12 shows the right ascension and declination of the sample orbits of C (CC has similar shapes) and of A27. These two types of trajectories have, respectively, three and four apocenters (see Section 10.4). The figure also shows contours for levels of the sun-angle necessary to acquire the asteroid with each of the four navigation instruments. The $[90^\circ, 270^\circ]$ range of the right ascension corresponds to the sunlit side of the asteroid. Because A27 has one additional apocenter but periods longer than C/CC by only approximately 15% (for equal r_{min}), it follows that A27 has shorter revisit times of the day side, as well as of the low-γ areas. This property helps reduce the orbit determination errors. The coverage with the optical cameras is also more uniform for A27, potentially leading to more complete surveys of the surface in fewer periods.

The four-period ground track of orbit 1 in family A27 is shown in Figure 10.13 in surface latitude and longitude. The figure contains only the parts of the orbits where either LIDAR, ONC-T or ONC-W1 can observe the asteroid with sun angle less than 45°, color coded to show the distance from the center of mass at each point.

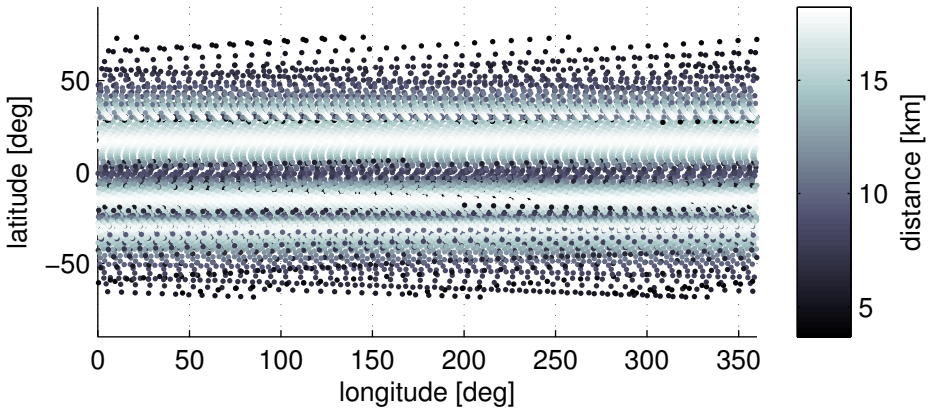

Figure 10.13. Ground track example of orbit 1 of A27.

Here we assume the rotational model with the highest confidence given by Müller [43] and a rotation axis parallel to the y–z plane at the beginning of the integration. In this configuration, nearly all the latitudes are accessible for observation, but the polar regions receive fewer visits. The use of ONC-W2 would overcome this problem.

From the above considerations, family A27 appears to be the most suitable for Hayabusa 2 among those analyzed in this work. Orbit 1 of A27 provides good coverage of the asteroid surface, relatively favorable features for orbit determination and robustness in the presence of small model and state errors. We should note that it is not necessarily the best solution, because there are "sun-side" group orbits, with higher numbers of apocenters and longer periods, not studied here. The relevant result, however, is that this type of motion, including C/CC and longer variants, has the properties necessary for the next Japanese sample-return mission. Further studies can then derive from this conclusion higher fidelity solutions similar to these but including the other perturbations and a more detailed characterization. In fact, the elliptic version of Hill's Problem with radiation pressure admits quasi-periodic solutions with structures and behaviors resembling the periodic orbits shown above [31]. These appear to be the most feasible strategies in an actual mission of this kind, and are currently the subject of further study by several groups.

Chapter 11

Active Stabilization of the Periodic Orbits

All the periodic solutions found with the steps described until now are valid in a simplified model of the dynamics, Hill's problem with solar radiation pressure. This assumes that the asteroid is in a circular orbit around the earth, that the asteroid is perfectly spherical and uniform and that no other solar system body affects the spacecraft's motion. These assumptions make the solution of the problem easier, but are not a good representation of reality. As a consequence, the natural orbits detailed up to this point in general cease to exist in a less regular environment.

One way to proceed towards a higher-fidelity model is to use the above orbits as a basis to discover useful solutions that include the perturbations. This approach is the one taken in Section 12. However, we can try to exploit the available solutions in another way. We might consider using the periodic orbits as they are, in their ideal forms, and account for the additional perturbations through an active control process.

In this section, we use a linear quadratic regulator, the formulation of which is contained in Section 8, to stabilize the periodic orbits in the presence of other perturbations. We are thus able to give a good estimate of the type and intensity of the control effort necessary to sustain the periodic orbits. Whether Hayabusa 2 would be able to implement such control is another matter, due to the restrictions in the pointing of the ion engines. Still, it is useful to know how the different perturbations influence the motion and how difficult it would be to correct them.

The following subsections introduce gradually more important effects into the equations of motion, showing the resulting orbits controlled though our LQR.

11.1 Constant Perturbation

We first apply the LQR algorithm to a disturbance corresponding to a constant force in a random direction. It is the simplest form of perturbation and serves as an initial test to evaluate the regulator.

The properties of the controlled orbit are exemplified in Figure 11.1, where a perturbing force of 0.1 N is applied in a constant direction chosen randomly. The orbit is controlled with linear integral feedback (see Eq. (8.7)) for one period. Plot

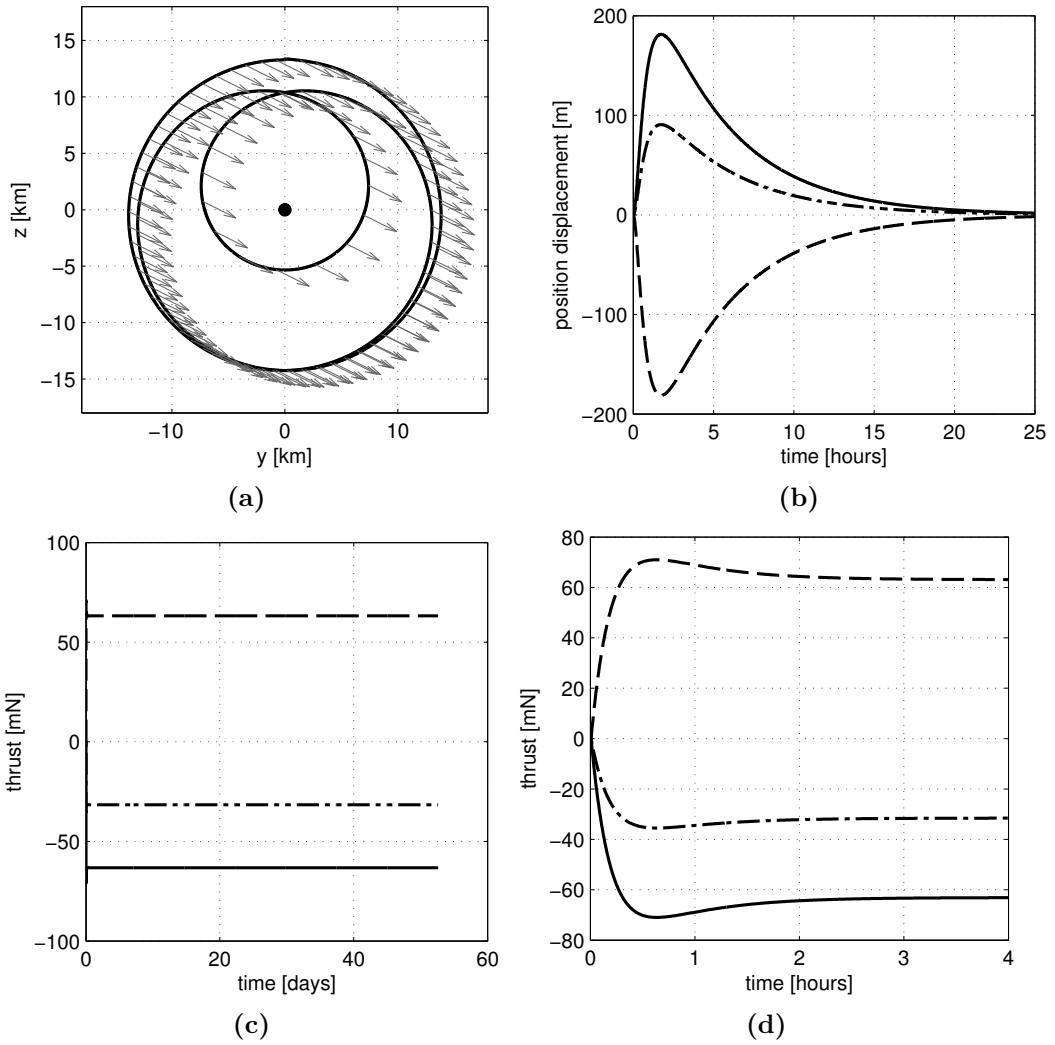

Figure 11.1. Orbit type D with $C = -8.0626$, subject to a constant perturbation and stabilized for one period by the LQR with integral term. Solid lines: x components; dashed lines: y components; dashed-dotted lines: z components.

(a) in the figure shows the trajectory as seen from the sun-asteroid line, but the difference between the nominal and the actual paths is not visible at this scale. The arrows indicate the direction of thrust.

The distance between the real and the nominal trajectory, during the first day, is shown in the plot in Figure 11.1b. The regulator starts and ends with zero control, therefore it needs some time to grow continuously to the necessary intensity and to decrease again at the end of the period. For the first 2 hours circa the control is still growing and insufficient, causing a brisk increase in the displacement. Without the integral term in the control, this displacement would remain constant and non-zero for most of the orbit's period. With the integral term, however, the displacement returns almost to zero within the first day of orbit. The displacement from the nominal velocity, although not shown, has the same structure as that in position, magnitudes ranging from 10^{-4} m/s to 10^{-3} m/s. The same is true for all the other

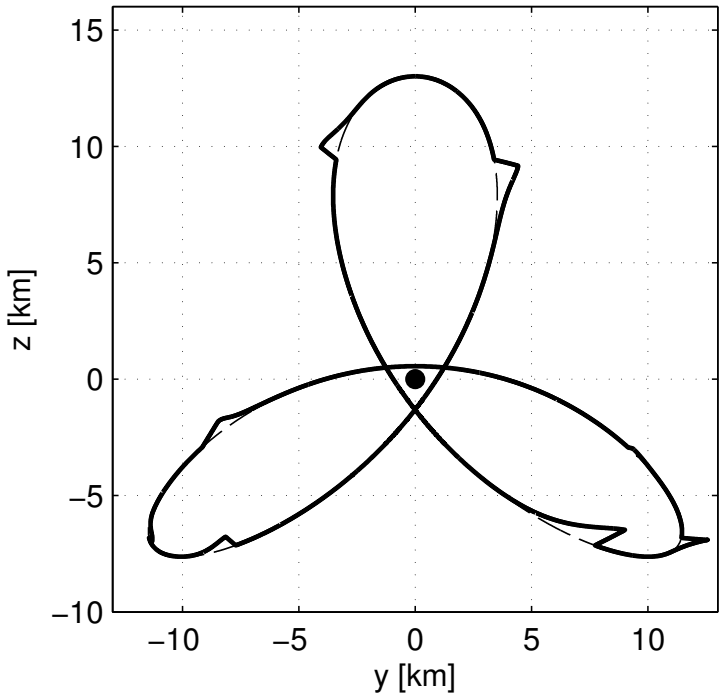

Figure 11.2. Orbit of family C ($C = -2.267$) affected by random instantaneous perturbations and controlled with the LQR algorithm.

examples in the following sections.

Plots (c) and (d) show the thrust history which, as expected, simply works to cancel out the constant perturbation. The initial overshooting phenomenon described above is visible in the close-up of the thrust history in the bottom-right plot, corresponding to the first four hours of control.

Most of the above results depend on the weights chosen in the LQR cost function. In this case, the control is affected by the weights only at the extremes of the interval of application. Weights that penalize the control decrease the overshooting phenomenon at the expense of wider displacements of the trajectory, and vice versa.

11.2 Random Instantaneous Errors

Next, we test the behavior of the LQR-controlled orbits in the presence of another type of random perturbation, which introduces errors in the position and velocity of the spacecraft at regular intervals. These errors are applied almost instantaneously, and their directions and magnitudes are chosen at random using normal distributions.

While this type of disturbance is still not something that occurs in reality, it simulates the result of a non-continuous orbit determination scheme. Because of the restrictions on the attitude of the spacecraft relative to the asteroid, for long periods of time it may not possible to measure its position and velocity in a satisfying way. When such measurements do occur, the discovered state may be substantially off from the nominal value. These simulations test the response of the LQR algorithm to sudden errors of this kind.

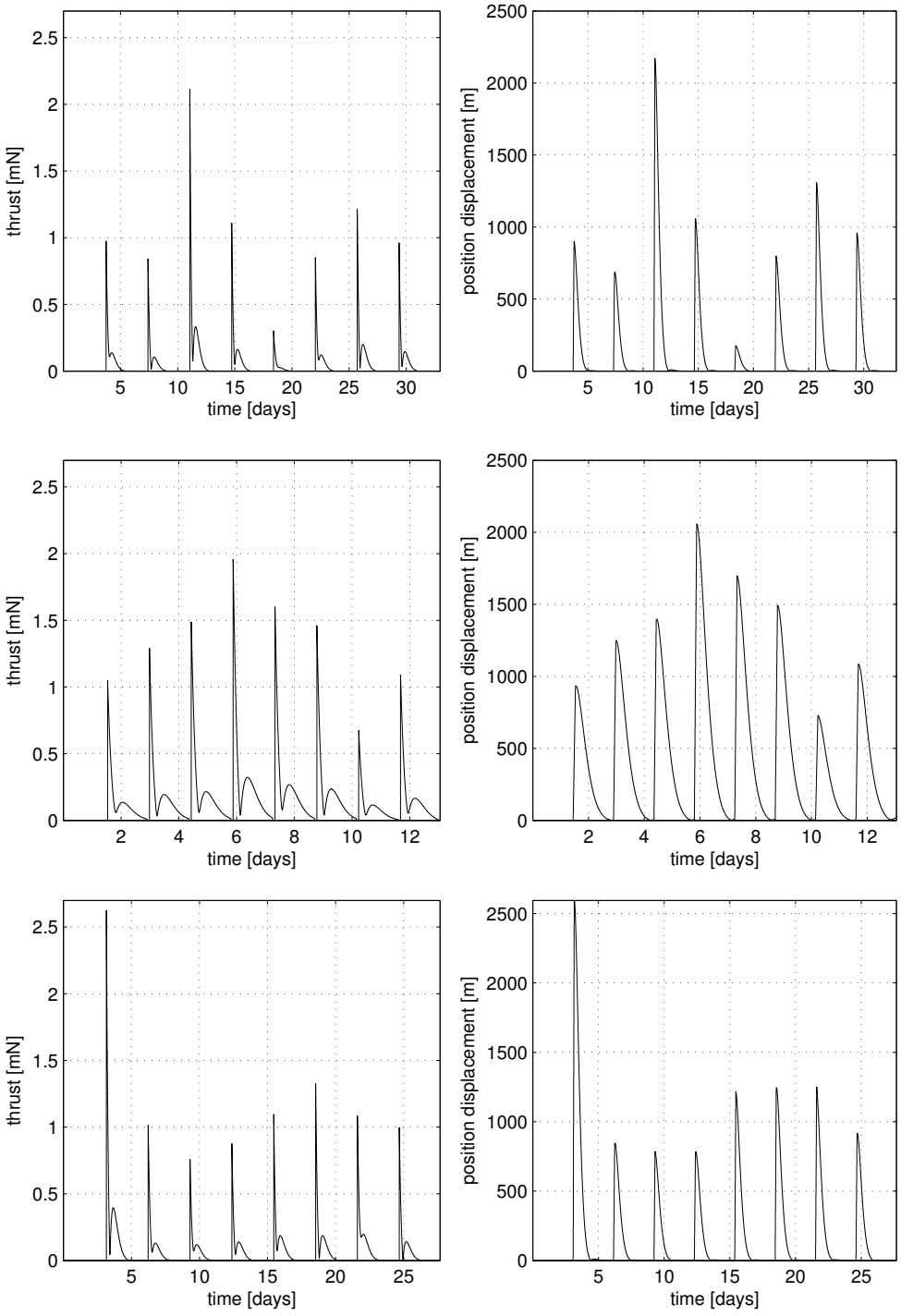

Figure 11.3. Random Instantaneous errors controlled by LQR. Thrust and displacement histories of (respectively by row): A with $C = -11.093$, A with $C = -6.717$ and B with $C = -7.959$.

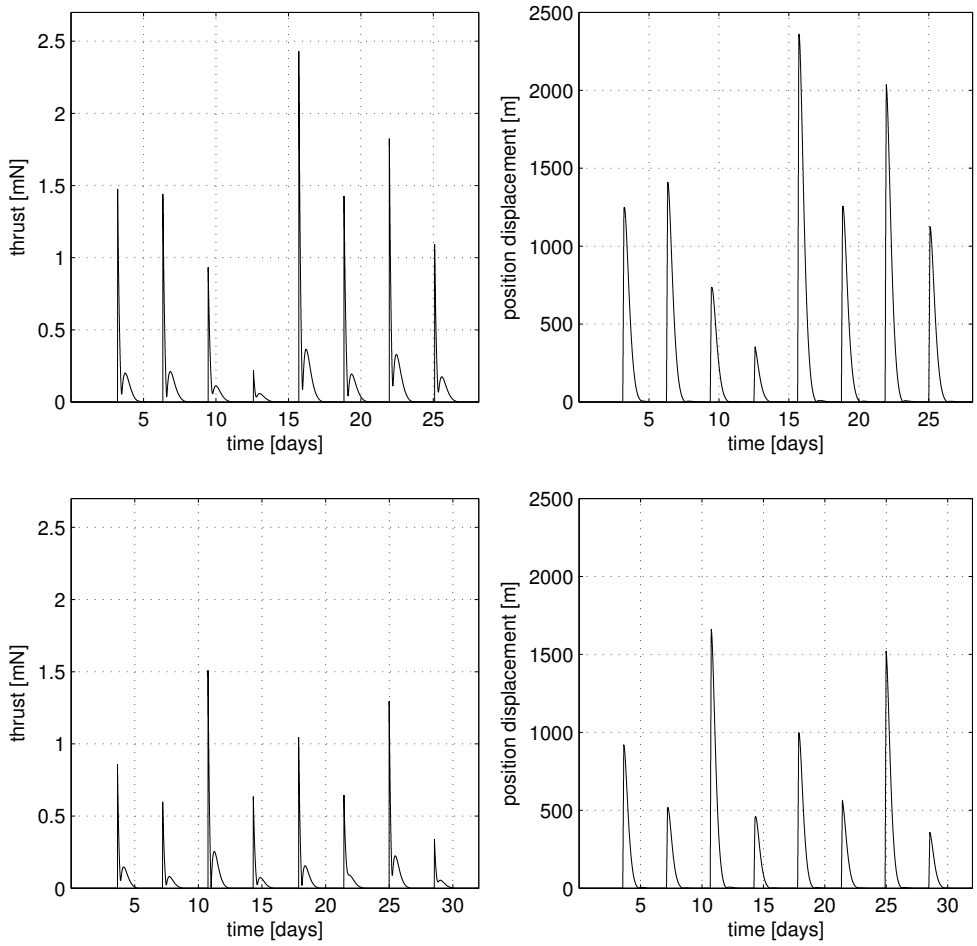

Figure 11.4. Random Instantaneous errors controlled by LQR. Thrust and displacement histories of (respectively by row): C with $C = -2.267$ and C with $C = -4.529$.

Figure 11.2 shows the nominal (thin dashed) and real perturbed (thick solid) trajectory of a C type orbit, chosen with $C = -2.267$, projected on the y–z plane. Along the orbit, errors are introduced artificially 8 times. The regulator manages to make these two trajectories coincide, except for short periods of time after an instantaneous error occurs. The thrust and position displacement histories of this and other orbits are included in Figures 11.3 and 11.4. These figures give several examples to compare the behavior of orbits with different parameters.

In two cases the same orbit family is given twice for different locations along their respective family branches. This is done for family A (top and middle rows of Figure 11.3), and for family C (Figure 11.4). In both pairs the closest approach distance, as well as the period of the orbits, change. The same is true for the additional orbit shown, with geometry and properties very different from the others. Notwithstanding, the results are similar in every case.

The error in position is of the order of 1 km, and that in velocity is close to 0.01 m/s. All the examples given have been produced with the same weights of the cost function. For this choice of the weights, in all cases it takes about 1.5 days to

Table 11.1. Periodic orbits simulated with Models 1 and 2.

ID	Family	C	r_{min} [m]	Model
ID1	A	−6.717	11133	1, 2
ID2	C	−1.733	1117	1, 2
ID3	C	−2.417	2241	1
ID4	C	−3.667	4478	1
ID5	DD	−10.783	536	1, 2
ID6	DD	−10.238	1078	1
ID7	DD	−9.353	2158	1

bring the trajectory back to its nominal path after an error has occurred. Some orbits have shorter periods, like the A orbit in the middle row of Figure 11.3, and the intervals between the 8 errors are shorter, but the response to the errors is the same. For all orbits the necessary thrust is of the order of 1 mN for the initial spike and 0.1 mN for the successive tail, while the total Δv during a whole period is 0.3 m/s to 0.45 m/s.

This similarity in the results is probably explained by the size of the errors, the control of which is of a larger scale with respect to the other forces acting naturally in the system.

11.3 Spherical Harmonic Terms of the Potential

For orbits that approach the asteroid very closely, the effect of the gravitational irregularities may become important. The shape model of Hayabusa 2's target, 1999 JU3, is not yet known in detail, but its properties have been somewhat constrained through light-curve observations [1, 12, 43]. Through the equations introduced in Chapter 9, we approximate its shape as a triaxial ellipsoid with up to the 4th degree and order polynomial terms and propagate the periodic orbits with the LQR algorithm.

We present here the results associated with two hypothetical shape models. Model 1 is almost spherical, with principal axes

$$\text{Model 1: } [899.8\,\text{m}, \quad 869.9\,\text{m}, \quad 808.6\,\text{m}] \ .$$

Model 2 has dimensions

$$\text{Model 2: } [1017.2\,\text{m}, \quad 860.7\,\text{m}, \quad 782.5\,\text{m}] \ ,$$

and thus is more elongated than Model 1. The asteroidal rotation period and the ecliptic latitude of the rotation axis were taken from the results by Müller et al. [43] (see Section 2.6), while the longitude of the rotation axis in Hill's reference frame and the initial angle around it were chosen randomly and evolved during the simulations. The orbits listed in Table 11.1 were simulated with in this mode. The minimum distance r_{min} from the center of the asteroid is also reported for each orbit in the table.

Figures 11.5–11.7 show the results of the simulations with Model 1. The plots in the left columns display the thrust history necessary to follow the nominal trajectory;

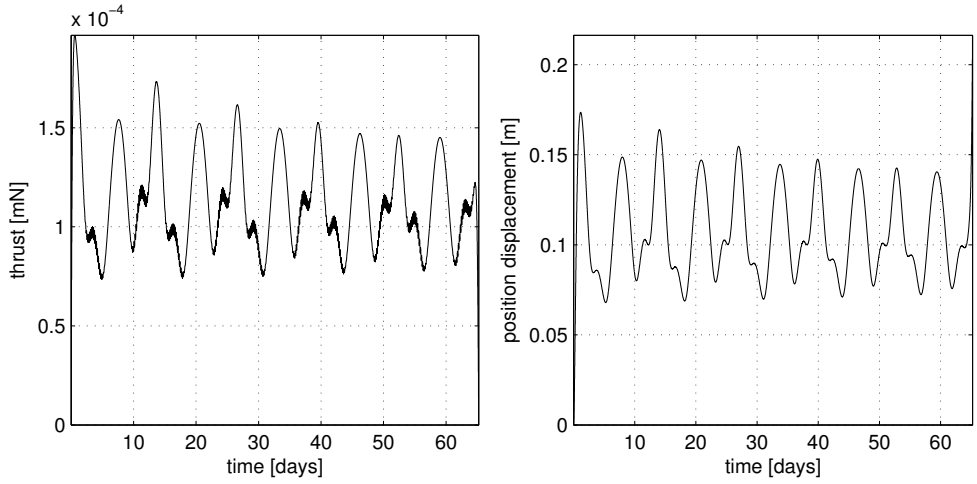

Figure 11.5. Spherical harmonic perturbations controlled by LQR in Model 1. Thrust and displacement histories for 5 periods of family A (ID1).

those on the right show the position displacement throughout the orbit. As should be expected, the distance from the asteroid is the main factor, with most of the control effort concentrated in the periods of close approach.

Terminator orbit A (ID1 in Table 11.1), shown in Figure 11.5, is almost circular and has a uniform distance from the asteroid (Chapter 10). As a consequence, the necessary correction is small, of the order of 10^{-4}mN, and spread out along the whole trajectory. The position error is of a few centimeters to a few decimeters, and the 1–period Δv is 1.610×10^{-3} m/s.

The results are different for orbit family C (ID2–ID4), which consists of three close approaches during one period (Figure 11.6), and for family DD (ID5–ID7), with only one very close approach (Figure 11.7). For both families, the control is concentrated in short intervals where the distance from the asteroid is shortest. While the general shape of both control and displacement histories is similar for members of the same family, they differ quantitatively depending on how close they get to the central body. In Figure 11.6 there are peaks of about 0.4 mN for the thrust and 160 m for the displacement in the smallest orbit (top row), but the peaks quickly decrease in size as the orbits get wider and farther from the asteroid. The Δv varies from 2.391×10^{-3} m/s to 3.552×10^{-2} m/s. Figure 11.7 displays the same behavior, although with more pronounced peaks and roughly the same range of Δv. Note that both orbit the C and DD families end in a bifurcation with A, so that their control properties tend to coincide with that of Figure 11.5 at the respective ends of their branches.

The more elongated Model 2 was applied to three of the orbits listed in Table 11.1 for comparison with Model 1. The thrust histories resulting from these simulations are shown in Figure 11.8. The structures of the LQR results are the same as those shown in the previous figures, but the stronger perturbations result in control intensities of roughly twice those of Model 1. The exception is DD (ID5), which has a lower peak due to the specific orientation of the asteroid during the fly-by.

It is important to note again that all the above results depend critically on

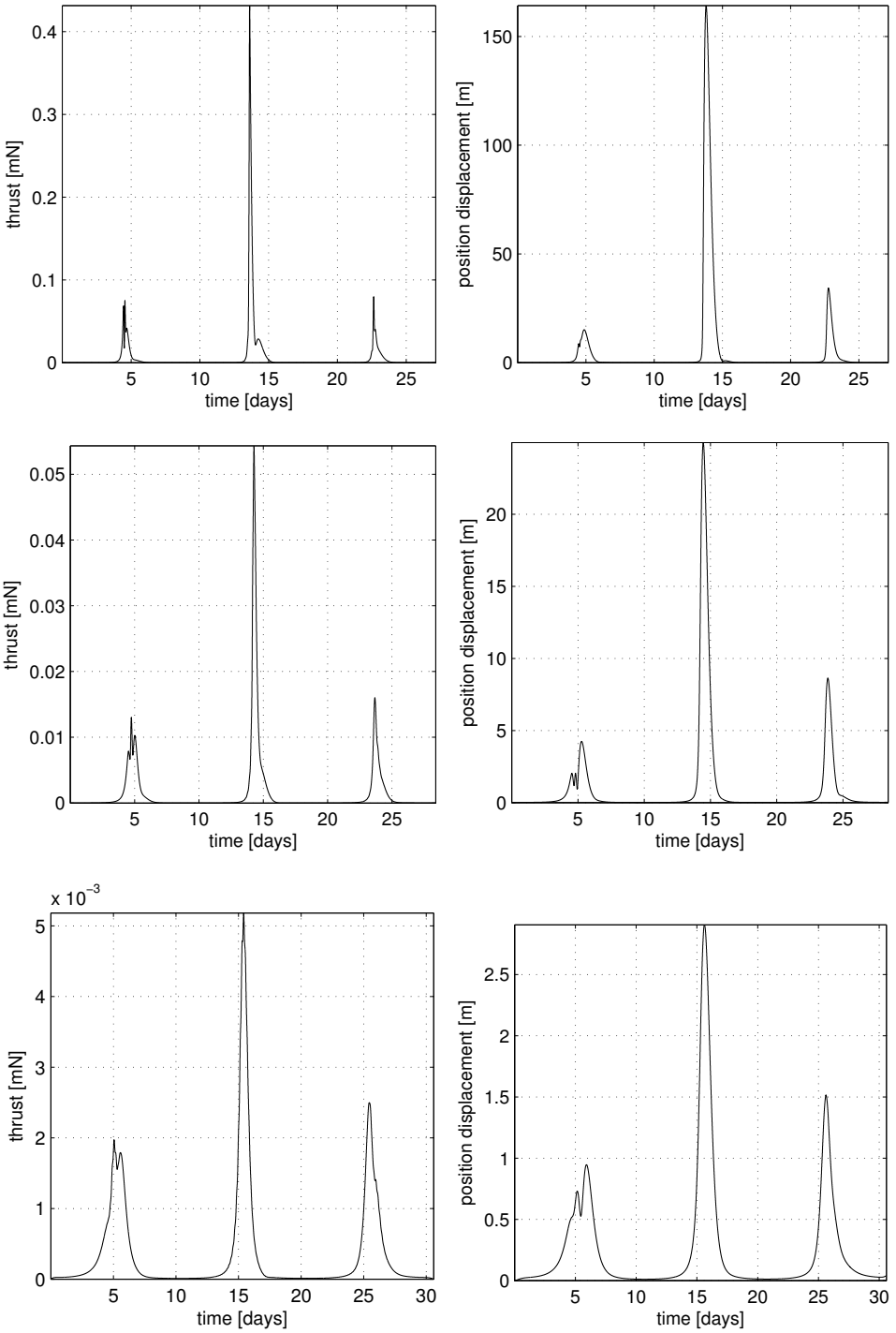

Figure 11.6. Spherical harmonic perturbations controlled by LQR in Model 1. Thrust and displacement histories of (respectively by row): C (ID3), C (ID4) and C (ID5).

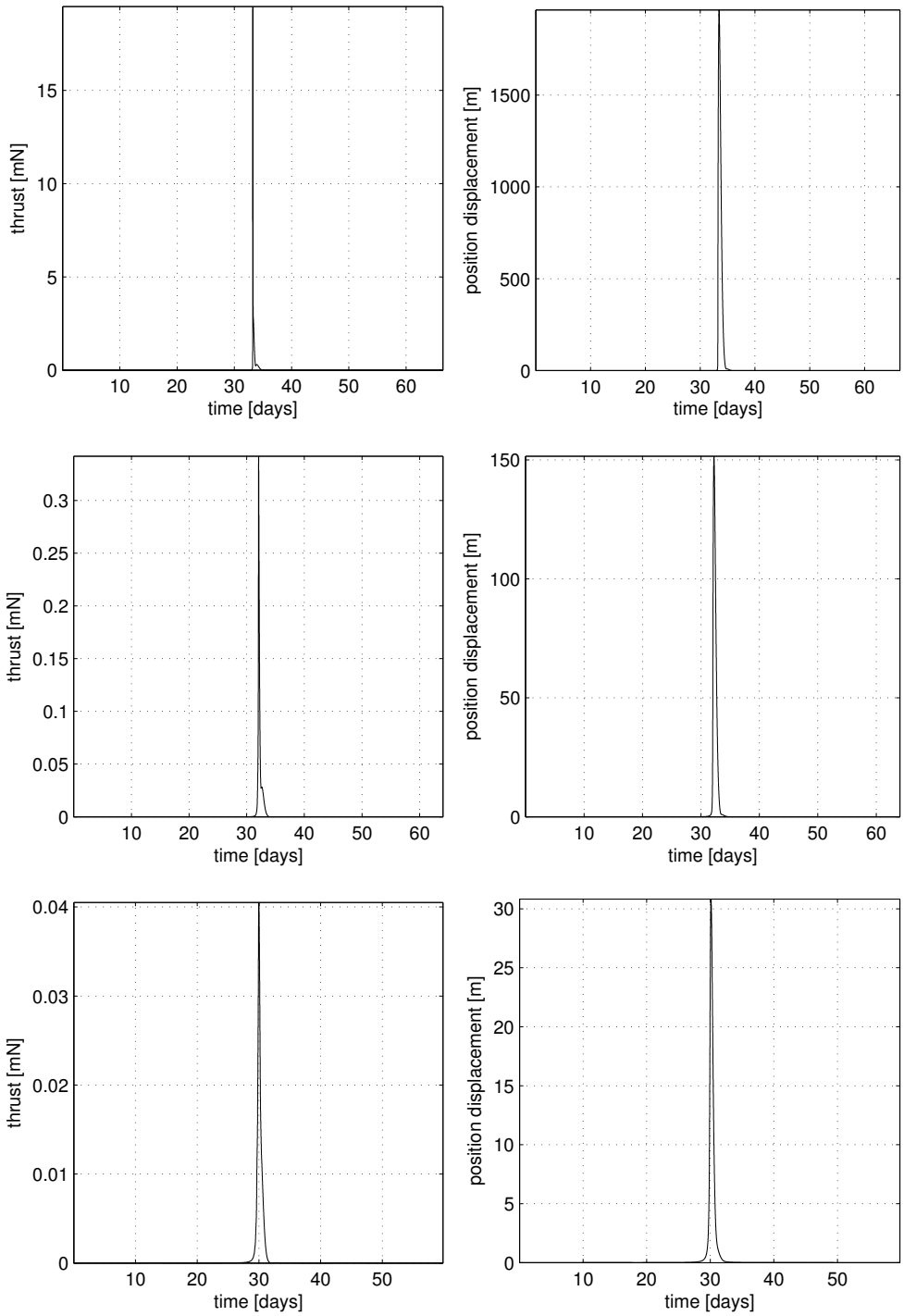

Figure 11.7. Spherical harmonic perturbations controlled by LQR, Model 1. Thrust and displacement histories of (respectively by row): DD (`ID6`), DD (`ID7`) and DD (`ID8`).

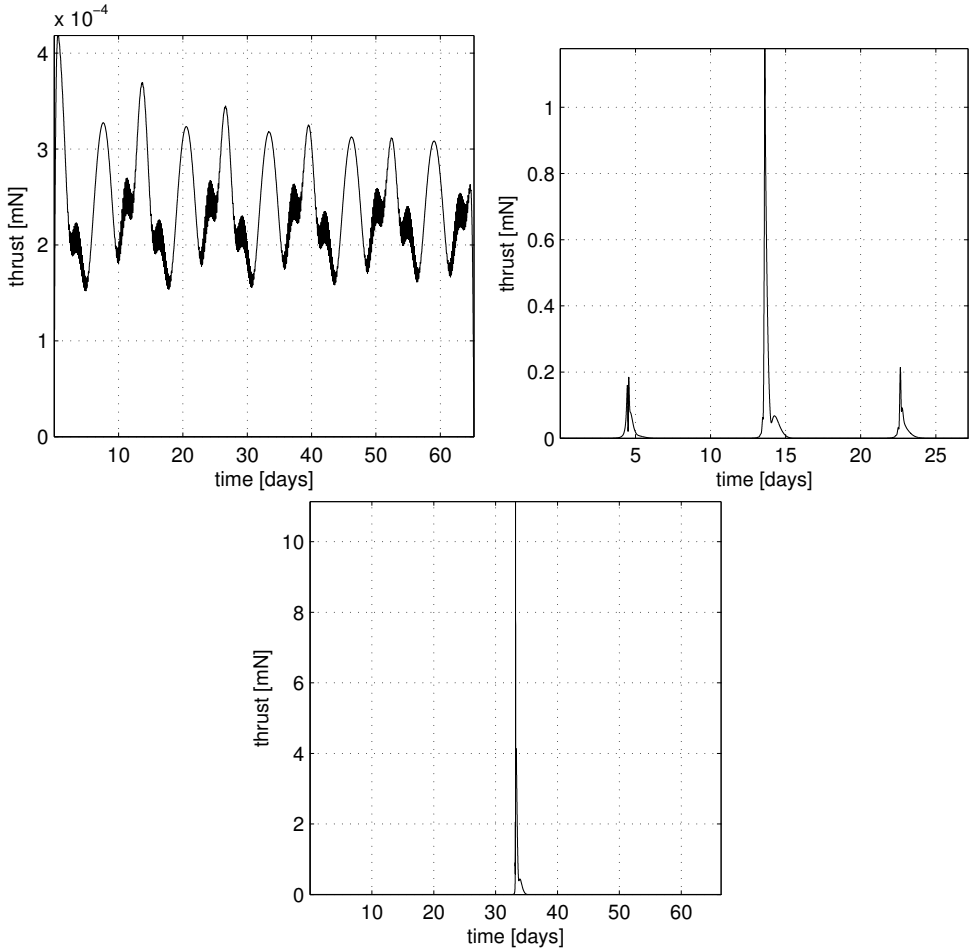

Figure 11.8. Spherical harmonic perturbations controlled by LQR, Model 2. Thrust histories of (from the top left): A (`ID1`), C (`ID3`) and DD (`ID6`).

the weights chosen for the cost function of the LQR algorithm. The shapes and properties of the curves shown are characteristic of the problem, but LQR gives us the freedom to increase or decrease the thrust and the displacement in state at will, within some ranges. The intention of the above discussion is to give estimates of the scale and behavior of the control effort necessary to stabilize the periodic orbits.

11.4 Eccentricity of the Asteroid's Orbit

The final application of the LQR stabilization consists in the simulation of the periodic orbits in the elliptic augmented Hill's problem (Section 4.4). If we consider the high eccentricity of 1999 JU3's orbit about the sun, we can expect that the dynamics will differ substantially from the circular problem. In fact the elliptic case is time dependent, hence no integral of motion like the Jacobi constant exists. The periodic orbits studied in the preceding sections no longer close onto themselves even in the absence of other perturbations, as we can readily verify by trying to use the initial conditions of our periodic orbits with the full elliptic model.

Table 11.2. Periodic orbits of the circular problem stabilized in the elliptic problem. RI stands for Random Instantaneous errors.

ID	Orbit type	C	r_{min}	Perturbations
ID8	CC	-5.686	7.105×10^{-2}	none
ID9	CC	-2.352	1.819×10^{-2}	none
ID10	CC	-1.320	4.622×10^{-3}	none, RI

Once again, we use the control obtained with the linear quadratic regulator to ensure that the real trajectories follow the ideal paths. Unlike the perturbations tested until now, in this problem not only the balance of the forces at place is changed, but also the scale of the system is different and constantly changing. In fact Section 4.4 shows that in the elliptic problem the unit of length pulsates, and that the independent variable is the true anomaly rather than time. For this reason, when we take an orbit of the circular case as nominal trajectory in the elliptic case, the resulting shape and period in non-normalized coordinates inevitably differ from the original. This, however, is not necessarily a problem from the point of view of a mission, and may indeed be a positive property. We might suppose to start an orbit when it is wide, with high-altitude flybys, then wait for the scale of the trajectory to shrink as the true anomaly advances, thus scanning gradually lower altitudes and slowly improving the gravity model of the asteroid.

Table 11.2 lists the orbits simulated in this scenario. They belong to the same family, with different close-approach distances. We report here the results of all three of them when propagated in the elliptic problem without any other perturbation. Figure 11.9 and the left column of Figure 11.10 show these results in adimensional units. From the first orbit (ID8) to the last (ID10) the minimum distance from the asteroid decreases, and the peaks of the control history get more pronounced, in a manner similar to what happens with the spherical harmonic perturbations. This dependence on the distance reflects the fact that larger differences between the circular and the elliptic problem occur when the gravitational force is stronger.

The last test, shown in the right column of Figure 11.10, simulates random instantaneous errors (page 89) in addition to the use of the elliptic problem's equations of motion. The orbit tested is the same as that in the left column, so that a comparison is easily made.

From the two sets of plots two observations are possible. The first one is that the thrust needed to correct the elliptic perturbation dominates over that needed to recover from the random errors. The second observation is that the displacements in position and velocity with respect to the nominal orbit due to the ellipticity are negligible compared to the ones introduced artificially. The reason for this apparent paradox is that, unlike sudden brief errors, the elliptic perturbation is a continued effect. Also, this force is strongest when the velocity is highest, meaning that the regulator has less time to act to counter it.

All the above applications of the linear quadratic regulator show that the orbit families found in Chapter 10 are in principle stabilizable against different types of perturbations. Little control effort is needed to counteract brisk errors in the orbit determination, and the feasible gravity irregularities that Hayabusa 2 could

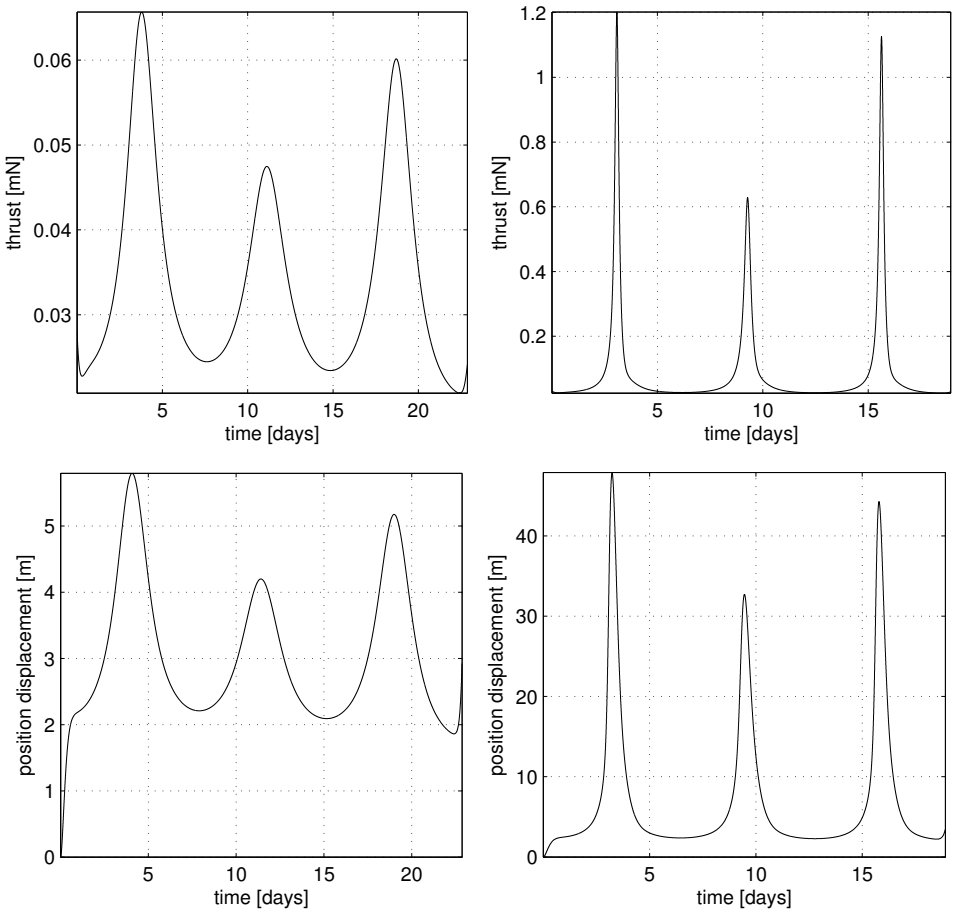

Figure 11.9. Controlled orbits in the elliptic problem. Left column: thrust and position displacement of orbit `ID8`. Right column: same plots for orbit `ID9`.

encounter at 1999 JU3 should not pose critical risks of instability when LQR is active. Finally, it would also be possible to follow circular-problem periodic orbits in the elliptic problem. In most cases, the necessary thrust is attainable by low-thrust engines such as the ones that will be on board of Hayabusa 2.

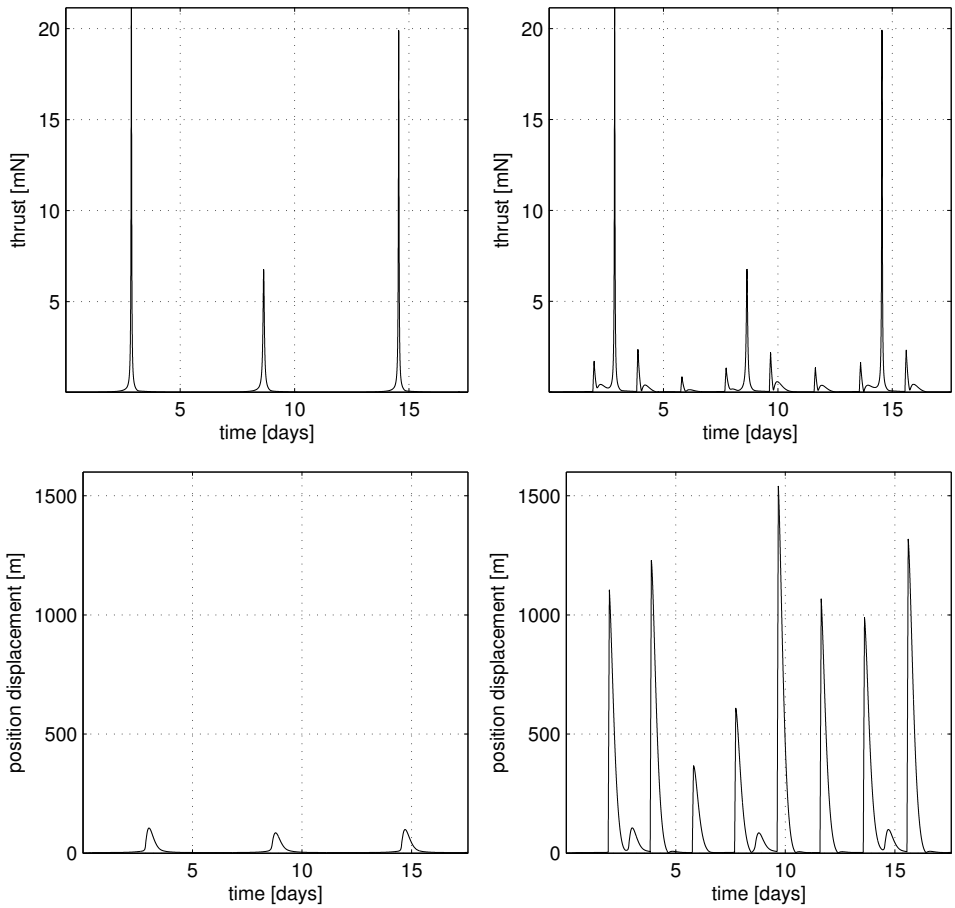

Figure 11.10. Controlled orbits in the elliptic problem. Left column: thrust and position displacement of orbit `ID10`. Right column: same plots, for the same orbit `ID10`, but with additional random instantaneous perturbations.

Chapter 12

Stable Solutions in the Elliptic Problem

As mentioned in Chapter 11, the problem of finding viable solutions in the elliptic problem can be tackled starting from the periodic orbits previously found in the circular case. The continuous change in the angular velocity and in the distance from the sun makes the elliptic problem non-conservative. As a consequence, short periodic orbits like the ones present in the circular problem are not possible. In the elliptic case the only periodic orbits that can exist are those whose period is an exact multiple of the asteroid's period around the sun.

Finding periodic orbits in the elliptic problem would require a procedure similar to that described in Chapter 5, exploiting a new symmetry that arises between the first and second half of the asteroid's period. We would thus seek two perpendicular crossings of a vertical plane containing the major axis of the orbital ellipse. We might also look for quasi-periodic orbits, which belong to higher-dimensional subspaces compared to the periodic ones. With quasi-periodic orbits there would be more solutions, and it would be easier to choose the shortest period in a way that suits the mission's objectives. Unfortunately, the computation of the invariant tori that define these quasi-periodic orbits is difficult, and to this moment it has only been applied once to the elliptic Hill's problem by Lantoine et al. [31], only for very small eccentricities ($e < 0.007$).

The orbits resulting from these theoretical computations would be delicate, making any benefit to a real mission dubious. A small perturbation, or small computational error, would break the periodicity condition, deviating from the desired path unless some active form of control is actuated. For this reason, it might be worth to relax our requirement for the orbits: instead of searching for orbits that are stable, in theory, forever, search for orbits that are stable, in reality, for a finite amount of time. We should note that the term "stability" used here is a more empirical, or practical, concept compared to the linear stability defined rigorously for periodic orbits in Section 6, as defined later in this chapter.

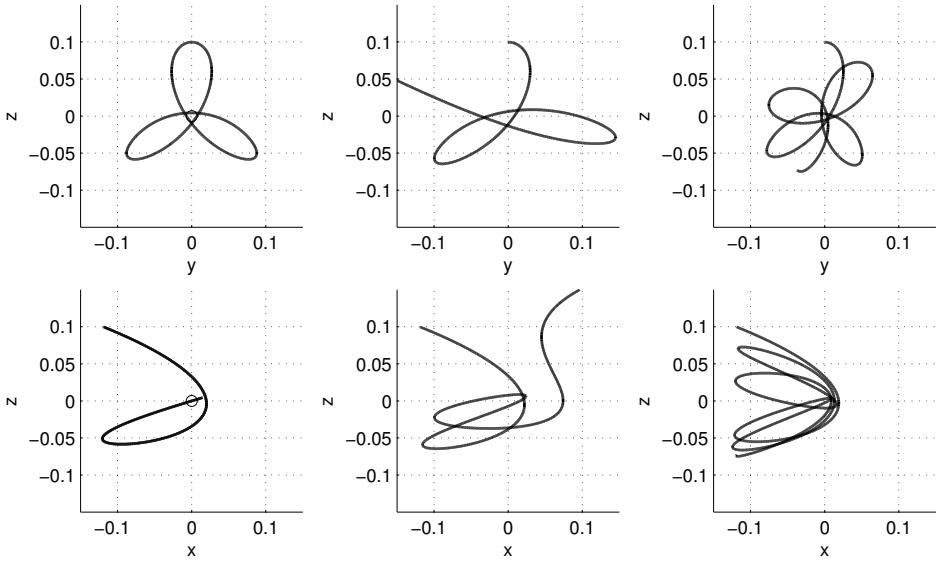

Figure 12.1. Periodic solution of the circular problem propagated in the elliptic case. Left: original, with $e = 0$; middle: $e = 0.2$ and $\nu_0 = 0$; right: $e = 0.2$ and $\nu_0 = 1$. Top row: projection on the y–z plane; bottom row: projection on the x–z plane.

12.1 Safe Regions Close to Known Orbits

If we chose a periodic orbit from the circular augmented Hill's problem and tried to naively simulate it in the elliptic equations (4.21) with $e = 0.2$, the result would be an orbit that differs widely from the original one, as shown in Figure 12.1. Not only is the new motion non-periodic, but in general it is unstable and leads either to an escape or to an impact with the asteroid. Note, however, that the time until the occurrence of one of these two undesirable outcomes depends strongly on ν_0, the initial true anomaly of the simulation.

Whereas starting at $\nu_0 = 0$ (middle column in Figure 12.1) leads to an escape in less than one period, a choice of $\nu_0 = 1$ (right-most column in Figure 12.1) gives a trajectory that remains bounded for a longer duration without escaping. The exact shape of the trajectory is changed, but some of its geometrical properties tend to remain relatively stable until an escape occurs. If we choose higher values for ν_0 the orbits tend to remain bounded for longer times. More importantly, trajectories that start at some $\nu_0 = \pi - \Delta\nu$ and remain temporarily bounded, tend to remain stable at least until $\nu = \pi + \Delta\nu$. This suggests that they settle into patterns of motion that are resilient to radiation pressure up to its initial intensity, but not to the stronger pressures that arise close to perihelium.

The above empirical evidence suggests that if a trajectory bounded for $\nu_0 = \pi - \pi = 0$ would remain bounded for more than one asteroidal period. In other words, it would be resilient to all values of the solar radiation pressure throughout the year. Also, the stable orbit's geometry would still be similar to the ideal periodic orbit, with similar initial conditions.

Based on these considerations, we perform one more grid search, at $\nu_0 = 0$, for "safe" orbits that satisfy the following two conditions.

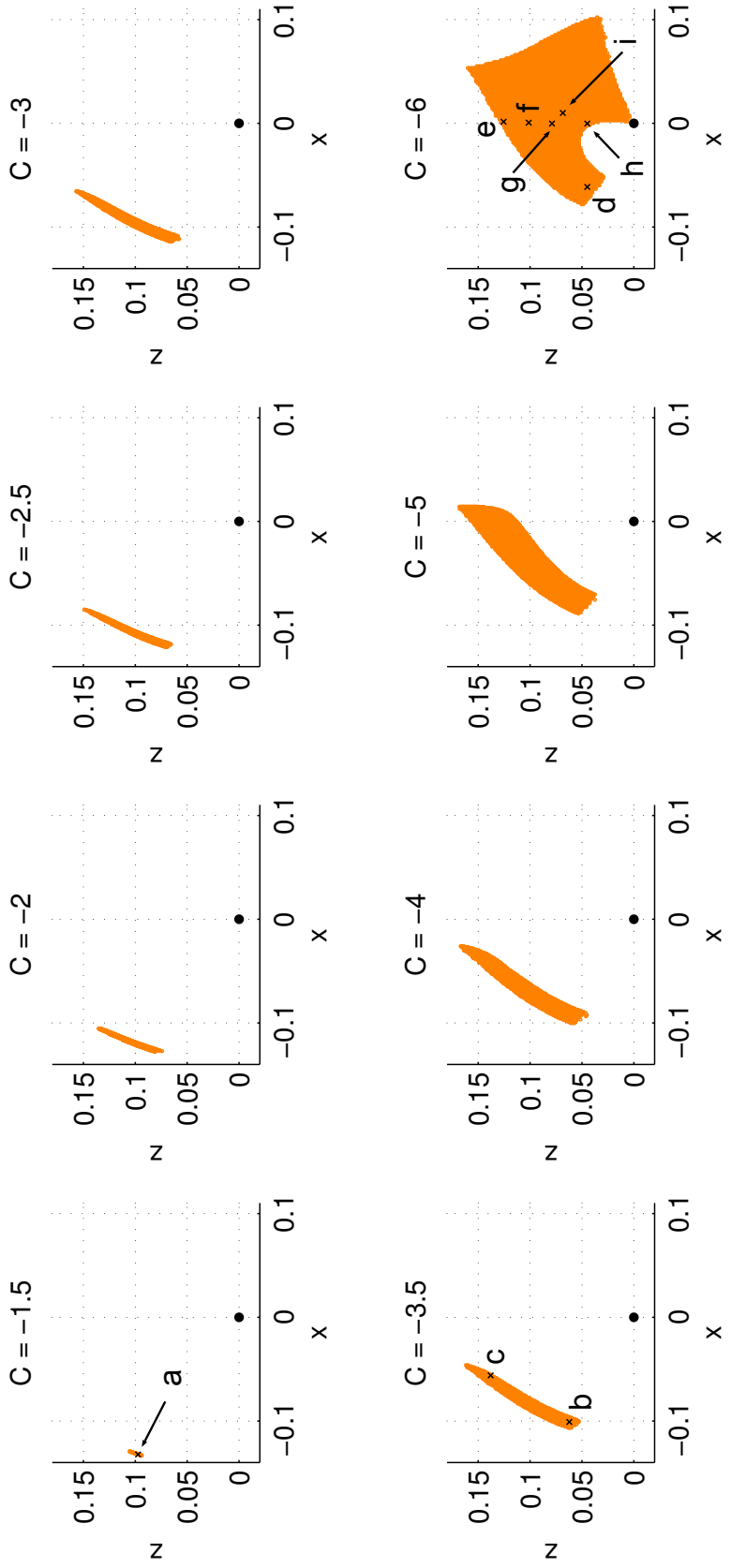

Figure 12.2. Safe regions on the x–z plane for $\nu_0 = 0$. Unit are adimensional

Table 12.1. Example orbits from the safe regions of Figure 12.2. $\beta = 31$ in all cases.

ID	$C_e(\nu_0)$	x_0	z_0	p_{sun}	p_{45}
a	−1.5	−0.132 03	0.097 30	96.5 %	80.6 %
b	−3.5	−0.100 78	0.062 26	91.7 %	57.3 %
c	−3.5	−0.056 00	0.137 93	81.2 %	11.0 %
d	−6.0	−0.061 39	0.044 82	78.5 %	19.3 %
e	−6.0	0.001 45	0.125 43	55.2 %	16.6 %
f	−6.0	0.000 55	0.101 40	50.6 %	0.0 %
g	−6.0	−0.000 31	0.078 91	34.2 %	0.0 %
h	−6.0	−0.000 17	0.044 83	18.1 %	0.0 %
i	−6.0	0.010 06	0.068 53	0.0 %	0.0 %

1. **Bounded**: remains inside a sphere of adimensional radius $r = 0.18$ for the whole duration of the simulation.

2. **Non-impacting**: does not impact with the asteroid, i.e. $r > R_a$ at all times during the simulation.

All the orbits start from the x–z plane at $\nu_0 = 0$ with a purely out-of-plane velocity, in a small region close to the initial condition of the periodic orbit chosen as reference. When necessary, this search region can be expanded on the plane to include more orbits and obtain a more complete map. This procedure helps reduce the number of necessary simulations. The velocity is determined by the instantaneous elliptic equivalent of the Jacobi integral, C_e (Section 4.4), of which several values are tested. The duration of propagation of all the orbits is $\Delta\nu_p = 1.2\pi$, enough to cover all the distances from the sun. We verified with longer-duration maps that the majority of the orbits that satisfy our two conditions for $\Delta\nu_p$ continue satisfying them for several asteroid years.

Figure 12.2 shows the maps resulting from this search, as performed with various choices of $C_e(\nu_0)$, with $\beta = 31$ and with initial velocity in the $+y$ direction. The periodic orbit family used as initial reference is C, which, as was shown in Section 10.5, is one of the most appropriate choices for Hayabusa 2 in the circular Hill's problem. The colored areas represent the orbits that satisfy both the "bounded" and the "non-impacting" conditions, and thus are stable for long periods of time. At high C_e, the stable region is small, concentrated close to the point [−0.13, 0, 0.10]. As the energy decreases, the position of the region moves closer to the asteroid, its shape evolves and its surface increases. When C_e approaches −6, the safe region spreads widely into the positive–x semi-plane, and also reaches very close to the asteroid.

12.2 Examples of Long-Term Stable Orbits

Any point inside the safe regions corresponds to a long-term stable orbit. Table 12.1 reports nine examples that display different shapes and properties. The location of these examples is also shown in the maps of Figure 12.2, and their trajectories are plotted in Figures 12.3–12.5. Each orbit is simulated for 3 asteroid years.

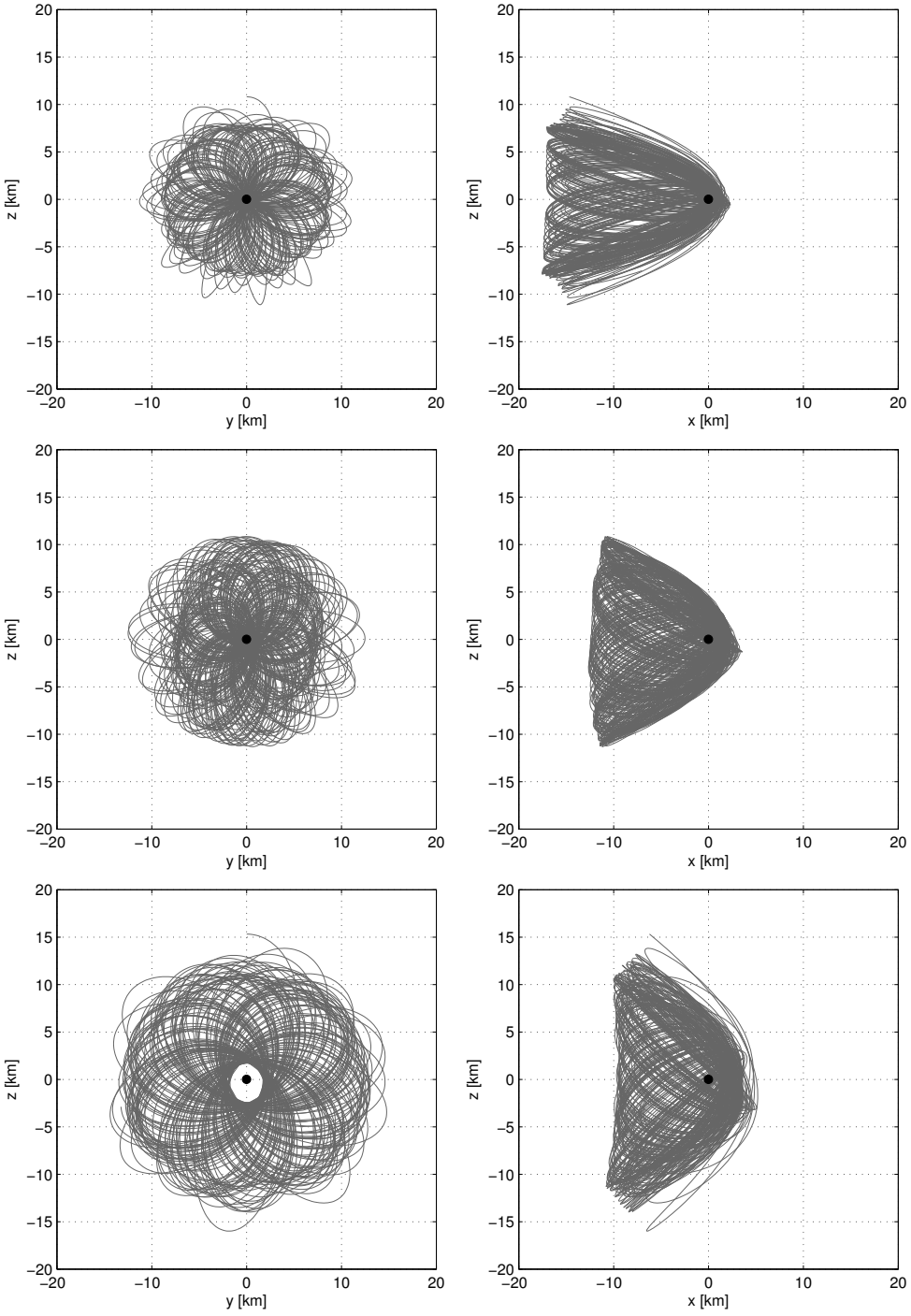

Figure 12.3. Example orbits `a`, `b` and `c`, respectively, from top to bottom. Left column: As seen from the sun. Right column: side view.

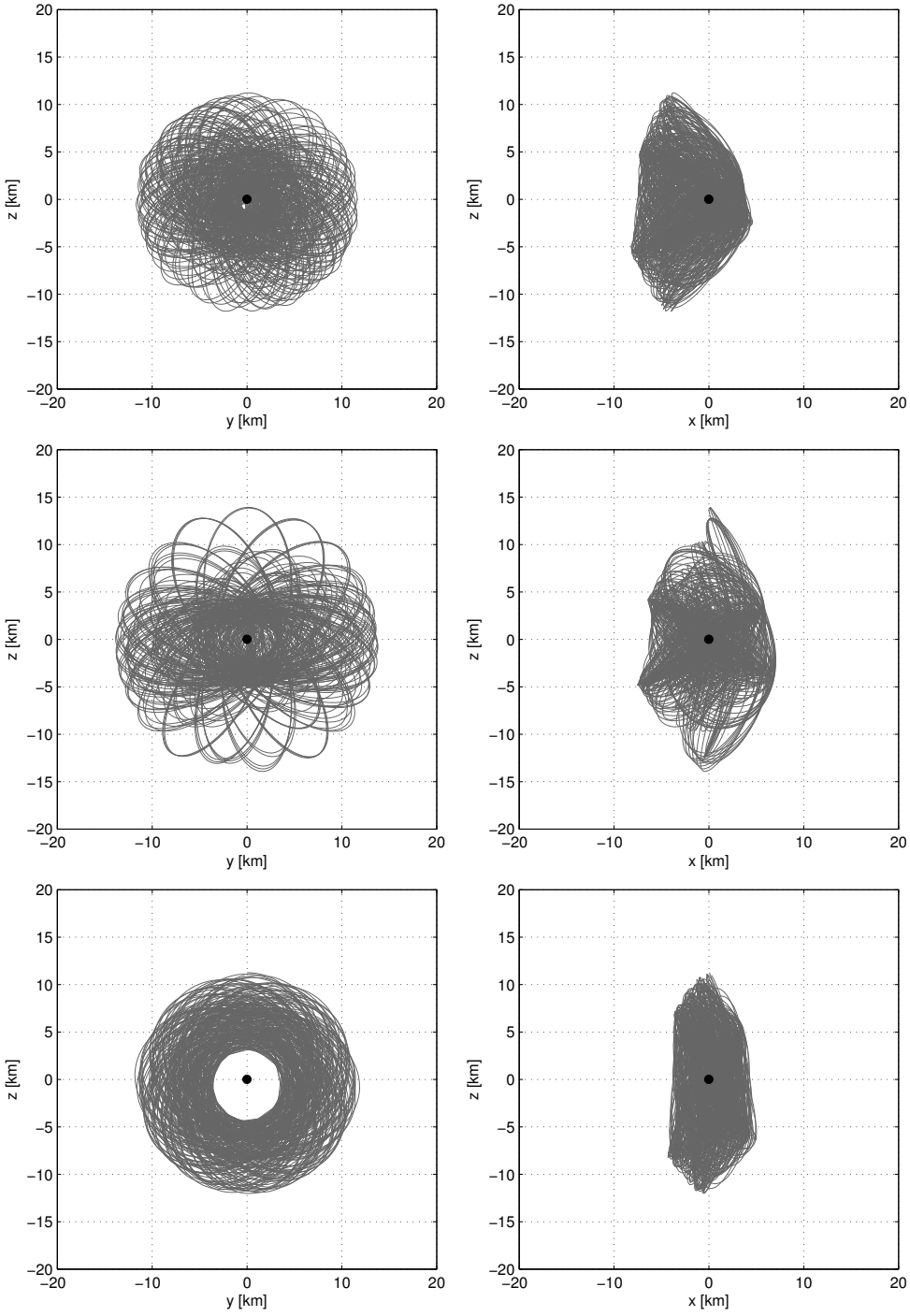

Figure 12.4. Example orbits `d`, `e` and `f`, respectively, from top to bottom. Left column: As seen from the sun. Right column: side view.

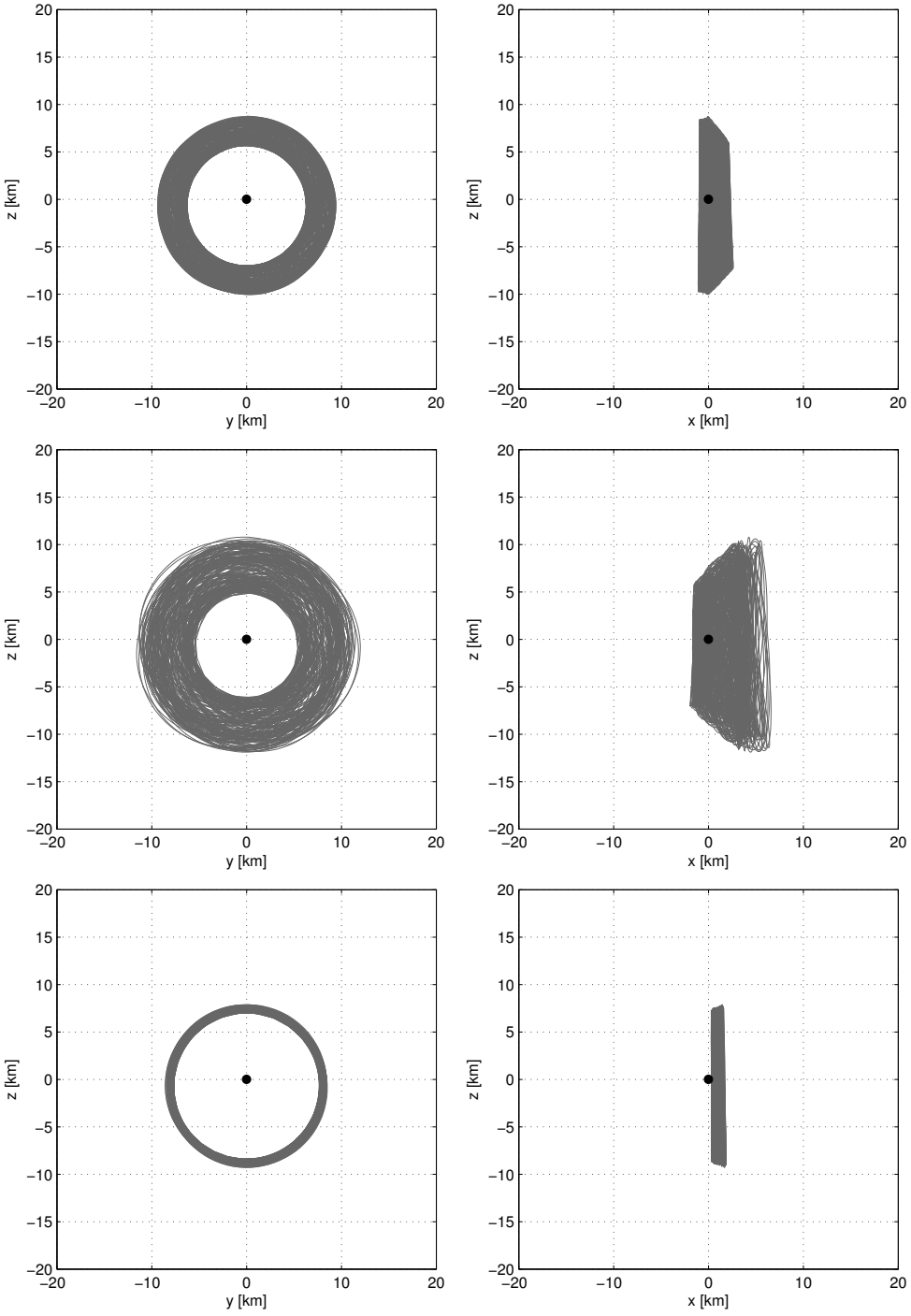

Figure 12.5. Example orbits `g`, `h` and `i`, respectively, from top to bottom. Left column: As seen from the sun. Right column: side view.

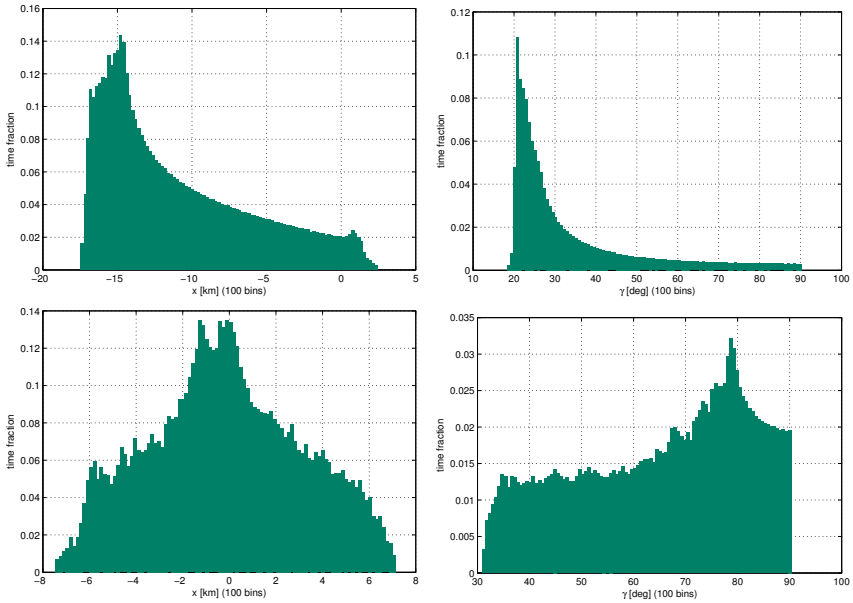

Figure 12.6. Distributions of the x coordinate (left column) and of the angle of the velocity with the sun-asteroid line (right column) for orbits `a` (top row) and `e` (bottom row).

The figures show that various shapes and sizes are possible, depending on the energy and on the initial position inside the safe regions. For instance, orbits with high $C_e(\nu_0)$ (Figure 12.3) have the shape of a bell open towards the sun, with variable diameter at the open end. As the energy increases, the bells become shorter and their "walls" thicken. Eventually their shapes become more complex, like in orbit `e` (Figure 12.4) or more ring-shaped. Some orbits close to the $x = 0$ plane are very similar to circular orbits, and indeed should be identified with the terminator-plane orbits studied in detail by Scheeres [56] (Figure 12.5, bottom). The majority of the orbits never passes through the asteroid's shadow. Even those that get very close to the surface, like `a`, mostly leave an oval opening on the positive x side of the asteroid. This property is a strong point in favor of these orbits from the perspective of the Hayabusa 2 mission.

12.2.1 Properties of the Stable Solutions

The safe region maps in Figure 12.2 are a useful tool for the design of trajectories with the desired parameters. They allow us to select the properties that are best suited for the mission, such as the amount of time spent over the sunlit side of the asteroid surface and the component of the velocity in the direction of the sun for Doppler measurements, similar to the study performed in Section 10.5.

These two properties are reported in Table 12.1. In more rigorous terms, p_{sun} is the percentage of time spent with negative values of the x coordinate, while p_{45} is the percentage of time where the velocity vector has a sun-angle γ (Subsection 2.5.1) lower than 45°. The two parameters, p_{sun} and p_{45}, are obtained from the distributions of the x coordinate and of the velocity angle of the orbits, based on how much time is spent at each value. To show how these distributions can vary among

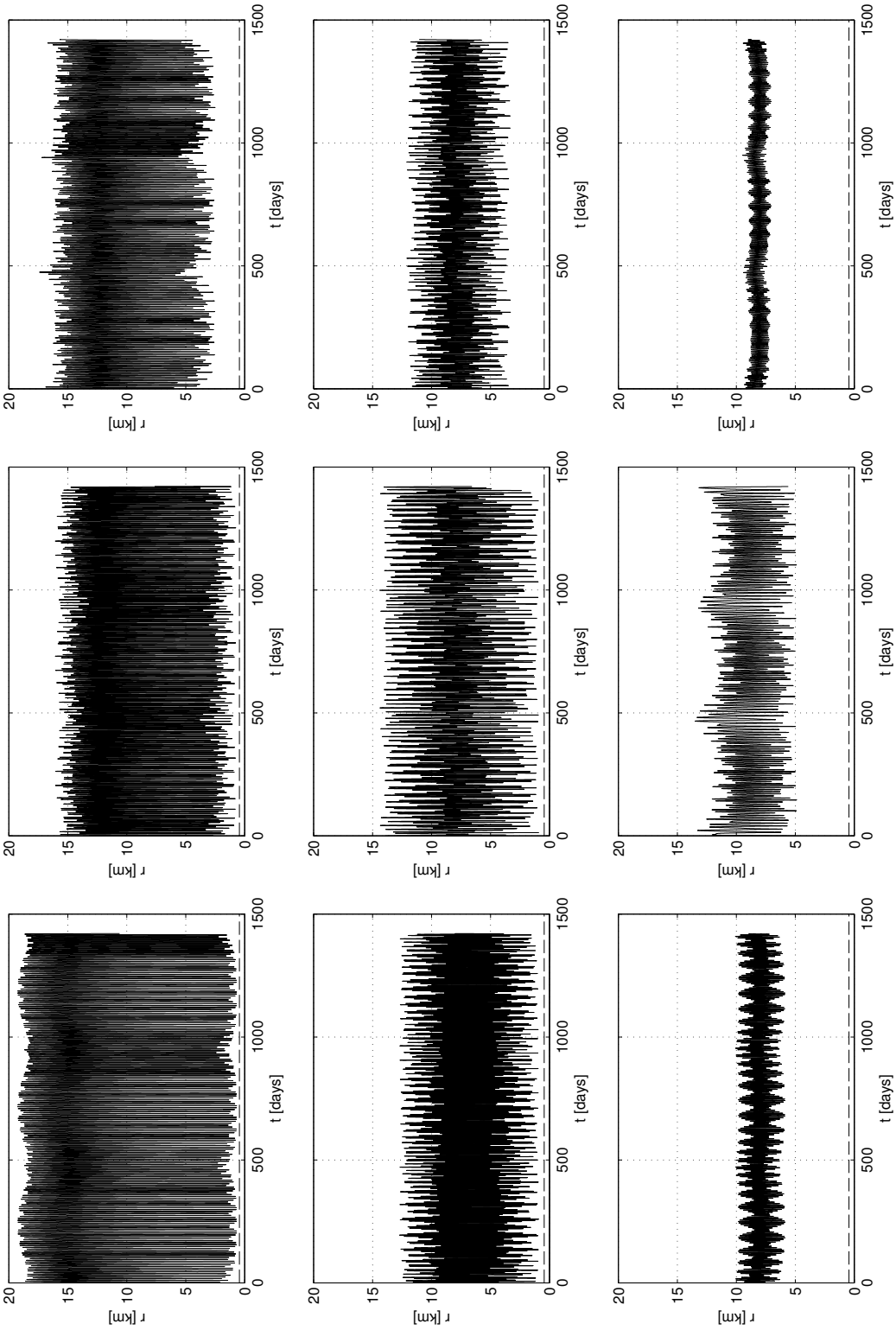

Figure 12.7. Asteroid distance history of all the orbits listed in Table 12.1, in order from the top left. Asteroid's radius shown as a dashed line.

different trajectory types, Figure 12.6 reports two examples, where the numbers have been normalized to make the total area equal to 1. The bell-shaped orbits (`a`–`d`) generally have higher p_{sun} and p_{45} and are thus more suited to an application by Hayabusa 2. This should be expected, because they are the trajectories most closely resembling the "sun-side" group of periodic orbits, which the discussion in Chapter 10 has shown to be the most appropriate choice for the circular problem.

The property of being on the sun-side and bell-shaped appears to be correlated to the initial value of the sun-angle γ, from the $-x$ semi-axis. This is demonstrated by the `b` and `c` orbits (see points in Figure 12.2). Both are selected at the same energy and in the same region of stability but `b`, with lower initial γ, has 14.7% more sunlit surface coverage and 430% more time with low Doppler angles than `c`. Orbit `d`, despite being close to the structurally different orbits `f`–`i`, has a low γ and thus still presents relatively high p_{sun} and p_{45}.

Finally, it is possible to select the closest approach distance from a wide range of possibilities. The asteroid-spacecraft distance of all the selected examples is shown as a function of time in Figure 12.7. Ring-shaped orbits only mildly oscillate around a fixed distance. For instance, this average distance is 8.3 km in the case of orbit `i`. Bell-shaped orbits, on the other hand, take wide ranges of distances.

The choice of the desired stable trajectories for Hayabusa 2, albeit quite wide, may involve trade-offs among the various requirements discussed in this chapter and in Chapter 10. Only a careful multi-objective analysis would allow for reliable decisions in orbit design, but the information currently available about the asteroid and the conditions of the spacecraft at the time of rendezvous is insufficient for such a complete study. This chapter aims at providing evidence for the existence of a wide variety of "stable" trajectories at the relatively high eccentricity of 1999 JU3, and to give some insights into the types and distributions of these trajectories. The problem of finding feasible orbits in the elliptic problem is certainly the most interesting application of Hill's problem, but it is still scarcely understood. Further works in this field will need to characterize the properties and the relations between the various types of orbits, as well as their behavior in the presence of perturbations of different types and intensities.

Chapter 13

Conclusions

Compared to that around the planets, the sun, or even Lagrangian points, the dynamical environment around a small asteroid is still largely unexplored and not well understood. Only three missions have performed a rendezvous with an asteroid until now. Of these, only Hayabusa has targeted a small asteroid, where the relative perturbation of solar radiation pressure is largest, and even then it hovered instead of orbiting.

Most of the rendezvous missions planned for the future, however, will visit asteroids of the same scale as Itokawa, and will have to face that same little-known dynamical environment. Other missions will likely follow these, with increasingly ambitious scientific and technical goals. For this reason, and given the recent rise of concern for the risk of an asteroid impact with the earth, the design of reliable and stable trajectories in such systems is becoming an important astrodynamical challenge.

This work tries to contribute new knowledge and, perhaps, insight on this topic, as an application for the soon-to-be-launched Hayabusa 2 mission. The final result of this research effort is a group of different trajectories that appear to be stable, and safe from impacts, for long periods of time. Indeed, their periods of stability typically last much longer than what is required by the Japanese mission, and in many cases they appear to be indefinitely long.

Stable orbits in the elliptic Hill's problem are not the only result offered by this work. In the process of understanding the behavior of trajectories around the asteroid, we obtain a variety of spatial periodic orbits valid in the circular variant of the problem. These, being in a sense the "backbone" of the general motion in that region, have an importance, if not for direct applications, for their theoretical value. They also serve as a way to identify the best orbital configurations for the specific requirements of the Hayabusa 2 mission, helping the search for more general solutions in the full elliptic problem.

Part of this research briefly addresses also the problem of controlling orbits around an asteroid. Through a relatively simple formulation of the LQR, we show the type and the amount of control necessary to correct different types of perturbations. Far from being a complete and high-fidelity simulation, this part aims to give first estimates of the necessary thrust and its stabilization capabilities. It demonstrates that, with conditions close to those of the real Hayabusa 2 rendezvous, most orbits

are indeed stabilizable and that even low-thrust propulsion would suffice in most cases.

Obviously, there is still much to understand about the long-term stable (or quasi-periodic) trajectories, with more detailed and multidisciplinary research necessary before being able to actually select them for a space mission. However, by providing examples of stable orbits in the elliptic Hill's problem that are suitable to Hayabusa 2's design, this thesis fulfills its primary goal, that is, describing a feasible alternative strategy that overcomes some of the shortcomings of hovering. Given the recent interest in small-body rendezvous projects, these bell-shaped orbits around asteroids are likely to assume the same importance that halo and Lissajous orbits have taken in the last decades in practical applications in the vicinity of the earth.

Bibliography

[1] Abe, M., et al. Ground-based observational campaign for asteroid 162173 1999 JU3. *37th COSPAR Scientific Assembly*, **37** (2008).

[2] Athans, M. and Falb, P. *Optimal Control: An Introduction to the Theory and Its Applications*. Dover Publications (2006).

[3] Bray, T. and Goudas, C. Doubly Symmetric Orbits About the Collinear Lagrangian Points. *The Astronomical Journal*, **72** (1967).

[4] Broschart, S. B., Lantoine, G., and Grebow, D. J. Characteristics of Quasi-Terminator Orbits Near Primitive Bodies. In *AAS 13-335* (2013).

[5] Broucke, R. A. Periodic orbits in the restricted three-body problem with Earth-Moon masses. *Pasadena, Jet Propulsion Laboratory, California Institute of Technology, 1968.*, **1** (1968).

[6] Broucke, R. A. Stability of periodic orbits in the elliptic, restricted three-body problem. *AIAA journal*, **7** (1969).

[7] Campins, H., Emery, J. P., Kelley, M., Fernández, Y., Licandro, J., Delbó, M., Barucci, M. A., and Dotto, E. Spitzer observations of spacecraft target 162173 (1999 JU3). *Astronomy and Astrophysics*, **503** (2009).

[8] Chavineau, B. *Dynamique à long terme des astéroides binaires. Bilan des observations et approche théorique*. Ph.D. thesis (1990).

[9] Chesley, S. R., et al. Direct detection of the Yarkovsky effect by radar ranging to asteroid 6489 Golevka. *Science (New York, N.Y.)*, **302** (2003).

[10] Doedel, E., Paffenroth, R., Keller, H. B., Dichmann, D. J., Galan-Vioque, J., and Vanderbauwhede, A. Computation of periodic solutions of conservative systems with application to the 3-body problem. *International Journal of Bifurcation and Chaos*, **13** (2003).

[11] Giancotti, M. and Funase, R. Solar Sail Equilibrium Positions and Transfer Trajectories Close to a Trojan Asteroid. In *63rd International Astronautical Congress* (2012).

[12] Hasegawa, S., et al. Albedo, Size, and Surface Characteristics of Hayabusa-2 Sample-Return Target 162173 1999 JU3 from AKARI. *Publications of the Astronomical Society of Japan*, **60** (2008).

[13] Hénon, M. Exploration Numérique du Problème Restreint - II - Masses Égales, Stabilité des Orbites Périodiques. *Annales d'Astrophysique*, **28** (1965).

[14] Hénon, M. Numerical Exploration of the Restricted Problem. V. Hill's Case: Periodic Orbits and Their Stability. *Astronomy and Astrophysics*, **1** (1969).

[15] Hénon, M. Vertical stability of periodic orbits in the restricted problem. I. Equal masses. *Astronomy and Astrophysics*, **28** (1973).

[16] Hénon, M. Vertical stability of periodic orbits in the restricted problem. II. Hill's case. *Astronomy and Astrophysics*, **30** (1974).

[17] Hill, G. W. Researches in the lunar theory. *American Journal of Mathematics*, **1** (1878).

[18] Howell, K. C. and Pernicka, H. J. Numerical Determination of Lissajous Trajectories in the Restricted Three-Body Problem. *Celestial Mechanics and Dynamical Astronomy*, **41** (1987).

[19] Hu, W. and Scheeres, D. J. Numerical determination of stability regions for orbital motion in uniformly rotating second degree and order gravity fields. *Planetary and Space Science*, **52** (2004).

[20] Ichtiaroglou, S. Elliptic Hill's problem-The continuation of periodic orbits. *Astronomy and Astrophysics*, **92** (1980).

[21] Ikeda, H., Tsuda, Y., Mimasu, Y., and Yoshikawa, M. A Simulation Study of Gravity and Ephemeris Estimation of Asteroid 1999JU3 Using Spacecraft Radiometric Tracking, Optical and Altimeter Measurements. In *23rd AAS/AIAA Spaceflight Mechanics Meeting, Kauai, Hawaii* (2013).

[22] Jacobi, C. G. J. Sur le mouvement d'un point et sur un cas particulier du probleme des trois corps. *Compte Rendu de l'Académie des Sciences, Paris*, (1836).

[23] Jacobi, C. G. J. Sur l'élimination des noeuds dans le problème des trois corps. *Astronomische Nachrichten*, (1843).

[24] Katherine, Y.-Y. L. and Villac, B. F. Periodic orbits families in the hill's three-body problem with solar radiation pressure. In *Advances in the Astronautical Sciences Series 136*, vol. 1 (2010). ISBN 9780877035602.

[25] Kaula, W. M. *Theory of Satellite Geodesy: Applications of Satellites to Geodesy*. Dover Publications (2000).

[26] Kawaguchi, J., Fujiwara, A., and Uesugi, T. Hayabusa - Its technology and science accomplishment summary and Hayabusa-2. *Acta Astronautica*, **62** (2008).

[27] Kawaguchi, J., Kominato, T., and Shirakawa, K. Attitude Control Flight Experience: Coping with Solar Radiation and Ion Engines Leak Thrust in Hayabusa (MUSES-C). In *20th ISSFD Conference, 24-28 September, 2007, Annapolis, Maryland, USA* (2007).

[28] Kazantzis, P. and Goudas, C. A grid search for three-dimensional motions and three new types of such motions. *Astrophysics and Space Science*, **32** (1975).

[29] Kim, M.-j., et al. Searching the pole solution of NEA 162173 (1999 JU3) [poster]. In *Conference at the Korean Space Science Society, April 24-26 2013, Jeju island, Korea*, vol. 162173.

[30] Kim, M.-J., et al. Optical observations of NEA 162173 (1999 JU3) during the 2011-2012 apparition. *Astronomy & Astrophysics*, **550** (2013).

[31] Lantoine, G., Broschart, S. B., and Grebow, D. J. Design of Quasi-Terminator Orbits Near Primitive Bodies. In *AAS 13-815* (2013).

[32] Lara, M. and Scheeres, D. J. Stability bounds for three-dimensional motion close to asteroids. *The Journal of the Astronautical Sciences*, **50** (2002).

[33] Lazzaro, D., Barucci, M. A., Perna, D., Jasmim, F. L., Yoshikawa, M., and Carvano, J. M. F. Rotational spectra of (162173) 1999 JU3, the target of the Hayabusa2 mission. *Astronomy & Astrophysics*, **549** (2012).

[34] Lowry, S. C., et al. Direct detection of the asteroidal YORP effect. *Science (New York, N.Y.)*, **316** (2007).

[35] Matukuma, T. On the Periodic Orbits in Hill ' s case. *Proceedings of the Imperial Academy*, **6** (1930).

[36] Matukuma, T. Periodic Orbits in Hill's Case. Third Paper. *Proceedings of the Imperial Academy*, **8** (1932).

[37] Matukuma, T. Periodic Orbits in Hill's Case. Third Paper. *Proceedings of the Imperial Academy*, **9** (1933).

[38] Maxwell, J. C. On physical lines of force. *The London, Edinburgh, and Dublin Philosophical Magazine and Journal of Science*, (1861).

[39] Miele, A. Revisit of the Theorem of Image Trajectories in the Earth-Moon Space. *Journal of Optimization Theory and Applications*, **147** (2010).

[40] Mignard, F. and Hénon, M. About an unsuspected integrable problem. *Celestial Mechanics and Dynamical Astronomy*, **33** (1984).

[41] Montenbruck, O. and Gill. *Satellite orbits: models, methods, and applications*. Springer (2000).

[42] Morrow, E., Scheeres, D. J., and Lubin, D. Solar Sail Orbit Operations at Asteroids. *Journal of Spacecraft and Rockets*, **38** (2001).

[43] Muller, T., et al. Thermo-physical properties of 162173 (1999 JU3), a potential flyby and rendezvous target for interplanetary missions. *Astronomy and Astrophysics*, (2010).

[44] Muller, T., et al. Thermal Lightcurves of 1999 JU3, Target of Hayabusa 2, Using Warm Spitzer. *AAS/Division for Planetary Sciences Meeting Abstracts*, **45** (2013).

[45] Munoz-Almaraz, F., Freire, E., Galán, J., Doedel, E., and Vanderbauwhede, A. Continuation of Periodic Orbits in Conservative and Hamiltonian Systems. *Physica D: Nonlinear Phenomena*, **181** (2003).

[46] Newton, I., Bernoulli, D., MacLaurin, C., and Euler, L. *Philosophiae naturalis principia mathematica*. Sumptibus C. & A . Philibert (1760).

[47] Öpik, E. J. Collision Probabilities with the Planets and the Distribution of Interplanetary Matter. *Proceedings of the Royal Irish Academy. Section A: Mathematical and Physical Sciences*, **54** (1951).

[48] Papadakis, K. and Zagouras, C. Bifurcation Points and intersections of Families of Periodic Orbits in the Three-Timensional Restricted Three-Body Problem. *Astrophysics and Space Sciences*, **199** (1993).

[49] Petit, J. and Hénon, M. Satellite encounters. *Icarus*, (1986).

[50] Poincaré, H. and Magini, R. Les méthodes nouvelles de la mécanique céleste. *Il Nuovo Cimento (1895-1900)*, (1899).

[51] Rossi, A., Marzari, F., and Farinella, P. Orbital evolution around irregular bodies. *Earth Planets and Space*, **51** (1999).

[52] Russell, R. P. Global Search for Planar and Three-Dimensional Periodic Orbits Near Europa. In *AAS/AIAA Astrodynamics Specialist Conference*. Lake Tahoe, California (2005). ISBN 8183936245.

[53] Scheeres, D. J. Dynamics about Uniformly Rotating Triaxial Ellipsoids: Applications to Asteroids. *Icarus*, **110** (1994).

[54] Scheeres, D. J. Dynamics of Orbits Close to Asteroid 4179 Toutatis. *Icarus*, **132** (1998).

[55] Scheeres, D. J. Satellite Dynamics about Small Bodies: Averaged Solar Radiation Pressure Effects. *Journal of the Astronautical Sciences*, (1999).

[56] Scheeres, D. J. Orbital Mechanics Sbout Small Bodies. *Acta Astronautica*, **72** (2011).

[57] Scheeres, D. J. *Orbital Motion in Strongly Perturbed Environments*. Springer (2012).

[58] Scheeres, D. J., Sutter, B., and Rosengren, A. Design , Dynamics and Stability of the OSIRIS-REx Sun-Terminator Orbits. In *23rd AAS/AIAA Spaceflight Mechanics Meeting, Kauai, Hawaii* (2013).

[59] Simó, C. New families of solutions in N-body problems. *European Congress of Mathematics*, (2001).

[60] Sundman, K. F. Mémoire sur le problème des trois corps. *Acta Mathematica*, **36** (1912).

[61] Szebehely, V. *Theory of Orbits. The Restricted Problem of Three Bodies.* Academic Press (1967).

[62] Tsuda, Y., Yoshikawa, M., Abe, M., Minamino, H., and Nakazawa, S. System design of the Hayabusa 2 - Asteroid sample return mission to 1999 JU3. *Acta Astronautica*, **91** (2013).

[63] Vokrouhlický, D. A Note on the Solar Radiation Perturbations of Lunar Motion. *Icarus*, **126** (1997).

[64] Vokrouhlický, D. and Milani, A. Direct solar radiation pressure on the orbits of small near-Earth asteroids: observable effects? *Astronomy and Astrophysics*, **755** (2000).

[65] Yarkovsky, I. O. The density of luminiferous ether and the resistance it offers to motion. *Tipografiadina Bryansk*, (1901).

[66] Zagouras, C. and Markellos, V. Axisymmetric Periodic Orbits of the Restricted Problem in Three Dimensions. *Astronomy and Astrophysics*, **59** (1977).

Index